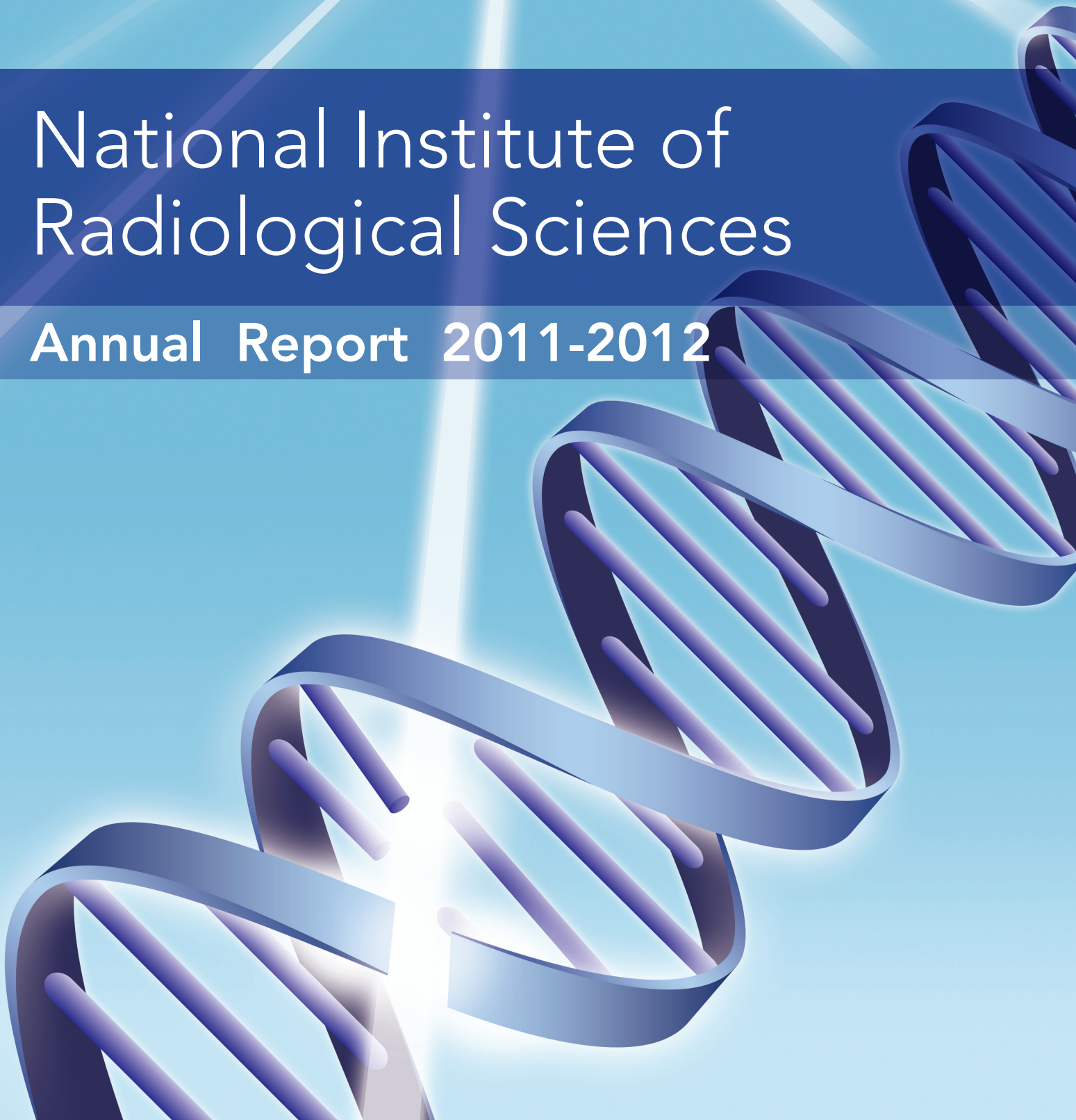


National Institute of Radiological Sciences

Annual Report 2011-2012



Annual Report 2011-2012
(April 2011-March 2013)

NATIONAL INSTITUTE OF
RADIOLOGICAL SCIENCES

Date of Publication May 2013
Editing and Publication Research Information Science
 Dept. of Information Technology
 Research, Development and Support Center
 National Institute of Radiological Sciences
 Anagawa 4-9-1, Inage-ku, Chiba, 263-8555 Japan
 Tel : +81-43-206-3485
 Fax : +81-43-290-1112
 E-mail: kagakujohoka@nirs.go.jp

Homepage:<http://www.nirs.go.jp>

Full Text: <http://www.nirs.go.jp/ENG/publications/index.shtml>

Copyright ©2013 National Institute of Radiological Sciences All Rights Reserved

Printed in Japan

ISSN 0439-5956

NIRS-51

Editorial Note

This document presents research and development results of NIRS, representing combined annual reports for the two fiscal years of 2011 and 2012 (April 2011-March 2013). Since the 3rd mid-term plan of NIRS was begun in fiscal year 2011, the Editorial Working Group felt this was a good opportunity to revise the contents and format of the annual report. The main revision we made was to publish summarized results on each research theme as “Highlights”. Then, from them we chose two themes and published these results as “Topics”.

This report is available as an electronic edition on the NIRS web site (<http://www.nirs.go.jp/ENG/publications/index.shtml>). This electronic edition includes the “List of original papers” which was not included in the print edition. The Editorial Working Group hopes that you will use it to explore more deeply what NIRS researchers have been doing.

Editing Committee

Yoshinobu HARADA
Hiroshi ISHIHARA
Etsuko ITO
Tomonori KUDO
Takeshi MAEDA
Ikuo NAKANISHI
Masumi NOZATO
Hiroaki SAITO
Shino TAKEDA
Masami TORIKOSHI (Editor-in-Chief)

Editorial Staff

Reiko ISHII
Ryouji MIMIDUKA
Masanori OKAMOTO
Masae SAEKI
Takeo SHIMOMURA

Contents

Preface	8
■ Outline of Research Activities	10
■ Research on Cancer Therapy with Carbon Beams	12
<Department of Accelerator and Medical Physics>	
<i>Highlights</i>	
Commissioning of the new ridge-filters and treatment planning system XiO-N	14
Development of multiple-energy operation with extended flattops	16
<Research on the Standardization and Clarification of Charged Particle Therapy>	
<i>Highlights</i>	
Research on the standardization and clarification of charged particle therapy	18
Gradient-vibrated MR elastography for charged particle radiation therapy assessment: A preliminary human study	20
<Research and Development on Medical Physics and Biology>	
<i>Highlights</i>	
Development of fast 3D scanning irradiation system	22
Development of patient handling system	24
<Basic Research on the Estimation of Effectiveness of Radiotherapy for Individual Cancer Patients>	
<i>Highlights</i>	
Irradiation alters the invasive potential of pancreatic cancer cell lines, MIAPaCa-2 and PANC-1, via altering protease activities, and also affecting mesenchymal and amoeboid mode of motility	26
Inherent factors in radiosensitivity to high linear energy transfer carbon ions (C-ions) in normal lung tissue	28
<Research and Development for the International Promotion of Carbon Ion Radiotherapy>	
<i>Highlights</i>	
Promotion of carbon-ion radiotherapy facilities	30
The Research Project with Heavy Ions at NIRS-HIMAC	32
■ Molecular Imaging Research for Functional Diagnosis	34
<Development and Production of PET Probes for Molecular Imaging>	
<i>Highlights</i>	
Synthesis and evaluation of [¹¹ C]ITMM for positron emission tomography imaging of metabotropic glutamate receptor subtype 1 in rodent brain	38
Development of a ceramic target vessel with potentially wide applicability for remote production of metallic radionuclides	40
<Research and Development of Advanced Bioimaging and Quantitative Analysis System>	
<i>Highlights</i>	
Impact of the laser-processed X'tal cube detector with 1 mm isotropic resolution in PET imaging	42
Image-based head movement correction for reliable quantification of receptor binding in PET dynamic studies	44
<Research on Pathophysiological Diagnosis of Cancer and Other Diseases with Molecular Imaging>	
<i>Highlights</i>	
Development of a novel positron emission tomography probe ⁶⁴ Cu-cyclam-RAFT-c(-RGDfK-) ₄ for noninvasive visualization and quantification of tumor angiogenesis and monitoring of antiangiogenic efficacy via targeting the tumor α _v β ₃ integrin	46
Tissue redox activity as a sensing platform for molecular imaging of cancer in vivo and in situ	50
<Molecular Imaging Research on Neuropsychiatric Disorders>	
<i>Highlights</i>	
Integrating cognitive neuroscience: from molecules to neural responses, to society	54
β-Amyloid in Lewy body disease is related to Alzheimer's disease-like atrophy	56

■ Research on Radiation Protection	58
< Biospheric Assessment for Waste Disposal >	
<i>Highlights</i>	
Isotopic evidence of Pu release into the environment from the Fukushima nuclear accident	62
Monitoring of radioactive fallout at National Institute of Radiological Sciences	64
< Experimental Studies on the Radiation Protection of Children >	
<i>Highlights</i>	
Age-dependent relative biological effectiveness of carbon ion radiation for rat mammary carcinogenesis	66
Combined exposure to X-irradiation and <i>N</i> -ethyl- <i>N</i> -nitrosourea treatment alters the frequency and spectrum of <i>Ikaros</i> point mutations in murine T-cell lymphoma	68
< Mechanistic Studies on the Reduction of Risks Relating to Radiation >	
<i>Highlights</i>	
Reduction of high-dose-radiation-induced delayed genotoxic effects by radioadaptive response in mice	70
<i>Looking for biomarkers that identify potentially sensitive individuals: Development of technology to discover genetic radiation risk-modifying factors and their biomarkers useful for radiation risk reduction</i>	72
< Bridging the Gap between Scientific Knowledge and Society: Regulatory Sciences Research >	
<i>Highlights</i>	
Risk perception in Japan of nuclear power and other risk factors during 25 years before the Fukushima Daiichi Nuclear Power Plant accident	74
Protection against radon	78
■ Research on Radiation Emergency Medicine	80
< Research on the Regeneration Therapy of Severe Radiation Damage and on the Decorporation of Actinides >	
<i>Highlights</i>	
Acute toxicity of uranium and the effects of decontamination agents in a simulated wound model of rodents	82
Novel therapeutic strategy using mesenchymal stem cell derived exosomes for radiation damage treatment	84
< Research on the Development of Dosimetric Technology >	
<i>Highlights</i>	
Sensitive and rapid detection of centromeric alphoid DNA in human metaphase chromosomes by fluorescence <i>in situ</i> hybridization using peptide nucleic acid (PNA) probes and its application to biological radiation dosimetry	86
Evaluation of wound contamination with heavy atoms by x-ray fluorescent spectrometry	88
< Improvement of Radiation Emergency Medical Systems in Japan and Asian Region >	
<i>Highlights</i>	
The status of radiation emergency medical systems in Japan since the accident at TEPCO's Fukushima Daiichi NPP	90
Improvement of radiation emergency medical systems in Asia	94
■ Development of Fundamental Technologies in Radiological Science	96
< Research toward the Development of Fundamental Technologies that Support the Use of Radiation >	
<i>Highlights</i>	
Research and development of focused proton microbeam irradiation system, SPICE for radio-biological studies	98
Research development of selective and precise measurement technologies of secondary high-LET particles in the radiation mixed fields	100
Analysis of lysosomal function in preimplantation mouse embryos	102
Immunogenicity of the differentiated cells derived from induced pluripotent stem cells	104

■ Fukushima Project Headquarters	106
<Project for Environmental Dynamics and Radiation Effects>	
<i>Highlight</i>	
Effects of the Fukushima Daiichi Nuclear Power Plant accident in wildlife of Fukushima Prefecture	108
< Worker's Health Follow-up Team, Project for Human Health>	
<i>Highlight</i>	
Project for human health (Workers' health follow-up team)	110
<Team of Dose Assessment for Fukushima Residents, Project for Human Health>	
<i>Highlight</i>	
NIRS external dose estimation system for Fukushima residents after	
the Fukushima Daiichi Nuclear Power Plant accident	112
<Radiation Effect Accumulation and Prevention Project>	
<i>Highlight</i>	
Research project for biological effects of low-dose-rate radiation and risk mitigation	116
■ Research on Evaluation of Medical Exposure	118
<i>Highlights</i>	
Investigations on frequencies and doses in X-ray CT examinations in pediatric hospitals	120
Estimations of pelvic organ doses in brachytherapy for cervical cancer patients	122
■ International Open Laboratory	124
<i>Highlights</i>	
Particle therapy molecular target unit, International open laboratory	126
Space radiation research unit, International open laboratory	128
■ Topics	130
Development of an innovative radiation monitoring system: Radi-Probe System	132
Development of the ⁶⁰ Co gamma-ray standard field for therapy-level dosimeter calibration in terms of	
absorbed dose to water	134
■ Organization Chart, Budget, Personnel, International Collaboration and Partnerships with Domestic and International Organizations and Universities	136
■ Appendix-1 (for FY 2011)	
List of Original Papers	142
■ Appendix-2 (for FY 2012)	
List of Original Papers	154



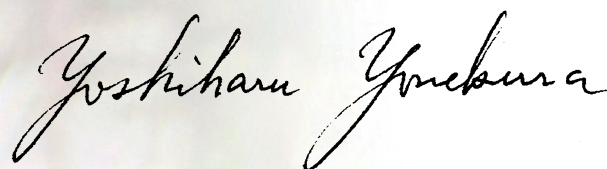
Preface

The National Institute of Radiological Sciences (NIRS) continues its scientific activities as Japan's leading research institution on radiation protection and promotion of radiological sciences. This annual report summarizes our accomplishments and research outcomes during the initial two years of the third mid-term plan from 2011 to 2015.

On March 11, 2011, just before starting this mid-term plan, the eastern part of Japan was hit by a huge earthquake and tsunami, and the events which followed triggered the severe nuclear accident in Fukushima Prefecture. NIRS directed our maximum efforts and activities toward emergency medical procedures coping with this nuclear accident. The Radiation Emergency Medical Assistant Team (REMAT), which was established in 2010, has made significant contributions to this mission. Training experts and professionals in radiological procedures and radiation protection is another important mission of NIRS, and its activity is expanding dramatically in responding to the requests of society.

In spite of such busy and difficult situations, NIRS has continued its activities for research and development in medical applications of radiological sciences. Carbon ion cancer therapy is now recognized as the most advanced and effective of radiotherapies for treatment of locally advanced cancers, maintaining excellent quality of life of the patients. The total number of patients who received this treatment has reached 7,000 cases since the first clinical trial in 1994. The technology is now being transferred to other institutions including facilities outside Japan. Molecular imaging, which can visualize molecular function in a living body, now serves as an essential tool for the accurate diagnosis of various diseases, including cancer, cardiovascular diseases, dementia and other neuropsychiatric diseases, and it is also expected to make a significant contribution in the development of new drugs. NIRS aims to serve as the nation's core institution for development of new technologies as well as for standardization and quality assurance of PET imaging technologies used for clinical research.

At the beginning of this third mid-term plan, I proposed three key targets for our activities: "Visible NIRS", "NIRS in the World" and "NIRS in History". With new challenges and opportunities, NIRS continues its maximum efforts to establish a solid base as a leading institution promoting comprehensive scientific research in a wide range of radiological sciences.



Yoshiharu Yonekura, M.D., Ph.D.

President



Outline of Research Activities

Makoto Akashi, M.D., Ph. D.
Executive Director for Research

The National Institute of Radiological Sciences (NIRS) was re-organized as an independent administrative institution in April 2001. Since then, NIRS scientists have been performing research studies according to the mid-term plans. Every 5 years, the mid-term plan has been revised: the first mid-term plan was started in April 2001; the second, in April 2006; and the third, in April 2011. Research activities at NIRS are done in five fields: heavy charged particle therapy, molecular imaging, radiation protection, radiation emergency medicine, and radiation technology. These mid-term plans have been carried out by four research centers and one fundamental technology center. In this report, the research activities at NIRS during the first and second years (FY 2011 and 2012: April 2011 to March 2013) of the third mid-term plan are presented.

The Great East Japan Earthquake measuring 9.0 on the Richter scale struck the northeast coast of Honshu, the main island of Japan, at 14:46 on March 11, 2011, triggering tsunami with over 10 meter-high waves. The earthquake was followed by numerous aftershocks. Although the operating reactors automatically shut down after the initial earthquake, damage primarily from the tsunami resulted in loss of electrical supplies for reactor cooling functions, which led to hydrogen explosions in some reactor units of the Fukushima Daiichi Nuclear Power Plant (NPP) of Tokyo Electric Power Company (TEPCO) that resulted in large amounts of radioactive materials, mainly I-131, Cs-134 and Cs-137, being released into the environment.

In April 2011, 3 weeks after the start of this huge disaster, NIRS began the third mid-term plan. Since NIRS is

designated as the national core center for radiation emergency medicine, we first had to respond to the disaster by: sending experts, receiving contaminated emergency workers, providing information on radiation and its effects to the public, and performing dose estimation. The people of Japan are still struggling with the effects of the multiple disasters, even though almost 2 years have passed and many NIRS researchers continue to be involved in response activities to the Fukushima accident.

The numbers of original papers published reached 214 and 251 in FY2011 and 2012, respectively and many of them were published in international journals of high reputation. Furthermore, more than 100 proceedings were presented at international and domestic scientific meetings, 806 oral presentations, and 95 patent applications. Collaborative studies and exchanges of researchers were also actively carried out: 268 collaborative studies were done, 812 researchers worked as visiting staff, and 277 students were accepted as trainees. In short, substantial, high level achievements have been realized by NIRS personnel and recognized by their peers, both domestically and internationally.

The Research Center for Charged Particle Therapy, as a leading research organization in this field, has conducted clinical, biological and physics research studies using heavy ions generated from the heavy ion medical accelerator in Chiba (HIMAC). In FY 2011, more than 650 patients were treated despite the confusion and extra work caused by the East Japan Great Earthquake. The clinical trial for lung cancer (single fraction) was completed in March 2012 and moved to the stage of clinical

practice in April 2012. In FY 2012, the clinical trial team started work with patients receiving carbon therapy with a newly installed scanning beam delivery system. The highlights of research progress in FY2011 and FY2012 are shown in other parts of this chapter.

The Molecular Imaging Research Center, consisting of four groups, has long experience with medical imaging technologies including positron emission tomography (PET) and magnetic resonance imaging (MRI). The Center conducts basic science and technology for molecular imaging and also application studies for diagnosis and pathophysiology of oncology and psychiatry. Current projects include the development of molecular probes and radiopharmaceutical production techniques and the investigation of measurement techniques for PET and MRI, in addition to preclinical and clinical applications in oncology and psychiatric and neurological diseases.

The Research Center for Radiation Protection has been providing a scientific basis for establishing regulations with global standards for radiation protection, security and safety, focusing on effects of low-dose radiation derived from human activities and from natural environmental radiation. For this purpose, the results of basic radiobiological research have been provided to promote understanding of radiation effects and to encourage enactment of more reasonable regulations for the safe and secure use of radiation in our lives. The Center has renewed its designation by the IAEA as a "Collaborating Centre for Biological Effects of Low Dose Radiation".

NIRS has been designated as the national center for radiation emergency medicine in Japan, providing direct or consultative services to local governments and hospitals in the event of an actual radiation incident. The Research Center for Radiation Emergency Medicine is responsible for services including providing exposed victims (patients) with the most advanced radiation emergency medicine treatments possible. Therefore, the Center has played important roles in medical response to the Fukushima accident. The Center also carries out activities to maintain and strengthen the emergency preparedness system fulfilling its role by establishing three nation-wide network councils for medicine, bio-dosimetry with chromosome analysis, and physical dosimetry. Furthermore, the Center conducted basic research studies on treatment of radiation exposure and dose estimation. The Center has also introduced several courses at NIRS on radiation emergency medical preparedness for medical professionals of the Asian region.

Research on radiation protection and radiation emergency medicine, an important mission of the institute since its establishment, has been carried out primarily in

two centers. These centers played a role as a national hub in collaboration with international organizations including the International Atomic Energy Agency (IAEA), International Commission on Radiological Protection (ICRP), United Nations Scientific Committee on the Effects of Atomic Radiation (UNSCEAR), and World Health Organization (WHO).

The Fundamental Technology Center, which was established to support various studies performed in NIRS with advanced fundamental technology, has been carrying out maintenance and quality control of institute accelerators including the single particle irradiation system to cell (SPICE), the PIXE (particle induced X-ray emission) analysis and tandem accelerator (PASTA), and the neutron exposure accelerator system for biological effects experiments (NASBEE), as well as radiation measurement apparatuses for cosmic rays. Efforts have also been extended to establish and support experimental animal laboratories for internal and external researchers.

In May 2012, the program for recovery of Fukushima was started. This program includes four research projects and a cooperation system. Research projects are the study for long-term and environmental effects of radiation, the health effect survey for emergency workers at the nuclear power plant, and the study of environmental dynamics of radionuclides and radiation in the ecosystems in the Fukushima region. The cooperation system is for collaboration with the Fukushima Medical University (FMU).

The second-term of the International Open Laboratory (IOL) also began in April 2011, for which four units were approved, including the "Particle Therapy Molecular Target Unit", the "Particle Beam Quality Unit", the "Space Radiation Research Unit", and "Radiation Response Model Unit". The purpose of the IOL is to conduct top level research by collaborating with distinguished scientists from leading research institutes world-wide and to promote further internationalization at NIRS by active research collaborations with foreign scientists. For the two years of FY 2011 and 2012, the IOL was involved in publication of 12 original articles and held three workshops/seminars.

Some other research programs have also been continued or newly started with the support of funding agencies including the Ministry of Education, Culture, Sports, Science and Technology (MEXT), the Ministry of Economy, Trade and Industry (METI), the Ministry of the Environment, and the Nuclear Regulation Agency.

In this report readers will be able to learn about substantial research that was performed in the 1st and 2nd years of the third mid-term plan. I would like to conclude with heartfelt thanks for cooperation and advice provided to us by all parties concerned.

Research on Cancer Therapy with Carbon Beams — Development of Human Friendly Cancer Therapy with Carbon Ion Beams —

Tadashi Kamada, M.D., Ph.D.

Director of Research Center for Charged Particle Therapy

E-mail: t_kamada@nirs.go.jp

The Research Center for Charged Particle Therapy (hereafter, abbreviated as “Center”) was established in 1993 when NIRS completed construction of the HIMAC. Since then its researchers have been carrying out clinical, biological and physics studies using heavy ions generated from the HIMAC. After accumulating many clinical experiences for carbon ion radiotherapy in various types of malignant tumors, the Center successfully obtained approval from the Ministry of Health, Welfare and Labor for “Highly Advanced Medical Technology” in 2003. Thus carbon ion therapy has achieved for itself a solid place in general practice of cancer treatment. The HIMAC has also served as a multi-user utilization facility for medical, biological and physics research and has been used by more than 700 researchers, including more than 100 foreign researchers.

In 2011, when the third Mid-Term Plan of NIRS was initiated, the Center was reorganized to conduct research on heavy ion beams using carbon ions and to develop more patient-friendly next generation heavy ion treatment system intensively. This will eventually contribute to progress in getting cancer cures and improved quality of life. The Center is organized as four research programs. In the Department of Physics; and the Hospital. Progress in research and practice in FY 2011 and FY 2012 are summarized briefly.

Research program for carbon ion therapy and diagnostic imaging (PL: Hiroshi Tsuji)

This program consists of the clinical trial research team, applied PET research team, applied MRI research team, and clinical database research team. According to the long-term objectives, research on developing advanced clinical therapy using carbon ion beam has been aggressively performed in FY 2011 and FY 2012. The clinical trial team has succeeded in having quite a large number of patients undergo carbon ion radiotherapy (C-ion RT) each year and a new clinical trial using the carbon ion scanning beam could be conducted. A total of more than 650 patients were treated with C-ion RT in FY 2011 despite the confusion after the Great East Japan Earthquake. Prostate, lung, head & neck, bone & soft tissue, liver tumors, post operative pelvic recurrence of rectal cancer, and pancreatic cancer are the leading 7 tumor types in the trials. The outcomes of C-ion RT in tumors that were hard to



cure with other modalities revealed quite high probability of local control, a survival benefit, and acceptable morbidity. In addition, clinical trials for establishment of hypofractionated C-ion RT in common cancers, such as lung cancer, liver cancer, and prostate cancer have also been successfully achieved. The ultra-short course C-ion RT trial for lung cancer (single fraction) was completed in March 2012 and was moved to clinical practice from April 2012. In FY 2012, the clinical trial team has set a record in the number of patients receiving carbon therapy with the aid of a newly installed scanning beam delivery system.

Medical physics research program for development of a novel irradiation system for charged particle therapy (PL: Toshiyuki Shirai)

The program consists of the beam delivery system research team, treatment planning system research team, radiation effect research team, experimental therapy research team, and image guided radiotherapy research team. On the basis of more than 15 years of experience with HIMAC, we have designed and constructed a new treatment research facility toward “adaptive cancer therapy” with heavy ions, which makes the one-day treatment of cancer easily. Further, the new treatment research facility should accurately treat a fixed target, a moving target with breathing and/or a target near a critical organ. For these purposes, a phase-controlled rescanning (PCR) method has been studied, especially for treating a moving target. A rotating gantry with the PCR method is also employed in order to increase the treatment accuracy for a tumor near a critical organ through the multi-field optimization method, and to reduce the patient’s load. The related R&D work has been carried out with HIMAC since April 2006. In September 2010, the treatment room E, which is one of the treatment rooms in the new treatment research facility, was

equipped with both the horizontal and vertical fixed beam-delivery systems. After a beam commissioning and pre-clinical study, the clinical study had been scheduled to start on 29 March 2011. The schedule was changed to May 2011, however, due to the massive earthquake in eastern Japan on 11 March 2011.

Advanced radiation biology research program (PL : Takashi Imai)

This program consists of the cancer system biology team, cancer metastasis research team, and radio-redox-response research team. These teams use different approaches to address the following research aims of the program.

Many favorable outcomes have been reported in clinical trials for carbon ion radiotherapy of several types of malignant tumors. However, some biological issues still remain to be resolved for the improvement of long-term survival. We have focused on the following fundamental issues:

- (1) Some tumor cells are pathologically indistinguishable from others, despite sometimes showing radio-resistance. What makes these tumor cells radio-resistant?
- (2) What causes distant metastases after local treatment? Are the metastatic cells simply overlooked before starting radiotherapy? If the metastatic cells are affected by irradiation, what are the molecular mechanisms? What types of tumor cells are susceptible to metastasis? How can we detect and suppress distant metastases?
- (3) How do reactive oxygen species generated by irradiation affect cellular functions? Can radioprotective agents, such as anti-reactive oxygen species, protect normal tissue surrounding tumor cells?

Through these studies, we have considered the effects of the genetic differences in the subjects or the experimental materials such as cell lines and mouse strains used on radio-sensitivity.

Research Program for the application of heavy ions in medical sciences (PL: Takeshi Murakami)

This program consists of the heavy ion radiotherapy promotion team, HIMAC research collaboration team, cellular and molecular biology research team, and international radiotherapy joint research team. This program mainly carried out the following activities in FY2011 and FY2012.

- (1) Promotion of carbon ion radiotherapy

A wide range of knowledge and know-how is required for promotion of carbon ion radiotherapy. Research and analyses of technical development, treatment procedures, and social environment concerning carbon ion radiotherapy were carried out. These results were assembled as review reports. Procedures transferring these results and know-how to new projects were also established. Contributions to new projects such as in Saga and Kanagawa were made.

- (2) Promotion of collaborative research, international as well as domestic

The research project with heavy ions at NIRS-HIMAC is the centerpiece of collaborative research using heavy ions. This program is deeply involved in the operation of the whole project. Since 1994 HIMAC at NIRS has been opened to researchers from all over the world in the field of ion beam sciences other than carbon beam radiotherapy. There are four experimental halls (Physics, Biology, Secondary beam and Medium-energy caves) as well as

three treatment rooms at HIMAC. During the daytime from Tuesday through Friday, HIMAC is operated for patient treatments. At nights and on weekends the four halls can be used for various experiments with ion beams. The latter framework is specified as "The Research Project with Heavy Ions at NIRS-HIMAC". A total of 123 proposals were accepted and carried out in FY2011 at HIMAC. The beam time of 5067 hours was supplied to those research studies. A total of 109 papers and 59 proceedings were published, and 331 papers were presented at various meetings. A total of 719 researchers participated in the project, including 122 foreign researchers in 15 international projects. The International Open Laboratory is the other framework for collaborative research. Two units of the IOL from the total four units are organized in this program.

Hospital, Research Center for Charged Particle Therapy (Director: Yutaka Ando)

The Research Center Hospital for Charged Particle Therapy of NIRS is unique in its specialization in radiotherapy for cancer. The hospital is designed for radiotherapy especially carbon ion therapy and consists of the oncology department, diagnostic radiology department and dental department. The hospital has 100 beds for inpatients and also handles 50-70 outpatients daily. The diagnostic radiology department has one CT-scanner with a 64-line detector, a 1.5 T MRI, a 3.0 T MRI, two PET/CTs, and one gamma camera. On the other hand, the oncology department has five fixed beam treatment rooms for carbon ion therapy (one vertical beam room, one horizontal beam room and three rooms with both beams) and one linear accelerator for x-ray therapy.

The hospital carries out radiotherapy using highly advanced medical technology and carries out clinical studies mainly using radiotherapy and diagnosis, and has a role as a tertiary hospital for radiation emergency medicine. The highly advanced medical technology started from 2003; the number of uses of this technology had reached 4,132 and the number of clinical studies had reached 3,139 in February 2013. From 1994 to January 2013 7,271 new patients have been treated with carbon ion therapy. In 2012 752 patients were treated with carbon ion therapy. The gender distribution of the patients treated by particle therapy was 513 males and 239 females; the ratio of male to female patients was 2.15 to 1. Patients living close to our facility reached 47.5% of total patients. In March 2012, we implemented the Electronic Medical Record (EMR) and developed a simple input method for each patient's findings, symptoms, tumor response, and toxic reactions that should be estimated by the physician during the clinical interview. We improved the coordination among several database systems (Hospital Information System, Therapy Plan Database, Treatment Management System, two PACSs and Radiology Information System for Radiation Therapy). These systems are connected to each other and data are transmitted to the destination systems.

Department of physics (Director: Koji Noda)

At present, the department of physics is one of the most active departments worldwide that are studying ion beam therapy as related to applied physics. For many years, reliable operation of HIMAC, a gigantic accelerator system, and the continuous development of novel techniques have been keeping us as a "center of excellence" in this field.

Highlight

Commissioning of the new ridge-filters and treatment planning system XiO-N

Yusuke Koba

E-mail: y-koba@nirs.go.jp

Introduction

In the HIMAC facility, the beam energies that have been used are 290 and 350 MeV/n in the vertical port and 290 and 400 MeV/n in the horizontal ports. Previously, a slight range shortage occasionally occurred in irradiations to deep-seated tumors in such parts as the pelvis, for which irregular patient positions were needed. A 3 cm longer range would have been able to reach most of those targets. To use a higher-energy beam, there were two problems. One was that the existing ridge filters could not shape a uniform dose distribution in the SOBP for the 430 MeV/n beam. The other was that the existing treatment planning system HIPLAN did not support addition of beam energy. We implemented new ridge filters and a new treatment planning system to solve these problems.

Methods

1) Improvement of Ridge-Filters

We added two therapeutic beam energies, 400 MeV/n for vertical ports and 430 MeV/n for horizontal ports. Then the maximum range was extended by 5 cm for the vertical and 3 cm for the horizontal ports. These higher-energy beams would be expected to have a sufficient range in most cases. But the old ridge filters were designed to optimize the SOBP distribution for the 290 MeV/n beam and they cannot shape a uniform dose distribution in the SOBP for the 430 MeV/n beam. In order to get an adequate distribution for all energies from 290 to 430 MeV/n, we redesigned all ridge-filters to optimize the SOBP distribution for an intermedi-

Table 1 Comparison of ridge-filter designs

	Old design	New design
Material	SOBP 25-120: Aluminum SOBP 150: Brass	all SOBP: Aluminum
Exchange of a ridge	difficult	easy
physics calculation	HIBRAG	Geant4
RBE model	Kanai 1999; Ref ^[1]	MKM2010; Ref ^[2]
Optimum energy	290 MeV/n	350 MeV/n
Applicable energies	290-400 MeV/n	290-430 MeV/n



ate energy, 350 MeV/n. Table 1 compares design specifications of the new and old ridge filters. The new ridge-filters were designed with the MKM2010 RBE model, which is identical to the model used for scanning irradiation treatment planning in the new treatment research facility at NIRS.

2) New Treatment Planning System XiO-N

The existing treatment planning system HIPLAN was developed when heavy particle radiotherapy was started at HIMAC. The dose-distribution calculation algorithm of HIPLAN adopted the parallel broad beam method. This method did not require powerful calculation capability, but it could not reproduce blurring and non-uniformity of distributions in the irradiation fields. Further, available beam energies for HIPLAN had been fixed from the design stage and therefore it would be difficult to add new beam energies. A high-precision treatment planning system XiO-N was developed jointly by NIRS, Mitsubishi Electric Corporation, and Elekta. Table 2 compares specifications of the existing and new treatment planning systems. The dose-distribution calculation algorithm of XiO-N adopts the divergent pencil beam method. By considering beam divergence and scattering effect, this system

Table 2 Comparison of treatment planning systems

	HIPLAN (Existing)	XiO-N (New)
Developers	NIRS & Asahi Kasei	NIRS, Mitsubishi & Elekta
Distribution	not for sale	Mitsubishi
Irradiation-field model	uniform approximation	wobbling
Algorithm	parallel broad beam	divergent pencil beam
Dose kernel	ideal calculation	actual measurement

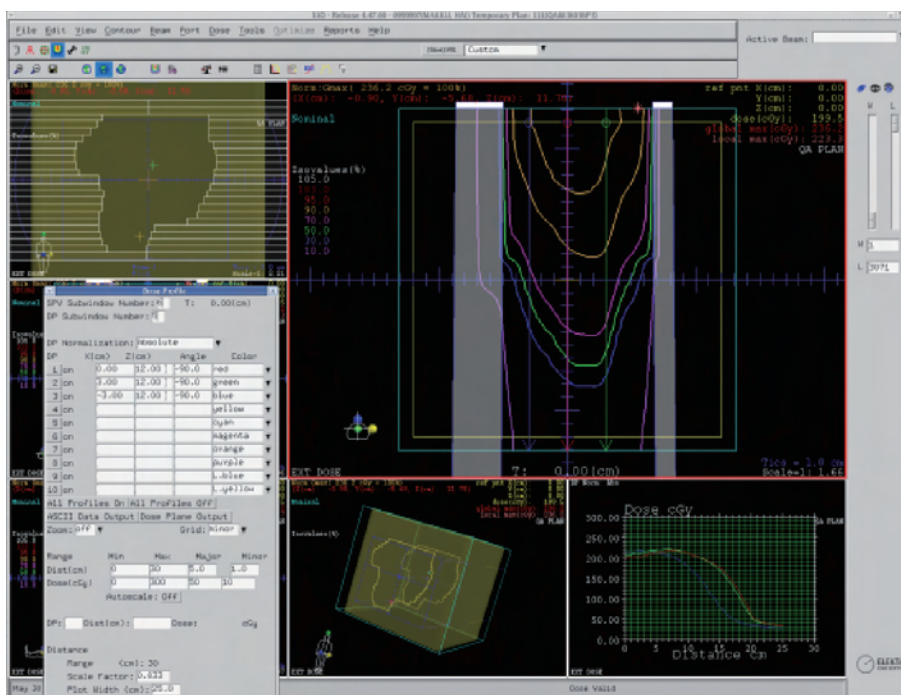


Fig.1 QA planning mode of XiO-N

calculates more precise distributions in the irradiation fields.

We measured depth dose distributions for all irradiation conditions and registered dose kernels of the pencil beam based on measurements into XiO-N. And we carried out interconnection tests with other treatment planning systems and peripheral equipment for irradiation.

Results and Discussion

We replaced the old ridge-filters with the improved design ridge-filters for the additional beam energy for broad beam irradiation and implemented the high-precision treatment planning system XiO-N. In the first half of FY 2012 there were 25 treatment cases using the new energy beam and XiO-N. For each treatment case we carried out confirmation of the system operation and verification of dose distribution. Using the QA planning mode of XiO-N, which is shown in Fig.1, the physical dose distribution in the water phantom which was irradiated at the treatment conditions for each patient was calculated. Quality of each treatment plan was assured by comparison of the calculated physical dose distribution with the measured distribution. Fig.2 shows example physical dose distributions of the QA measurements. Reasonable measured distributions were obtained and reliable assurance was confirmed.

In FY 2012, XiO-N was released for use in exceptional cases. Currently, the fraction of treatment plans made with XiO-N is about 20%. We are carrying out commissioning of the layer-stacking method and a motion-management technique against respiration for XiO-N. In FY 2013, XiO-N will be released for all cases and we will gradually be replacing all HIPLAN systems by XiO-N over several years.

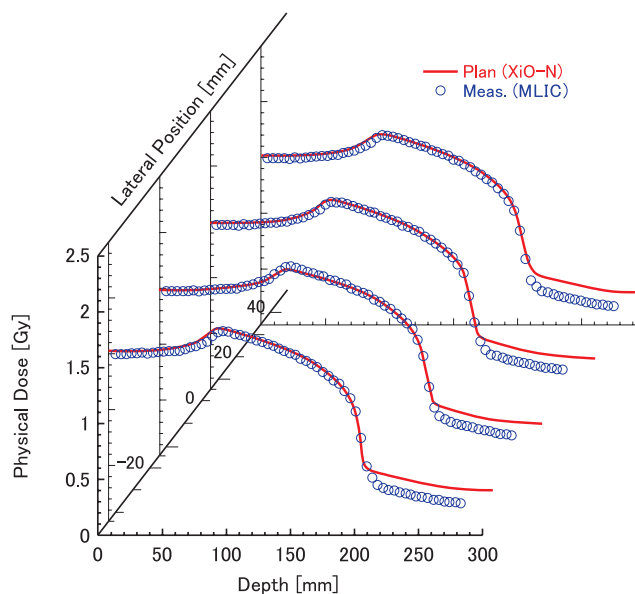


Fig.2 Physical dose distributions of QA measurements.

References

- [1] Kanai T, Endo M, Minohara S, *et al.*: Biophysical characteristics of HIMAC clinical irradiation system for heavy-ion radiation therapy, *Int J Radiat Oncol Biol Phys*, 44, 201-210, 1999.
- [2] Inaniwa T, Furukawa T, Kase Y, *et al.*: Treatment planning for a scanned carbon beam with a modified microdosimetric kinetic model, *Phys Med Biol*, 55, 6721-6737, 2010.

Highlight

Development of multiple-energy operation with extended flattops

Yoshiyuki Iwata

E-mail: y_iwata@nirs.go.jp

Heavy ion cancer therapy using the Heavy-Ion Medical Accelerator in Chiba (HIMAC) has been carried out since June 1994. The many successful cancer treatments have led us to construct a new treatment facility^[1]. This new facility is equipped with three treatment rooms, and three-dimensional raster-scanning irradiation with a pencil beam is employed for all the irradiation ports^[2]. In raster-scanning irradiation, a target is directly irradiated with high-energy heavy ions. The position of the focused beam on a target is controlled by the fast horizontal and vertical scanning magnets.

To control the depth dose-distribution, energy degraders, such as range shifters, consisting of PMMA plates having various thicknesses, are used in the present irradiation system with broad-beam irradiation. However, these range shifters may broaden the spot size of the beam on a target, and concurrently produce secondary fragments, which could adversely affect the depth dose-distribution. Since focused beams are used to irradiate a target in the raster-scanning irradiation method, it is preferable to change the beam energy directly by the accelerators, instead of using such energy degraders.

To change the energy of the beam, as provided by the synchrotron ring, we developed a multiple-energy operation with extended flattops. The proposed operation enables us to provide heavy ions having various energies in a single synchrotron cycle; namely, the beam energy would be successively changed within a single synchrotron pulse by an energy step, corresponding to a water range of 2 mm. With this operation, the beam range could be controlled without using any energy degraders, such as the range shifters, and hence an excellent depth dose-distribution could be obtained.

The multiple-energy operation employs operation patterns having a stepwise flattop, as schematically shown in Fig.1(a). With these operation patterns, the heavy ions injected in the ring are initially accelerated to the maximum energy, and then successively decelerated to lower energies. Although the stepwise pattern only has short flattops, where the beam can be extracted from the ring, we can extend the flattop and extract the beam during the extended flattop. Having consecutively extended the flattops, as illustrated in Fig.1(b), the beams having various energies can be

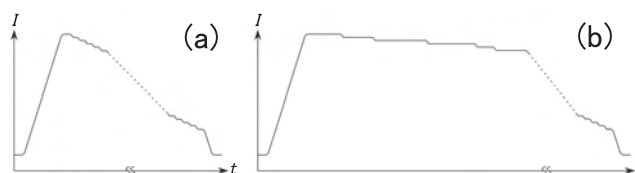
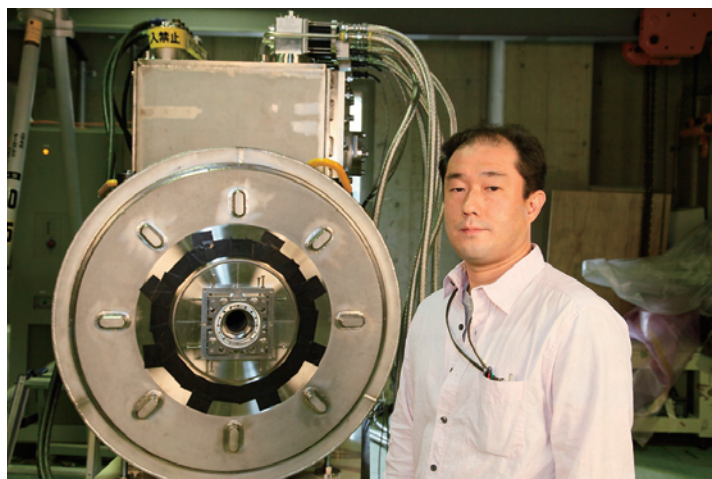


Fig. 1 (a) Schematic drawing of synchrotron pattern for multiple-energy operation. (b) The same pattern as (a), but with the extended flattops. The beam is extracted from the synchrotron ring during these extended flattops^[3].

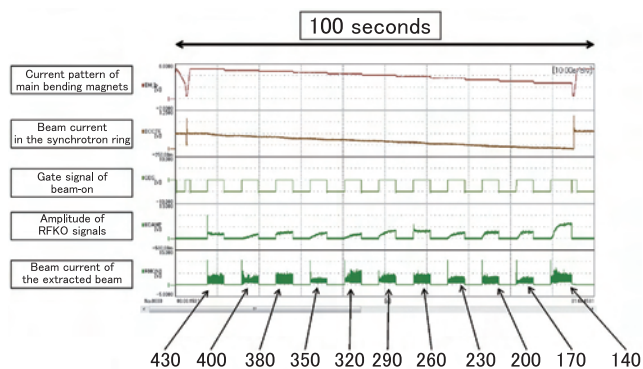


Fig. 2 Results of the beam acceleration test using the 11-flattop operation pattern. Beams having 11 different energies were successively extracted from the synchrotron ring.

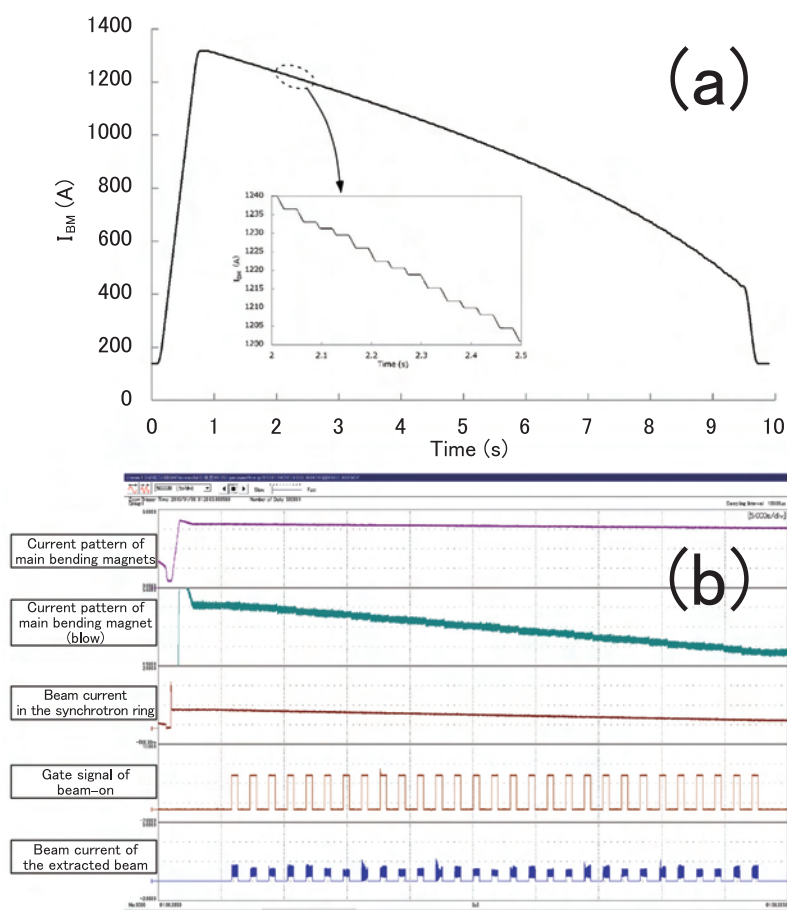


Fig. 3 (a) Current pattern for the main bending magnets in the ring as a function of time. (b) Results of the beam acceleration and extraction tests using the 201-flattop operation pattern.

extracted from the ring within a single synchrotron cycle, and hence the total irradiation time can be considerably reduced.

To prove the principle of multiple-energy operation with extended flattops, we have performed beam acceleration and extraction tests using the stepwise operation pattern. The pattern has 11 short flattops, corresponding to beam energies of 430, 400, 380, 350, 320, 290, 260, 230, 200, 170 and 140 MeV/u. A similar pattern was prepared for other devices, such as the main quadrupole, sextupole magnets, the RF-acceleration cavity, and the beam-extraction devices in the extraction channel. By using the prepared operation pattern, the beam will be first accelerated to 430 MeV/u, and then consecutively decelerated down to 140 MeV/u at an energy step of 20 MeV/u or 30 MeV/u. Results of the beam test are shown in Fig.2. Beams having 11 different energies were successively extracted from the synchrotron ring. The multiple-energy operation using this pattern was successfully commissioned and has been used for scanning treatments since FY 2012.

The final goal of this study is to control the depth dose-distribution only by varying the beam energy from the accelerators. To accomplish this, the beam energy has to be successively varied by an energy step corresponding to a water range of 1 mm or 2 mm. Since the maximum and minimum energies, as used in the raster-scanning irradiation, are 430 and 60 MeV/u, respectively, the synchrotron pattern having 201 flattops will be needed

to cover the entire energy range. Fig.3(a) shows the current pattern of the main bending magnets for the 201-flattop operation pattern. The beam energies at the first and last flattops are 430 and 56 MeV/u, respectively, and the difference in the beam energies between the neighboring short flattops correspond to a water range of 1 or 2 mm. Any of the 201 flattops can be extended, and the beam can be extracted during an extended flattop. Hence, with this 201-flattop operation pattern, designated the *universal pattern*, the depth dose-distribution could be controlled without using any energy degraders.

The beam acceleration and extraction tests using this universal operation pattern were made, and some results are given in Fig. 3 (b). As can be seen in the figure, the beams having various energies were successively extracted from the synchrotron ring. These results proved the effectiveness of the multiple energy operation. To commission and implement the multiple energy operation with the universal operation pattern to therapy, we will next undertake fine tuning of the operation pattern.

References

- [1] Noda K, Furukawa T, Fujimoto T, *et al.*: New treatment facility for heavy-ion cancer therapy at HIMAC, *Nucl Instrum Meth Phys Res B*, 266, 2182-2185, 2008.
- [2] Furukawa T, Inaniwa S, Sato S, *et al.*: Performance of the NIRS fast scanning system for heavy-ion radiotherapy, *Med Phys*, 37, 5672-5682, 2010.
- [3] Iwata Y, Kadowaki T, Uchiyama H, Fujimoto T, *et al.*: Multiple-energy operation with extended flattops at HIMAC, *Nucl Instrum Meth Phys Res A*, 624, 33-38, 2010.

Highlight

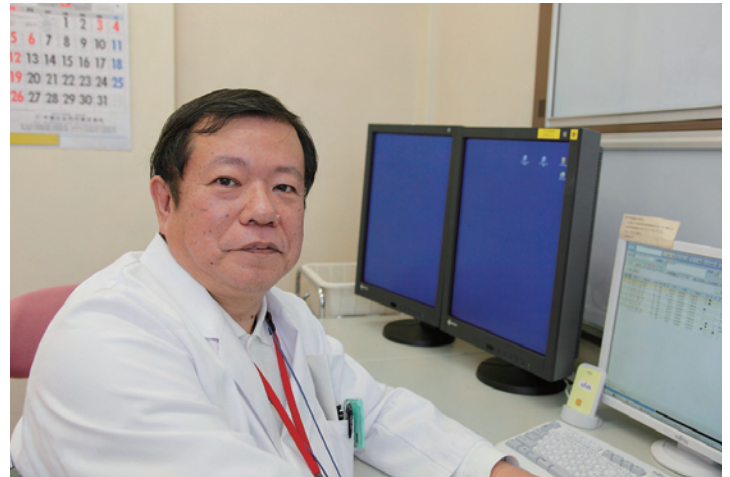
Research on the standardization and clarification of charged particle therapy

Hiroshi Tsuji

E-mail: h_tsuji@nirs.go.jp

Objectives

- To perform clinical research for clarifying usefulness of carbon ion therapy in order to establish new treatments for radioresistant tumors and to standardize the treatments for common cancers.
- To perform clinical research on utilization of the advanced technique of high-speed spot scanning irradiation of carbon ion beam in the routine treatment for head & neck or pelvic tumors.
- To investigate the benefits of improving accuracy of imaging modalities, such as PET, MRI, and CT scans for carbon ion therapy.
- To investigate the possibility of prediction or evaluation of effectiveness of carbon ion therapy using novel information from imaging modalities.
- To develop and regulate a comprehensive database on radiotherapy, mainly carbon ion therapy in consideration of achieving evidence based medicine. Additionally, to propose



a national database for multi-institutional research on particle therapy in domestic and foreign institutions.

Progress of Research

The Program of Research on the Standardization and Clarification of Charged Particle Therapy consists of the Clinical Trial Research Team, Applied PET Research Team, Applied MRI Research Team, and Clinical Database Research Team. All the teams are performing research and development on charged particle therapy. Progress of research in each team is summarized below.

Tumor sites for carbon ion radiotherapy at NIRS

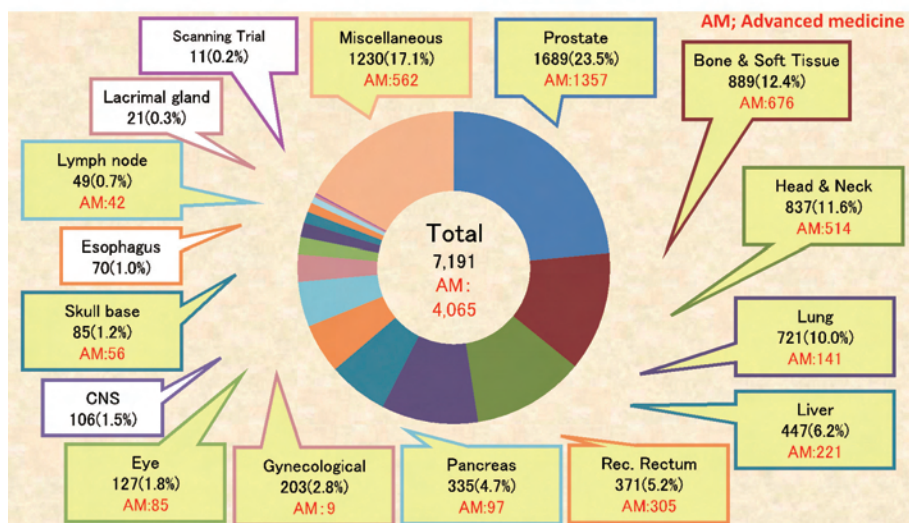


Fig.1 The numbers of patients for each tumor site treated with carbon ion beams.

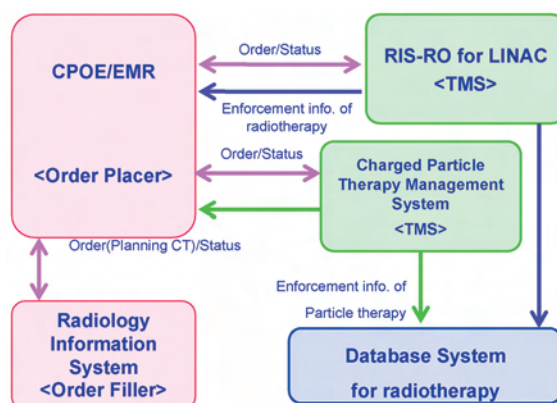


Fig.2 Current IT Systems and IHE Actor at NIRS.

1) Clinical Trial Research Team

As of December 2012, a total of 7,191 patients have been treated with carbon ion beam therapy at our institute. Carbon ion radiotherapy of these patients was carried out as more than 60 different phase I/II or phase II clinical trials or as advanced medicine treatments. Fig. 1 lists the numbers of patients for each tumor site

We treated 656 new patients from April 2012 to December 2012; that represents an increase of more than 100 compared to last year. Prostate, lung, head & neck, bone & soft tissue, and liver tumors are the 5 leading tumor types in the trials and recently the number of pancreatic tumors has been increased rapidly.

Scanning irradiation became available for the routine treatment of less mobile targets in the head & neck or pelvic region. Actually more than 100 patients could be safely and efficiently treated with scanning irradiation at the new treatment research facility.

New clinical trials for pancreas, esophagus, uterus and kidney cancers were proposed and permitted by the institute's ethical committee and some patients have already been enrolled. With advancement of hypofractionation for carbon ion therapy, the single session treatment for lung cancer and the 12-fraction treatment for prostate cancer could be established and their applications have started as advanced medicine treatments.

As a result of clinical research so far, it has been determined that carbon ion radiotherapy provided definite local control and offered a survival advantage without unacceptable morbidity in a variety of tumors that were hard to cure with other modalities. In addition, it was possible to implement hypofractionated radiotherapy using carbon ion beams, with application of larger doses per fraction and a reduction of overall treatment times as compared to conventional photon radiotherapy.

2) Applied PET Research Team

The PET respiratory gating system was modified for detecting respiratory signals at the end of the expiratory phase which is the same as can be achieved in the gated irradiation system for heavy ion radiotherapy. With this modification, we are able to fuse respiratory gating PET images with CT images for treatment planning taken in synchronization with the respiratory motion.

In order to judge applicability of carbon ion therapy, accurate diagnosis of lung metastasis is quite important in various cancers. To improve accuracy in diagnosis of lung nodules, we have carried out research on the usefulness of a computer aided diagnostic system and this year the environment (hardware and software)

for acquisition and analysis of actual patient data became available.

3) Applied MRI Research Team

To provide quantitative diagnostic information for heavy charged particle therapy, several MR methods, such as diffusion kurtosis imaging, quantitative dynamic contrast enhanced MRI, MR spectroscopy, and MR elastography have been proposed. Preliminary results about human MR elastography are reported in the Highlight section.

4) Clinical Database Research Team

We replaced the whole database system for clinical practice in March 2011. Historically, NIRS has built systems based on the IHE (Integrating the Healthcare Enterprise). In order to coordinate the Electronic Medical Record system / Computerized Physician Order Entry system (EMR/CPOE) and the charged particle therapy management system, we adopted the Enterprise Schedule workflow (ESI) integration profile proposed by the Radiation Oncology Domain of IHE this time. We defined the Order Placer (OP) Actor shown in ESI as the EMR/CPOE system and the TMS (Treatment Management System) Actor as the charged particle therapy management system as shown in Fig. 2. In addition, the coordination of these systems applied the transaction using the HL7 shown in ESI. This ensures interoperability and will also be effective in when updating the associated systems in the future.

In addition, we developed a prototype of a teaching file system for visiting researchers including persons from overseas institutions. With this system users can easily browse patient and image information via the DICOM Viewer by selecting a disorder of interest from the menu on a power-point navigation file. This year, we compiled 11 cases for each organ: head & neck, skull base, lung, liver, bone & soft tissue, prostate, kidney, and rectum. Such a system is quite useful to diffuse, standardize and educate researchers about charged particle radiotherapy.

References

- [1] Matsunobu A, Imai R, Kamada T, *et al.*: Impact of carbon ion radiotherapy for unresectable osteosarcoma of the trunk., *Cancer*, 118(18), 4555-4563, 2012, doi: 10.1002/cncr.27451(2012-09-15)
- [2] Okada T, Tsuji H, Kamada T, *et al.*: Carbon Ion Radiotherapy in Advanced Hypofractionated Regimens for Prostate Cancer: From 20 to 16 Fractions, *Int J Radiat Oncol Biol Phys*, 84(4), 968-972, 2012.
- [3] Shinoto M, Yamada S, Yasuda S, *et al.*: Phase 1 trial of preoperative, short-course carbon-ion radiotherapy for patients with resectable pancreatic cancer, *Cancer*, 111(1), 45-51, 2013.

Highlight

Gradient-vibrated MR elastography for charged particle radiation therapy assessment: A preliminary human study

Mikio Suga, Takayuki Obata*, Riwa Kishimoto, Hajime Ikeda, Shinya Ozawa, Atsuhisa Koyama, Hiroshi Ito, Tetsuya Wakayama, Takayuki Abe, Hiroshi Tsuji

*E-mail: t_obata@nirs.go.jp

Introduction

Magnetic resonance elastography (MRE) is a noninvasive technique for measuring tissue elasticity^[1]. In order to generate waves within the tissue, various external drivers have been proposed^[2]. Alternatively, Gallichan *et al.*^[3] suggested that the vibrations of the patient table that result from the impulse of an imaging gradient lobe could be used as a mechanical driving mechanism for MRE. The advantage of this approach is that it can be easily adapted for clinical application. Therefore, it has high potential to provide quantitative diagnostic information for charged particle radiation therapy.

In this study, we proposed gradient-vibrated MRE (GV-MRE) which consists of sinusoidally switching gradients for table vibration before a conventional MRE pulse sequence. To evaluate the elasticity of the brain using the specific mechanical resonance frequencies of the patient table, heterogeneous phantom and in vivo brain experiments were performed.

Materials and Methods

A spin-echo EPI MRE sequence (SE-EPI-MRE) was used for GV-MRE data acquisition (Fig. 1). Experiments were performed using a GE Signa HDx 3.0T. We directly measured the movement of the head coil on the MRI patient table during GV-MRE scanning using a laser Doppler vibrometer (Keyence Co., Ltd, SI-F10). The GV-MRE experiments were conducted on a tissue-simulating heterogeneous polyacrylamide (PAAm) gel phantom and a healthy 23-year-old male subject. The gel phantom was 160 mm long and constructed with five cylindrical inclusions (diameter 10, 15, 20, 30, and 40 mm; gel storage-modulus 6.8 kPa) inside a larger cyl-

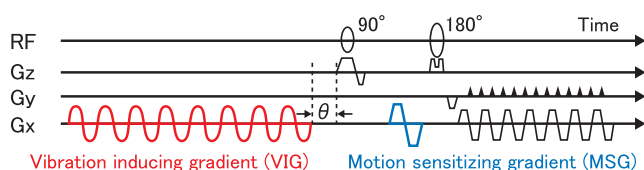


Fig. 1 SE-EPI-MRE sequence with vibration inducing gradient



inder (diameter 180 mm; gel storage-modulus 3.1 kPa). The imaging protocol for GV-MRE was: single-shot EPI, repetition time (TR) = 2000 ms, echo time (TE) = 65.2 ms (MSG=40 Hz) or 50.3 ms (MSG=57 Hz), field of view (FOV) = 192 x 192 mm² slices = 9, number of excitations = 1, MSG cycles = 1, phase offsets = 8, maximum MSG gradient = 3 (in vivo 40) mT/m, vibration-induced-gradient (VIG) and MSG frequency = 40 and 57 Hz, and VIG duration time = 1 s. VIG and MSG were applied on the x-axis. In order to calculate the elastogram, the local frequency estimation (LFE) method was applied.

Results

Fig. 2 shows the vibration amplitude of the patient table during GV-MRE scanning at each VIG frequency. The peaks at 32, 40, and 57 Hz have amplitudes of 27, 23, and 9 μm , respectively. Fig. 3 shows shear wave images and elastograms for the heterogeneous PAAm gel phantom. The estimated shear moduli are shown in Table 1. Fig. 4 presents shear wave images and elastograms for in vivo human brain. The estimated shear moduli are shown in Table 2.

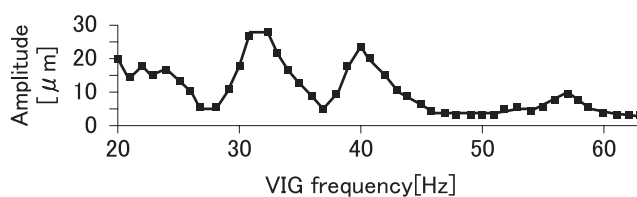


Fig. 2 Vibration amplitude of the patient table during MREwVIG scanning with a laser Doppler vibrometer

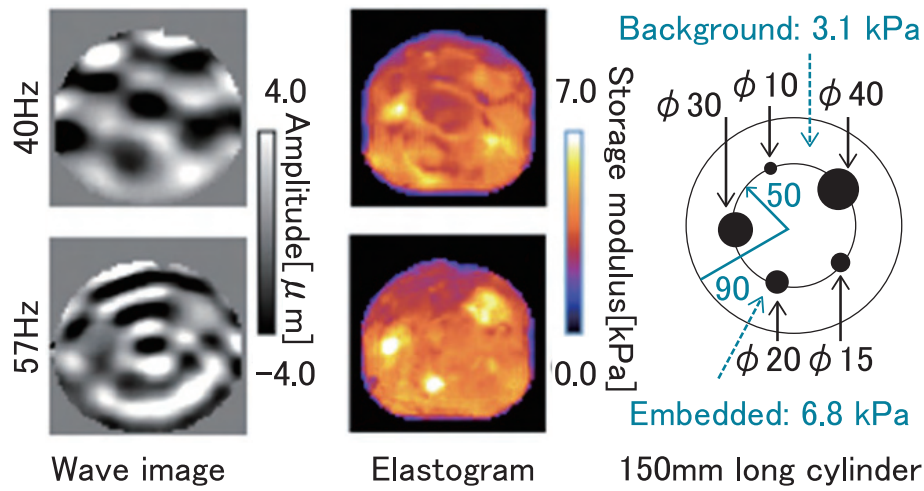


Fig. 3 Wave images and elastograms of the heterogeneous gel phantom. (ϕ : diameter)

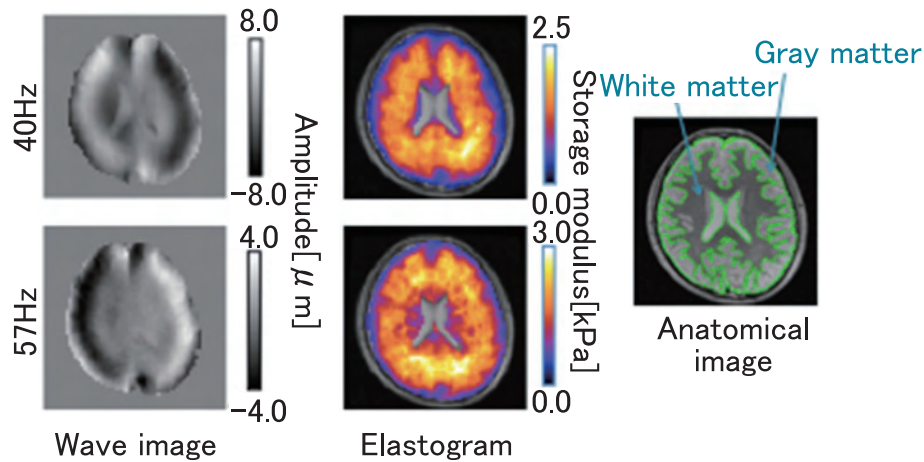


Fig. 4 Wave images and elastograms of in vivo human brain.

Table 1 Average storage-modulus of the heterogeneous phantom in each cylinder (Unit: kPa, ϕ : diameter, n/m: not measured)

	ϕ 10	ϕ 15	ϕ 20	ϕ 30	ϕ 40	background
40 Hz	n/m	5.8±0.4	3.5±0.5	5.3±1.0	4.1±0.4	3.5±0.5
57 Hz	n/m	5.0±0.3	3.9±0.3	5.7±1.0	5.6±0.6	3.9±0.3

Table 2 Average storage-modulus of *in-vivo* human brain in gray matter (GM) and white matter (WM) regions (Unit: kPa)

	GM	WM
40 Hz	1.2±0.7	1.7±0.7
57 Hz	1.7±0.8	1.8±1.2

Discussion

The phantom experiments show that the mechanical vibration of the patient table generates a shear wave of sufficient amplitude, but insufficient spatial resolution and accuracy at 40 Hz. The *in vivo* experiments at 40 Hz suggest that shear waves of sufficient amplitude to penetrate the whole brain can be generated and provide good contrast between gray and white matter. However, measurements at 57 Hz are less reliable in the deeper tissue.

Conclusion

In this study, we measured the vibration amplitude of the patient table during GV-MRE scanning as a function of VIG frequency and obtained clear *in vivo* elastograms using the specific mechanical resonance frequencies of the patient table. The results suggest that GV-MRE will enable quantitative measurements for charged particle radiation therapy assessment.

References

- [1] Muthupillai R, Lomas D.J, Rossman P.J, *et al.*: RL. Magnetic resonance elastography by direct visualization of propagating acoustic strain waves. *Science*, 269(5232), 1854-1857, 1995 Sep 29.
- [2] Uffmann K, Ladd ME. Actuation systems for MR elastography: design and applications. *IEEE Eng Med Biol Mag*, 27(3), 28-34, 2008 May-Jun.
- [3] Gallichan D, Robson MD, Bartsch A, : *Table-resonance elastography with MR*. *Magn Reson Med*, 62(3), 815-821, 2009 Sep.

Development of fast 3D scanning irradiation system

Toshiyuki Shirai

E-mail: t_shirai@nirs.go.jp

Particle therapy using carbon beams is a desirable cancer therapy due to the high dose localization and the high biological effect around the Bragg peak. We have developed a 3D scanning irradiation system to enhance these advantages. The scanning irradiation method has many good features; for example, it eliminates the need for compensating filters and collimators, and it is suitable for adaptive therapy. On the other hand, it has disadvantages such as a long irradiation time and the difficulties associated with moving target irradiation. At the New Particle Therapy Research Facilities in NIRS (Fig. 1), we have developed a fast 3D scanning system to solve these conventional problems^[1].

Fig. 1 shows a schematic view of the new facility and the existing HIMAC facility. There are three treatment rooms in the new facility. Two of them are equipped with fixed beam delivery systems in both the horizontal and vertical directions (Rooms E & F), and the other, now under construction, will be equipped with a rotating gantry (Room G). The heavy ion beam is provided from the HIMAC upper synchrotron. Table 1 shows the major parameters of the scanning beam delivery system. The maximum ion energy is designed to be ^{12}C , 430 MeV/n in order to obtain the residual range of 30 cm.

The most important feature of the NIRS scanning system is its speed; this shortens the irradiation time for patients and realizes the rescanning irradiation for the moving target within a reasonable time. We have achieved speeds 100 times faster than in past systems by improvements of the scanning system, the treatment planning system and the synchrotron operation. The horizontal scanning speed reaches 100 mm/ms. We have gotten a large increase in speed of not only the scanning power supply, but also the control and beam monitoring systems.

The clinical trial for therapeutic irradiation of patients was started on May 17, 2011 at Room E and finished on November 20. The number of the patients treated in the new facility was 11 and their targets were in pelvic and head regions. The irradiation area in the target was confirmed for each patient by observation of autoactivation using PET. Fig. 2 shows an example fusion image of



the treatment plan and the PET-CT image.

In the clinical operation of FY 2011, the beam range was con-

Table 1 Major parameters of beam delivery system.

Ion species	Carbon
Irradiation method	Scanning
Max. beam energy	430 MeV/n
Beam intensity	$1 \times 10^7 - 1 \times 10^9$ pps
Max. irradiation area	220 mm x 220 mm
Scanning speed	100 mm/ms (horizontal)

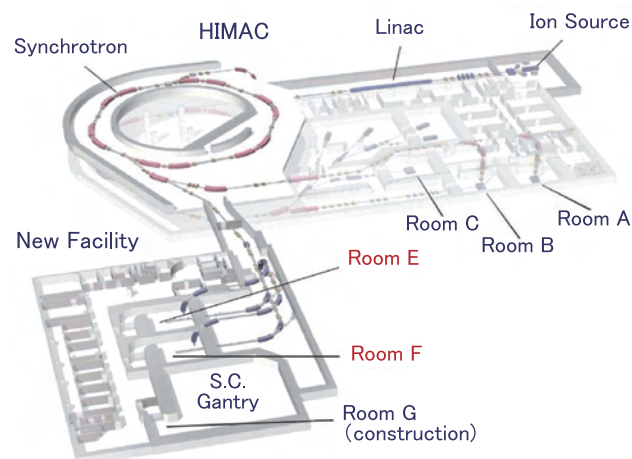


Fig. 1 Schematic view of the new facility (New Particle Therapy Research Facilities) and the existing HIMAC facility. When completed there will be three treatment rooms (E-G) in the new facility.

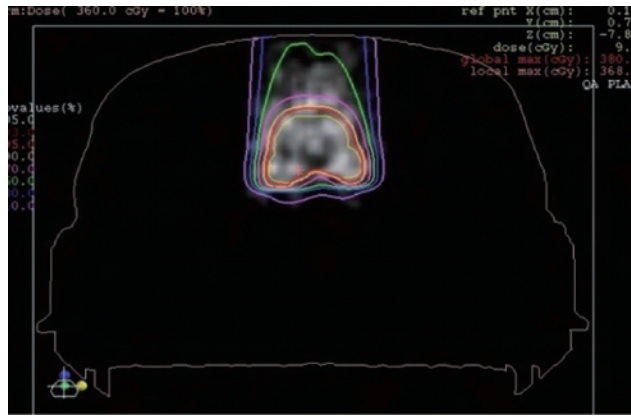


Fig.2 Cross-sectional view of the dose distribution in the treatment plan and the PET-CT image of the autoactivation. The green line shows the 50% contour line.

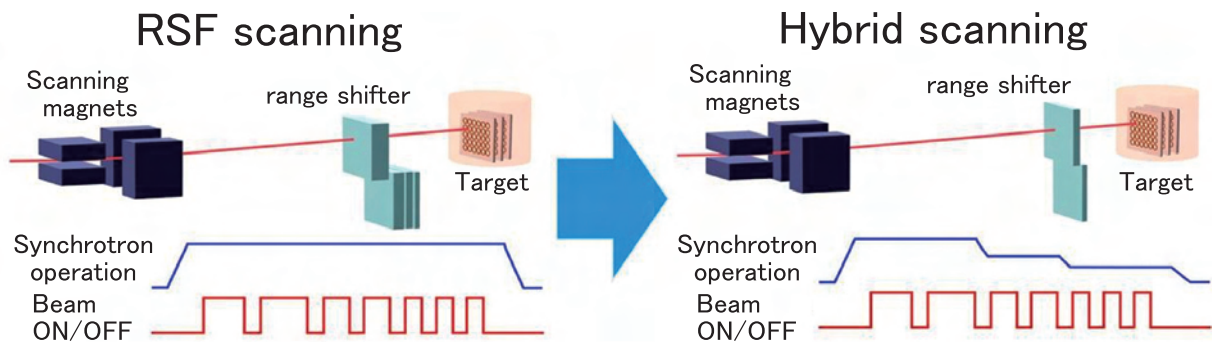


Fig.3 Comparison between the range shifter scanning and the hybrid depth scanning methods.

trolled by inserting PMMA plates with given thicknesses. This technique provides the desired range shift within a few hundred milliseconds. However, the range shifter plates increase the numbers of secondary fragments and multiple scattering, which can degrade the RBE and depth dose profile. It is preferable to change the beam energy directly from the synchrotron; however beam energies of more than 200 steps are necessary without range shifter, which leads to long adjustment and commissioning periods. We proposed a hybrid depth scanning method, where coarse tuning of the range (11 steps) is provided by the energy change of the synchrotron, while the fine tuning is provided by thin range shifter plates (Fig.3)^[2]. The dose conformity was improved considerably with hybrid depth scanning after a short commissioning period.

The carbon radiotherapy was restarted on September 11, 2012 in Rooms E and F using the hybrid depth scanning method. Through the end of FY 2012, the number of patient is 121 for the half year period. The average irradiation time has been 1.2 min with the PTV volume of 180 cc. The longest irradiation time has been 3.5 min with the maximum target volume of 1500 cc. The dose conformity has been improved and the irradiation time is comparable with that of the broad beam irradiation methods.

References

- [1] Furukawa T, Inaniwa T, Sato S, *et al.*: Performance of the NIRS fast scanning system for heavy-ion radiotherapy, *Med Phys*, 37, 5672-5682, 2010.
- [2] Inaniwa T, Furukawa T, Kanematsu N, *et al.*: Evaluation of hybrid depth scanning for carbon-ion radiotherapy, *Med Phys*, 39, 2820-2825, 2012.
- [3] Iwata Y, Uchiyama H, Fujimoto T, *et al.*: Multiple-energy operation with extended flattops at HIMAC, *Nucl Instrum Meth Phys Res A*, 624, 33-38, 2010.

Development of patient handling system

Toshiyuki Shirai

E-mail: t_shirai@nirs.go.jp

We set a goal of treating 1,000 patients per year for the design of the New Particle Therapy Research Facilities in NIRS; this is the target number for other recent carbon ion radiotherapy facilities. The following conditions are assumed and a simple calculation shows that the goal is met:

- (1) Treatment time of 6 hours/day and treatment period of 170 days/year;
- (2) Average fraction number of 12;
- (3) Average treatment room occupation time of 15 min; and
- (4) Treatment room number of 3.

The treatment room occupation time in assumption (3) is a key point for the goal realization. While the irradiation time is less than 5 min with the passive and scanning beam delivery system, most of the room occupation time is spent for the patient setup and positioning using the imaging system. These techniques for patients are called the patient handling system (PTH) and we have developed and tested hardware and software applications for them.

The PTH covers a wide range of functions including X-ray/CT imaging, geometrical/position accuracy including motion management (immobilization, robotic arm treatment bed), layout of the treatment room, workflow in the treatment room, software, and others^[1]. Fig. 1 shows a block diagram of the complete treatment system for scanning irradiation. The patient information is transferred from the Hospital Information System (HIS) through the Treatment Management System (TMS) to three subsystems; Scanning Irradiation System (S-IR), Treatment Planning System (TPS) and PTH. The treatment data such as plans and records are stored in DICOM-RT PACS and accessed by each subsystem.

Fig. 2 shows the treatment floor in the new facility. It has three treatment rooms (Rooms E, F & G) including one gantry room. Fig. 3 shows treatment Room E. This room has the SCARA-type (selective compliance assembly robot arm-type) robotic arm with a treatment table. Linear movements of 2400 mm, 600 mm, and ± 300 mm are possible in the longitudinal, vertical, and lateral directions, respectively. Rotational movements are -15° to 195° for rotation (isocentric), $\pm 20^\circ$ for roll, and $\pm 5^\circ$ for pitch. Absolute and relative position accuracies are within the range of spheres of 0.5



mm and 0.3 mm diameter, respectively.

The PTH includes orthogonal (vertical and horizontal directions) X-ray imaging systems with flat panel detectors (FPDs) for patient position verification. All FPDs are installed within the port cover, and the vertical X-ray tube is set under the floor. The horizontal X-ray tube is moved down when it is used. For respiratory gated treatment, the DFPDs are installed on the right and left sides of the vertical irradiation port, and the respective X-ray tubes are installed under the floor. The tumor position during the irradiation will be observed continuously using two oblique X-ray fluoroscopic units.

The PTH also includes several custom software applications to

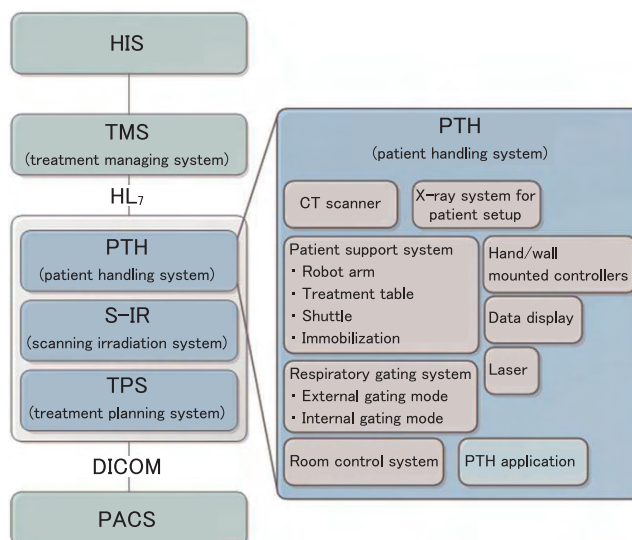


Fig. 1 Block diagram of the treatment system for scanning irradiation.

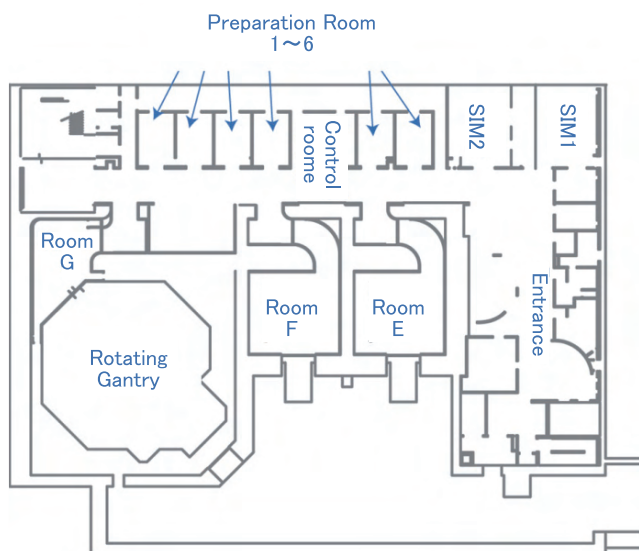


Fig.2 Layout of the treatment floor on the second basement level of the New Particle Therapy Research Facilities.



Fig.3 Treatment Room E with two fixed beam ports and SCARA-type robotic arm.



Fig.4 User interface of the patient position verification application.

facilitate treatment workflow. Fig.4 shows the graphical user interface of the patient position verification application, which has functions of landmark-based manual registration and GPU-based 2D/3D auto-registration. For the patient position verification, DRR (Digitally Reconstructed Radiography) images are provided from planning CT images^[2] and compared with the FPD images by the 2D/3D auto registration software. The result of the registration is transmitted to the robotic arm and the patient position is adjusted semi-automatically.

On May 17, 2011, the clinical trial was started for 11 patients with tumors of the head and neck (5 patients), prostate (3 patients), and pelvis (3 patients). The treatment room occupation time averaged over all patients was 20 min. Of the total, 3 min were for preparation of the patient (including immobilization), 12 min for patient positioning, 2 min for irradiation (including preparation) and 3 min for exit. Residual errors in translation and rotation

averaged over all patients were 0.4 mm/0.2° at the end of the clinical trial^[3]. In the clinical operation in FY 2012, the treatment room occupation time dropped to 13 min on average. The patient positioning time was lowered to 7 min, while other times were almost the same. We believe that PTH is important to improve the efficiency and precision of the treatment and reach the goal of the treatment room occupation time.

References

- [1] Mori S, Shirai T, Takei Y, *et al.*: Patient Handling System for Carbon-ion Beam Scanning Therapy, *J Appl Clin Med Phys*, 13, 3926, 2012.
- [2] Mori S, Inaniwa T, Kuwae T, *et al.*: Development of Digital Reconstructed Radiography Software at New Treatment Facility for Carbon-ion Beam Scanning of National Institute of Radiological Sciences, *Australas Phys Eng Sci Med*, 35, 221-229, 2012.
- [3] Mori S, Shibayama K, Tanimoto K, *et al.*: First clinical experience in carbon-ion scanning beam therapy: retrospective analysis of patient positional accuracy, *J Radiat Res*, 53, 760-768, 2012.

Highlight

Irradiation alters the invasive potential of pancreatic cancer cell lines, MIAPaCa-2 and PANC-1, via altering protease activities, and also affects mesenchymal and amoeboid modes of motility

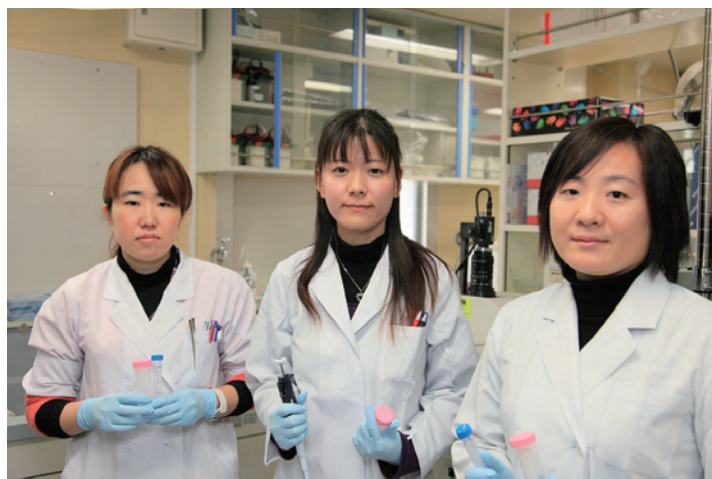
Mayumi Fujita, Kaori Imadome, Yoshimi Shoji, Takashi Imai

E-mail: mafujita@nirs.go.jp

In order to elucidate effects of local radiotherapy on the characteristics of metastatic tumors, it is fundamental to understand the nature of motility in irradiated tumor cells; this will, in turn, facilitate the development of effective strategies to counter tumor cell motility, for use in combination with radiotherapy. It is known that tumor cells invade by two modes of motility—mesenchymal and amoeboid. Tumor cells with the mesenchymal mode of motility are known to use proteolytic enzymes, such as matrix metalloproteinases (MMPs) and serine proteases (SerPs), to create a path to move through the ECM. In contrast, cells with the amoeboid mode of motility, which are rounded, exhibit a protease-independent mechanism of invasion; this mechanism is based on actomyosin contractility and is dependent on Rho/ROCK signaling. Evidence shows that cells can shift between these two modes of motility depending on the environmental conditions; this may limit the effectiveness of single therapeutic agents, such as MMP inhibitors (MMPIs), which are directed at inhibiting a single mode of tumor cell motility. Under these circumstances, understanding cancer cell motility is critical for the effective use of inhibitors.

Both *in vitro* and *in vivo* studies have shown that photon irradiation enhances the metastatic potential of tumor cells. On the other hand, C-ion irradiation is known to diminish the invasive potential of several cancer cell lines. We also found from *in vitro* studies that X-ray irradiation enhanced the invasiveness of pancreatic cancer cell lines, MIAPaCa-2 and PANC-1, whereas C-ion irradiation effectively suppressed the invasive potential of MIAPaCa-2, BxPC-3, and AsPC-1 cells; however, we observed that C-ion irradiation enhanced invasion in PANC-1 cells^[1,2]. To the best of our knowledge, no study has been conducted to examine the invasiveness of cells with mesenchymal and amoeboid modes of motility after exposure to radiation. To clarify the mechanisms of different invasiveness of such irradiated pancreatic cancer cell lines, we used MIAPaCa-2 and PANC-1 cells to investigate the effects of irradiation on invasiveness focusing on the modes of motility.

We found that X-ray-induced MIAPaCa-2 invasion was associated with induction of MMP-2 expression and its activity, and inducing the amoeboid-mesenchymal transition to some extent^[1]. MIAPaCa-2 cells are morphologically heterogeneous, including both mesenchymal and amoeboid modes (Fig.1). In accordance



with this, we demonstrated that the combination of MMPI and ROCK inhibitor (ROCKI), which blocks both mesenchymal and amoeboid movements, was needed to suppress MIAPaCa-2 invasiveness, whereas the single use of MMPI only slightly reduced the invasiveness, and in the case of ROCKI, it even enhanced the invasion (Fig.2). C-ion irradiation, on the other hand, suppressed the expression and activation of MMP-2, which resulted in reduced invasion^[2]. The effect of C-ion irradiation on the amoeboid type of invasion was unknown and further research is needed.

PANC-1 cells have no rounded cells, which suggested that PANC-1 invasiveness is dependent on proteolysis. Indeed, MMP-2 was significant for X-ray-induced PANC-1 invasion^[1]. However, in contrast to MIAPaCa-2, C-ion enhanced PANC-1 invasion via the activation of SerP, such as plasmin, and uPA^[2]. Inhibition of the

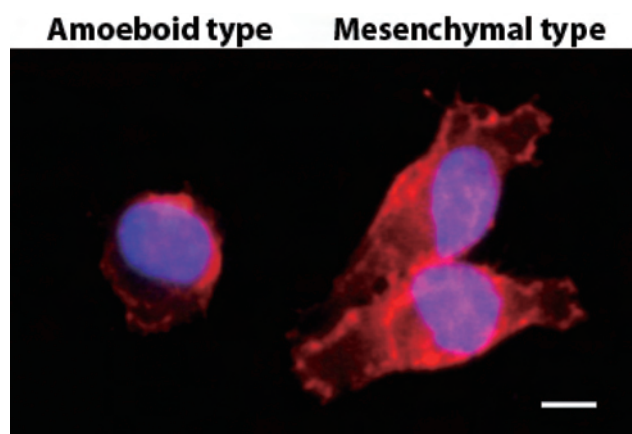


Fig.1 MIAPaCa-2 cells with typical mesenchymal-type and amoeboid-type morphology were shown^[1].

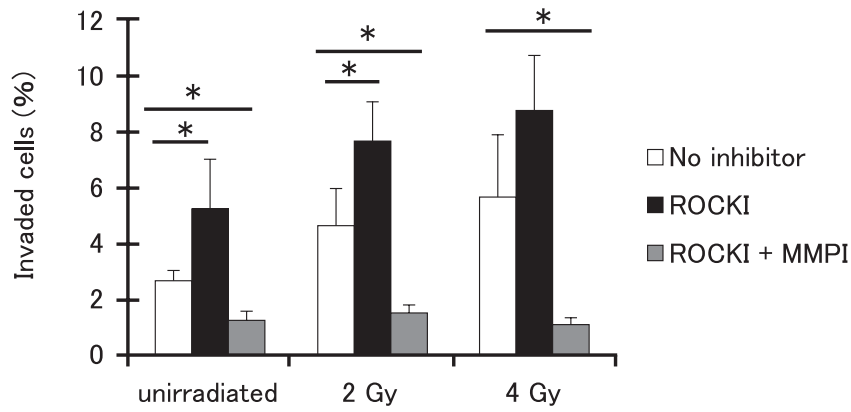


Fig.2 The effects of MMPI and ROCKI on the invasiveness of MIAPaCa-2 cells. Invasion assay was performed with addition of ROCKI or ROCKI plus MMPI. Data represent the mean±SD of samples (n = 6). *P < 0.05 vs. control^[1].

functioning protease, SerP, however, failed to reduce C-ion-enhanced PANC-1 invasion because C-ion-irradiated PANC-1 cells exhibited the ability to undergo the mesenchymal-amoeboid transition (Fig.3). To block both mesenchymal and amoeboid invasions of C-ion-irradiated PANC-1 cells, we treated PANC-1 cells with SerP inhibitor (SerPI) plus a ROCKI; this resulted in effective reduction of C-ion-irradiated PANC-1 invasion (Fig.4).

Over all, we found that irradiation alters the invasive potential of MIAPaCa-2 and PANC-1 via altering functioning protease expression and its activities, and it also affects mesenchymal and amoeboid mode transition. Since the ability of transition between these two modes of motility could allow the cells to invade adjacent tissues via either protease-dependent or protease-independent mechanisms depending on the environmental conditions, blocking of both mesenchymal and amoeboid motilities is necessary for such cell types. We note that PANC-1 invasion was only enhanced after the C-ion irradiation among four pancreatic cancer cell lines; this is the first report that C-ion irradiation enhanced the invasive potential of a tumor cell line *in vitro*. It is still unclear how C-ion irradiation generates such cell-specific effects, and further investigations, such as research on the genetic background of target tumors, will be required.

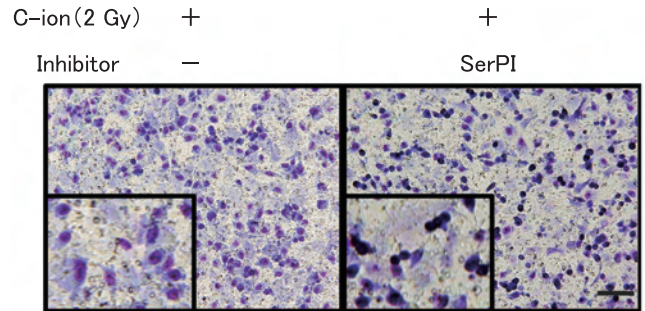


Fig.3 The effects of SerPI on the mode of motility of C-ion-irradiated PANC-1 invasion. Morphology of invaded PANC-1 cells with SerPI is shown. Bar = 200 μm^[2].

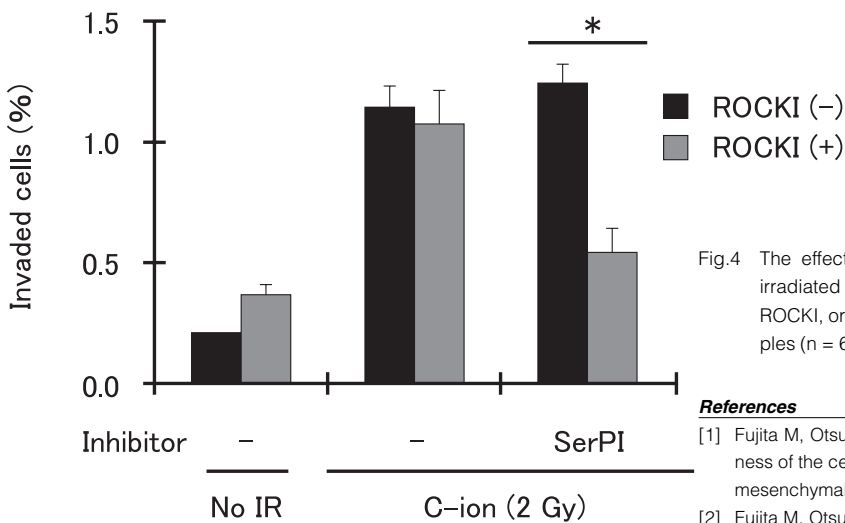


Fig.4 The effects of SerPI plus ROCKI on the invasiveness of C-ion-irradiated PANC-1. Invasion assay was performed with addition of ROCKI, or ROCKI plus SerPI. Data represent the mean±SD of samples (n = 6). *P < 0.05 vs. control^[2].

References

- [1] Fujita M, Otsuka Y, Yamada S, *et al.*: inhibitor additively induce invasiveness of the cells of the pancreatic cancer line, MIAPaCa-2, which exhibits mesenchymal and amoeboid motility, *Cancer Sci.* 102(4), 792-798, 2011.
- [2] Fujita M, Otsuka Y, Imadome K, *et al.*: Carbon-ion radiation enhances migration ability and invasiveness of the pancreatic cancer cell, PANC-1, *in vitro*, *Cancer Sci.* 103(4), 677-683, 2012.

Highlight

Inherent factors in radiosensitivity to high linear energy transfer carbon ions (C-ions) in normal lung tissue

Miyako Nakawatari, Kaori Imadome,
Takashi Moritake, Takashi Imai*

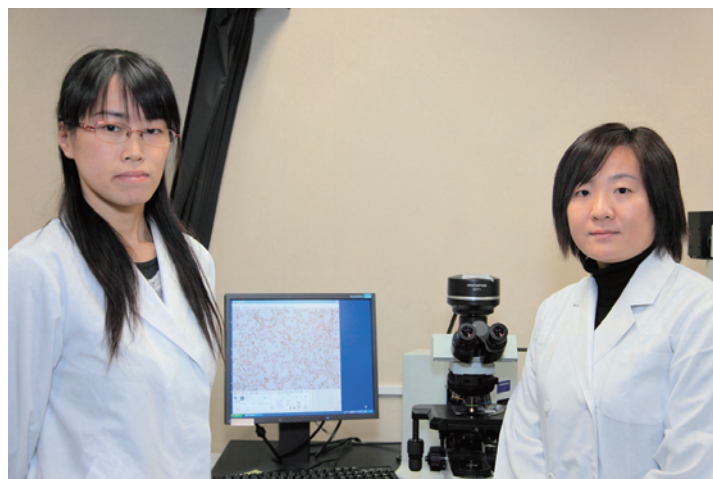
*E-mail: imait@nirs.go.jp

Summary

We investigated whether inherent factors produced variance in mouse lung morbidity in response to C-ions. Three strains of female mice (C3H/He Slc, C57BL/6J Jms Slc, and A/J Jms Slc) were locally irradiated in the thorax with either C-ion beams (290 MeV/n, in 6 cm spread-out Bragg peak) or with ^{137}Cs γ -rays as a reference beam. The survival data in mice showed a between-strain variance after C-ion irradiation with 10 Gy. The median survival time of C3H/He was significantly shortened after C-ion irradiation at a higher dose of 12.5 Gy. Histologic examination of the lung revealed early-phase hemorrhagic pneumonitis in C3H/He and late-phase focal fibrotic lesions in C57BL/6J after C-ion irradiation with 10 Gy. Pleural effusion was observed in C57BL/6J and A/J mice at 168 days after C-ion irradiation with 10 Gy. We identified candidate genes, *Gdf15* and *Has1*, which were differentially expressed between C-ion and γ -ray irradiation with strain-dependent changes. Immunohistochemical staining showed that the number of CD44-positive cells and Mac3-positive cells varied significantly among the three mouse strains during the early phase. These data demonstrated a strain-dependent differential response in mice to C-ion thoracic irradiation. Our findings also provided candidate molecules that could be implicated in the between-strain variance to early hemorrhagic pneumonitis after C-ion irradiation.

Introduction

Carbon ion therapy has gained increasing attention in the last decade because it spares normal tissue and gives improved tumor control. One important target cancer for C-ion radiation therapy is lung cancer, which has been the leading cause of cancer-related death in Japan^[1]. Dose escalation using C-ions is a promising approach especially for locally advanced non-small cell lung cancer. Despite recent technological advancements in C-ion irradiation, occasional cases of radiation pneumonitis occur^[2]. The ability to identify which patients are at risk of C-ion-induced lung injury would allow for safer and more efficient therapy with patient-specific regimens. The presence of individual or strain differences in lung radiosensitivity to low-LET irradiation has been well established. Although the diversity in sensitivity of individual



tumor cells to C-ions is known to be smaller than for photon irradiation, little is known about the inherent factor(s) involved in radiosensitivity to high-LET C-ions in normal lung tissue. Thus, in this study, we performed whole-lung C-ion irradiation using three different strains of mice to examine whether strain-dependent differences in radiation effects occur in C-ion thoracic irradiation.

Mice survival study and histologic examination after C-ion irradiation

A difference in mouse strains was demonstrated in the survival assay after 10 Gy of thoracic C-ion irradiation within a period of 180 days; almost all C57BL/6J mice had died by 6 months, while most of the C3H/He mice were still alive at 6 months. Survival curves after γ -irradiation showed a different manner of between-strain variance after 15 Gy and 20 Gy. The median survival time of C3H/He mice after γ -irradiation was significantly shortened as the dose was increased from 10 Gy to 15 Gy and 20 Gy. Similarly, the median survival time of C3H/He mice after C-ion irradiation was significantly shortened as the dose was increased from 10 Gy to 12.5 Gy.

All strains showed intra-alveolar hemorrhage at 56 days and 84 days after C-ion irradiation, which is defined as the presence of red blood cells in the alveolar space (Fig. 1). C3H/He mice showed (++) hemorrhage at 56 days after irradiation in 2 of 10 mice without evidence of ruptured vessel walls (Fig. 1b). This hemorrhage in C3H/He was gradually resolved by 84 days (Fig. 1c), and 10 Gy of C-ion irradiation did not lead to lethality. In contrast, C57BL/6J mice showed only slight microscopic hemorrhage (Figs. 1e and f). At 168 days after irradiation, intraalveolar hemorrhage was not seen in any of the strains. The data of C3H/He mice showing diffuse hemorrhagic alveolitis at 2-3 months after C-ion irradiation with 10 Gy may have led to the waves of death in the C3

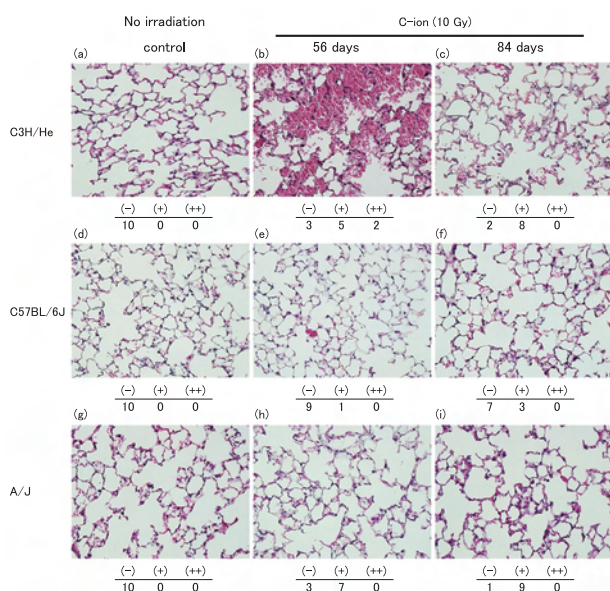


Fig.1 Representative findings of hematoxylin and eosin-stained sections (X20 objective) after carbon ion irradiation with 10 Gy (n = 10). The number of mice for each criteria (per 10 mice) : (-)=no hemorrhage; (+) = hemorrhage observed microscopically (X40 objective); (++) = hemorrhage observed microscopically (X10 objective)^[3].

H/He mice at the higher dose of 12.5 Gy. On the other hand, C57BL/6J and A/J mice developed pleural effusion with focally fibrotic lesions at 6 months. Thus, our study reveals that strain-related differences in lung morbidity are also evident with high-LET C-ion irradiation.

Identification of C-ion irradiation-responsive genes with strain differences in expression

We performed gene expression analysis using right lung lobes taken after C-ion or γ -irradiation with a dose of 10 Gy to select genes potentially associated with strain differences in response to C-ion irradiation. Microarray analysis identified differential expression changes in *growth differentiation factor 15 (Gdf15)* and *hyaluronan synthase 1 (Has1)*. In quantitative RT-PCR, we observed elevated *Gdf15* and *Has1* expression at 6 hours after C-ion irradiation in all strains (Figs. 2a and b), which remained elevated for 12 weeks in C3H/He and C57BL/6J mice (Figs. 2c and d), although expression amounts of both genes were clearly higher in C57BL/6J than in C3H/He.

Gdf15 is a murine ortholog of human macrophage inhibitory cytokine-1, which regulates inflammation after injury as well as acts as an autocrine inhibitor of macrophage activation. Hyaluronic acid (HA) is a component of the extracellular-matrix. *Has1* is one of the 3 HA synthase isoforms (*Has1*, *Has2*, and *Has3*) that are expressed at a higher level in growing cells than in resting cells. Our data indicate that the expression level of particular early-responsive genes is related to those cytokines or extracellular-matrix components and support the notion that these molecules may be involved in the mechanism that causes early hemorrhagic pneumonitis.

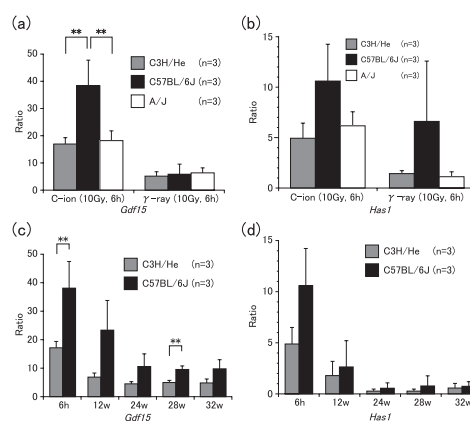


Fig.2 Quantification of mRNA expression levels for *Gdf15* (a) and *Has1* (b) 6 h after carbon ion or γ -ray irradiation with 10 Gy. Trend in expression levels up to 32 weeks for *Gdf15* (c) and *Has1* (d). Relative values are plotted in comparison with the corresponding preirradiated samples, and data are expressed as ratios (n = 3; **P < 0.05, Student *t* test)^[3].

Immunohistochemical analysis of HA, CD44, and Mac3 expression

The number of CD44-positive cells, a surrogate marker for HA accumulation, showed differences between strains from 14 days to 84 days after C-ion irradiation. Similarly, the number of Mac3-positive cells, a marker for macrophage infiltration in irradiated lung, showed interstrain variance from 14 days to 56 days after C-ion irradiation. Because most CD44-positive cells corresponded to alveolar macrophages based on hematoxylin-eosin staining (data not shown), the fraction of CD44-positive macrophages was expressed as the ratio of CD44/Mac3 positive cells for descriptive purposes. This analysis clearly demonstrated the strain differences from 14 days to 84 days. These findings imply that the elevated expression of CD44 on macrophages, seen in C3H/He mice, accelerates the clearance of degraded HA from the extracellular-matrix. This promotes the migration of macrophages into the alveolar space or into the interstitium during the early phase, which may consequently evoke pneumonitis with intra-alveolar hemorrhage.

In planning radiation therapy for lung cancer, it is critically important to be able to predict whether an adverse effect such as radiation pneumonitis is likely to develop for a particular patient. Because both bronchoscopy and bronchoalveolar lavage are common procedures in therapy as well as diagnosis for illness, then measurement of the number of CD44-positive and Mac3-positive cells in bronchoalveolar lavage fluid before and during radiation therapy will be useful to minimize the adverse effects of early-phase pneumonitis.

References

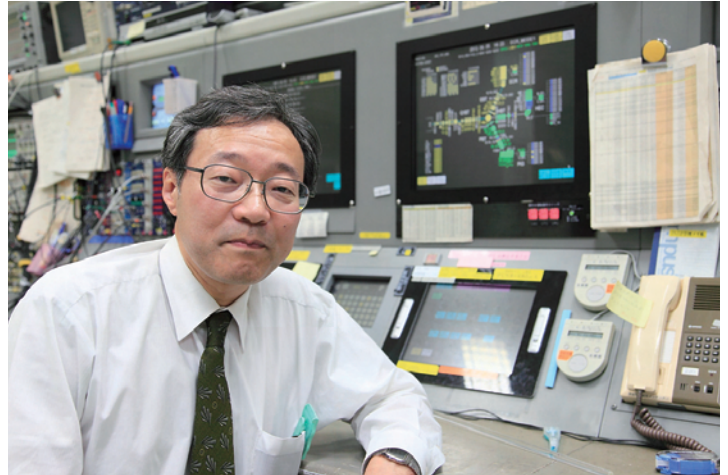
- [1] Tsujii H, Mizoe J, Kamada T, *et al.*: Clinical results of carbon ion radiotherapy at NIRS, *J Radiat Res*, 48, A1-A13, 2007.
- [2] Miyamoto T, Baba M, Yamamoto N, *et al.*: Curative treatment of Stage I non-small-cell lung cancer with carbon ion beams using a hypofractionated regimen, *Int J Radiat Oncol Biol Phys*, 67, 750-758, 2007.
- [3] Moritake T, Nakawatari M, Imai T, *et al.*: Strain-dependent Damage in Mouse Lung After Carbon Ion Irradiation, *Inter J Radiation Oncol Biol Phys*, 84, e95-e102, 2012.

Highlight

Promotion of carbon-ion radiotherapy facilities

Atsushi Kitagawa

E-mail: kitagawa@nirs.go.jp



The approval of “advanced medicine” at NIRS in 2003 has awakened an interest in carbon-ion radiotherapy all over Japan. In order to promote carbon-ion radiotherapy, development efforts for new downsizing technologies, personnel training systems, guidelines for treatment procedures, methods of radiological protection for medical workers and related persons, and so on have been carried out by the Japanese government and collaborating organizations. The most important project was the construction of the Gunma University Heavy Ion Medical Center (GHMC), and GHMC was launched in 2010. As a result, constructions of the 4th facility in Saga and the 5th facility in Kanagawa were promoted and started. The SAGA Heavy Ion Medical Accelerator in Tosu (SAGA-HIMAT) will start operation in 2013. Construction of the ion-beam Radiation Oncology Center in Kanagawa (i-ROCK) at Kanagawa Cancer Center also started in 2011. Table 1 lists heavy ion

radiotherapy facilities worldwide. Presently, there are six facilities in operation and seven are under construction. Five of the thirteen are located in Japan. The oldest (Bevalac) and third oldest (UNILAC+SIS) facilities are no longer in operation.

On the other hand, many issues for study have been increasingly recognized, i.e. continuing efforts for cost reduction, development of systematic patient selection procedures, development of specialists in related industrial fields, and so on. It is necessary

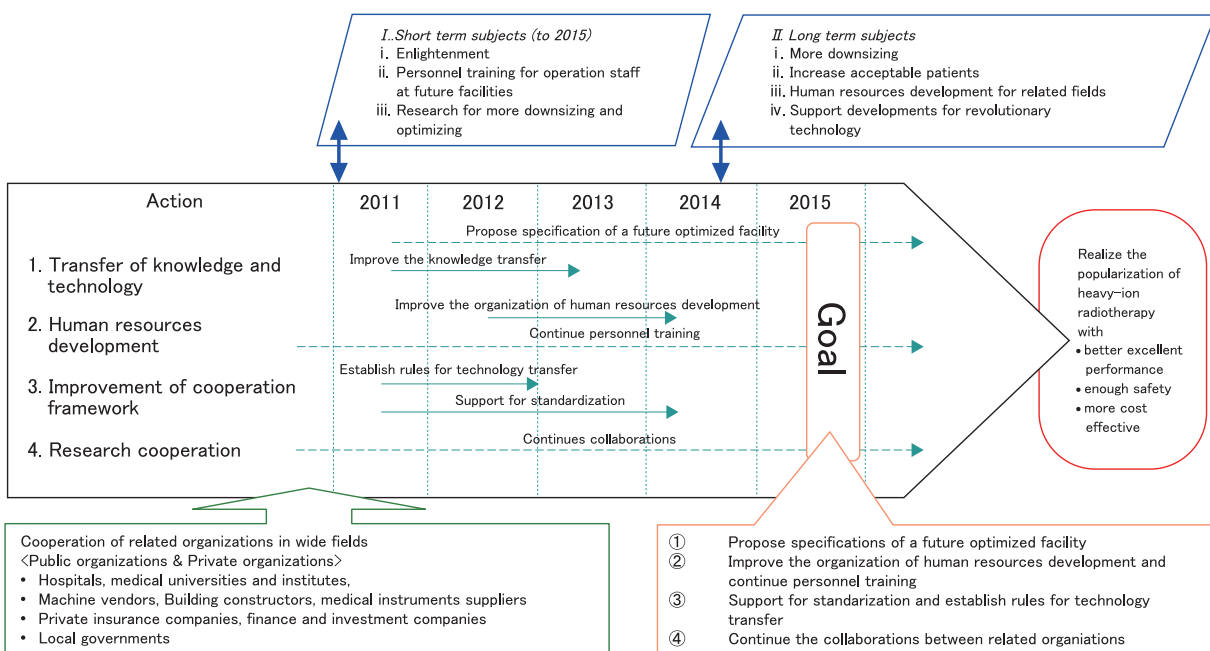


Fig.1 NIRS's roadmap for carbon-ion radiotherapy promotion in 2011-2015.

Table 1 Heavy ion radiotherapy facilities worldwide.

Institution	Facility acronym	Location (Country)	Start, close year	Total pati-ents	Number of treatment rooms and irradiation ports				Irradiation methods	Energy (MeV /u)/ Intensity	Ion species
					R	H	V	Other			
LBL	Bevalac	Berkeley (USA)	1975-1992	433	1	1	0	0	ST, W	670(Ne) 1E10ppp	Ne, Si, etc
NIRS	HIMAC	Chiba (Japan)	1994 -	6846 Jul.'12	6*	4	4	1* rotate	W, LS, RS	430/ 2E9pps	C
GSI	UNILAC+SIS	Darmstadt (Germany)	1997-2009	440	1	1	0	0	RS	430/ 4E10ppp	C
Hyogo ion beam medical center	HIBMC	Hyogo (Japan)	2002-	1393 Mar'12	3+	2	1	1 45deg	W	320/ 2E9pps	C, p
IMP	HIRFL-CSR	Lanzhou (China)	2009 -	159 Oct'11	2	2	0	0	W, LS	235/ 5E8ppp	C
Univ. Heidelberg	HIT	Heidelberg (Germany)	2009 -	900 May'12	3	2	0	1 rotate	RS	430/ 1E9ppp	C, p
Gunma Univ.	GHMC	Gunma (Japan)	2010 -	424 Dec'12	4*	2	3*	0	W, LS	400/ 1.2E9pps	C
Fondazione CNAO	CNAO	Pavia (Italy)	2012 -	-	3	3	1	0	RS	400/ 4.5E8ppp	C, p
Kyushu International heavy-ion Treatment Center	SAGA-HIMAT	Saga (Japan)	2013 (plan)	-	3*	3*	2*	1 45deg	W, LS, RS	400/ 1.2E9pps	C
Fudan Univ. Shanghai Cancer Center	SPHITH	Shanghai (China)	2013 (plan)	-	3	1	2	1	RS	430/ 3E8pps	C, p
EBG MedAustron Ltd.	Med-Austron	Wiener Neustadt (Austria)	2014 (plan)	-	3*	2*	1	0	RS	400/ 1E9pps	C, p, O
Gansu Tumor Hospital	HITFiL	Lanzhou (China)	2014 (plan)	-	4	2	2	1 45deg	W, SS	400/ 4E8pps	C
Wuwei Tumor Hospital	HITFiW	Wuwei (China)	2014 (plan)	-	4	2	2	1 45deg	W, SS	400/ 4E8pps	C
Kanagawa Cancer Center	i-ROCK	Kanagawa (Japan)	2015 (plan)	-	4	4	2	0	W, LS, RS	430/ 1.2E9pps	C
KIRAMS	KHIMA	Busan (Korea)	2015 (plan)	-							C

Treatment rooms: * includes those under construction and used in research, + excludes proton treatment rooms
 Irradiation method: ST (scatterer); W (wobbler); LS (layer stacking); RS (raster scanning); SS (spot scanning)
 Unit of intensity: ppp (particles per pulse); pps (particles per second)

to improve the framework of knowledge and technology transfer, to increase efforts in human resources development, to achieve worldwide standardization, and to cooperate on new research and development. A new roadmap for the next step of promotion by NIRS has been determined and is shown in Fig. 1.

In the present cooperation framework between NIRS and a partner, NIRS desires to give necessary support in construction procedures as summarized in Fig.2. In the planning phase, the partner is able to obtain the necessary clinical knowledge or technical recommendations. NIRS dispatches specialists to authorized committees for the partner. The necessary technical guidance or technology transfer will be arranged during the construction phase. For operation planning, the partner is also able to share clinical data such as protocols and clinical results. Recent hospital-specified facilities have set a goal of treating 800-1000 patients per year. Of course, it is not possible for only NIRS to solve all problems and to realize the goal. Cooperation among related public and private organizations in many fields is very important. International activities and collaborations are also required. It is expected that the role of cooperation frameworks between NIRS and such organizations will become more efficient.

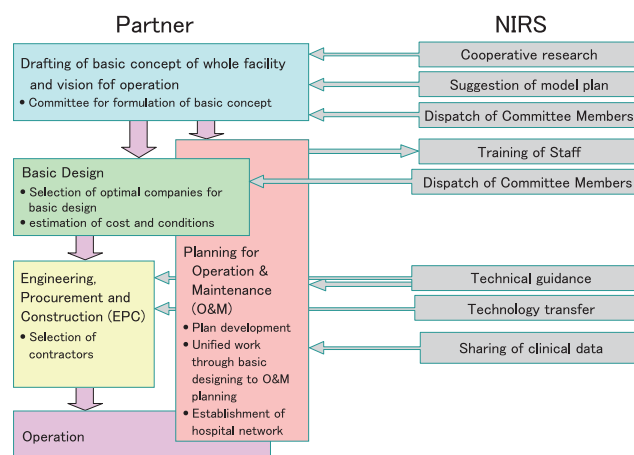


Fig.2 A typical cooperation procedure between NIRS and a partner

The Research Project with Heavy Ions at NIRS-HIMAC

Akifumi Fukumura

E-mail: fukumura@nirs.go.jp

Since 1994 the Heavy-Ion Medical Accelerator in Chiba (HIMAC) at NIRS has been opened to use by researchers worldwide in the field of ion-beam sciences other than carbon-beam radiotherapy. There are four experimental halls (Physics, Biology, Secondary beam and Medium-energy caves) as well as three treatment rooms. During the daytime from Tuesday through Friday, HIMAC is operated for patient treatments. At night and on weekends the four halls can be used for various experiments with ion beams. The latter framework is specified as "The Research Project with Heavy Ions at NIRS-HIMAC". Table 1 shows typical beam characteristics which are available at the Physics cave.

NIRS accepts proposal submissions for the Research Project twice a year (basically in June and November). Information about the call for proposals can be seen on the NIRS website^[1]. The Program Advisory Committee (PAC) for the Research Project reviews submitted proposals from the viewpoint of scientific merits and feasibilities. The Machine Time Committee allocates beam time in accordance with the review of PAC, considering requests from proposers. The Program Coordinator Group supports researchers especially from external institutions. The researchers, whose proposals employing HIMAC are accepted, are asked to make a report including a list of publications and to make a presentation at annual meeting after the end of the fiscal year (FY).



Fig.1 shows numbers of accepted proposals as a function of fiscal year. In FY 2011, 133 proposals from medicine, biology and physics etc. were accepted and total beam time of 5070 hours was supplied. Fig.2 shows contents of accepted proposals: physics pie chart (a) includes medical physics, accelerator, atom & nuclear physics, chemistry and space sciences; and biology pie chart (b) includes fundamental studies for cancer treatment, response of normal tissue, cell biology and molecular biology. More than 700 researchers, including 120 foreigners, were registered as participants from external institutions. Fig.3 shows numbers of scientific reports such as original papers, proceedings, theses and oral presentations. For more detail, the annual report^[2] of the Research Project (partly in English) is available from the Program Coordinator (book or CD-ROM) and at the NIRS website (PDF file). It includes submitted reports and publication lists.

Table 1 Typical beam characteristics available at HIMAC

Ion	Energy(MeV/u)								Intensity pps(partides/second)
He	100	180	230	—	—	—	—	—	$<1.2 \times 10^{10}$
C	100	180	230	290	350	400	430	—	$<1.8 \times 10^9$
N	100	180	230	290	350	400	430	—	$<1.5 \times 10^9$
O	100	180	230	290	350	400	430	—	$<1.1 \times 10^9$
Ne	100	180	230	290	350	400	600	—	$<7.8 \times 10^8$
Si	100	180	230	290	350	400	600	800	$<4.0 \times 10^8$
Ar	—	—	—	290	—	400	650	—	$<2.4 \times 10^8$
Fe	—	—	—	—	—	400	500	—	$<2.5 \times 10^8$

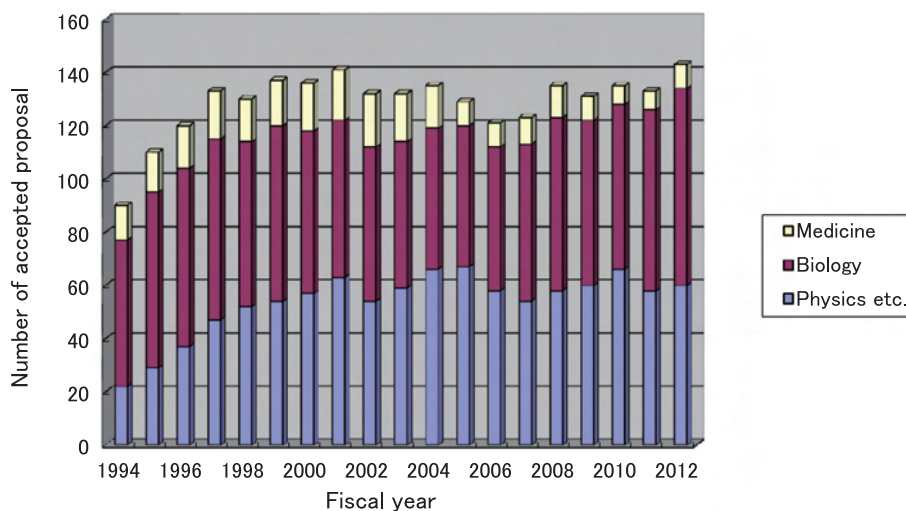
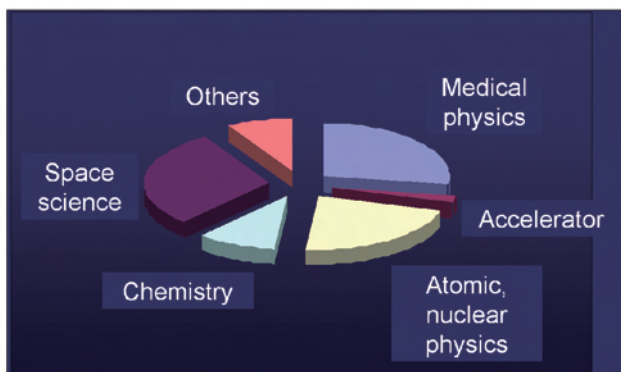


Fig.1 Numbers of accepted proposals as a function of fiscal years

a)



b)

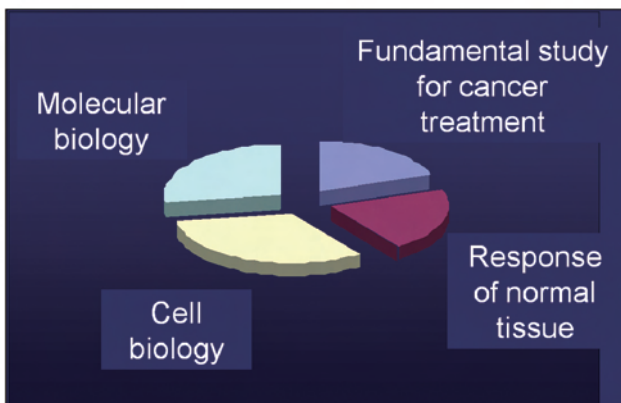


Fig.2 Contents of accepted proposals in physics (a) and biology (b) in FY 2011

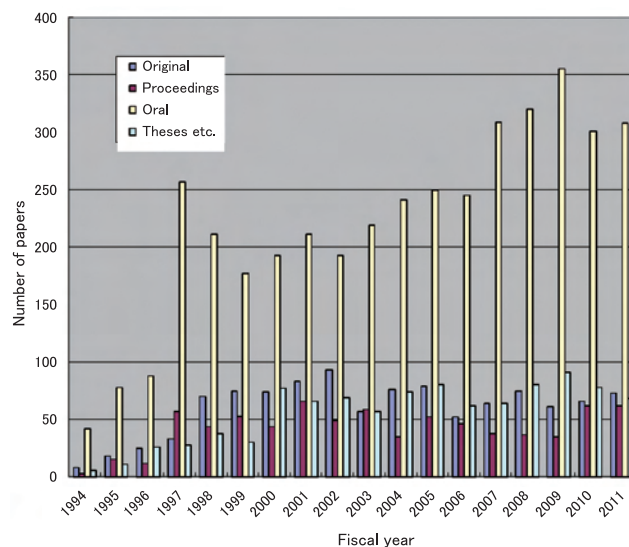


Fig.3 Number of scientific reports as a function of fiscal year

References

- [1] NIRS, <http://www.nirs.go.jp/information/application/25himac2013.shtml>
- [2] NIRS, 2011 Annual Report of the Research Project with Heavy Ions at NIRS-HIMAC, NIRS-M-251, Aug. 2012. <http://www.nirs.go.jp/publication/irregular/04.shtml>

Molecular Imaging Research for Functional Diagnosis

Yasuhisa Fujibayashi, Ph.D., D.Med.Sci.

Director of Molecular Imaging Center

E-mail: yfuji@nirs.go.jp

The Molecular Imaging Center (MIC) is the youngest research center at NIRS, established in 2006 for research and development on clinical applications of radiation, especially in the field of nuclear medicine, including positron emission tomography (PET), single photon emission tomography (SPECT) and internal radiation therapy. Research on these is based on collaboration among diverse areas as follows:

- (1) Drug design for target-selective delivery (molecular probe), labeling of the molecular probe with suitable radionuclide for diagnosis/therapy, and radionuclide production.
- (2) Development of three-dimensional gamma-ray measurement systems such as PET and SPECT, including hardware and software.
- (3) Clinical application for diagnosis/therapy of tumors, psychiatric and neurodegenerative disorders, and so on.

The MIC has four research groups: the Molecular Probe Program, the Biophysics Program, the Diagnostic Imaging Program, and the Molecular Neuroimaging Program.

The MIC also promotes research on magnetic resonance imaging (MRI), X-ray-CT imaging, and optical imaging; these radiological imaging techniques are an integral part of diagnostic imaging in nuclear medicine. The development of PET-CT has realized fusion images of anatomy and functionality that have resulted in a synergic progress in diagnostic imaging. Recently, PET-MR has become commercially available, and it will surely bring unexpected advances in the clinical field.

Molecular Probe Program

1) Radiolabeling technique

We developed a method for preparing 2-[¹¹C]methoxy pyridine using [¹¹C]methyl triflate as a radiolabeling agent. Using this method, we synthesized a novel PET probe with a reliable and high radiochemical yield and it is expected to be put to routine clinical use. We carried out a joint research project with a pharmaceutical company to develop PET probes for brain neurotransmitters and found a promising candidate which was synthesized using [¹¹C]cyanide as a labeling agent.

A convenient route was determined for producing [¹¹C]formaldehyde with a reproducible radiochemical yield and sufficient



amount of radioactivity for labeling. Using [¹¹C]formaldehyde, we developed a novel technique for radiosynthesis of [¹¹C]oligopeptide. On the other hand, a labeling method directly using cyclotron-produced [¹⁸F]KF aqueous solution was established for synthesizing new [¹⁸F]peptide PET probes for tumor imaging.

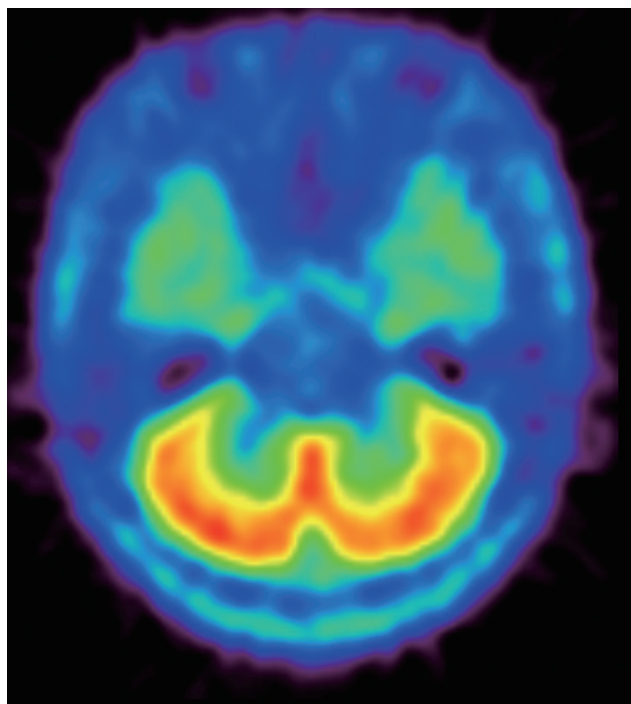


Fig.1 PET study of [¹¹C]ITMM for human brain

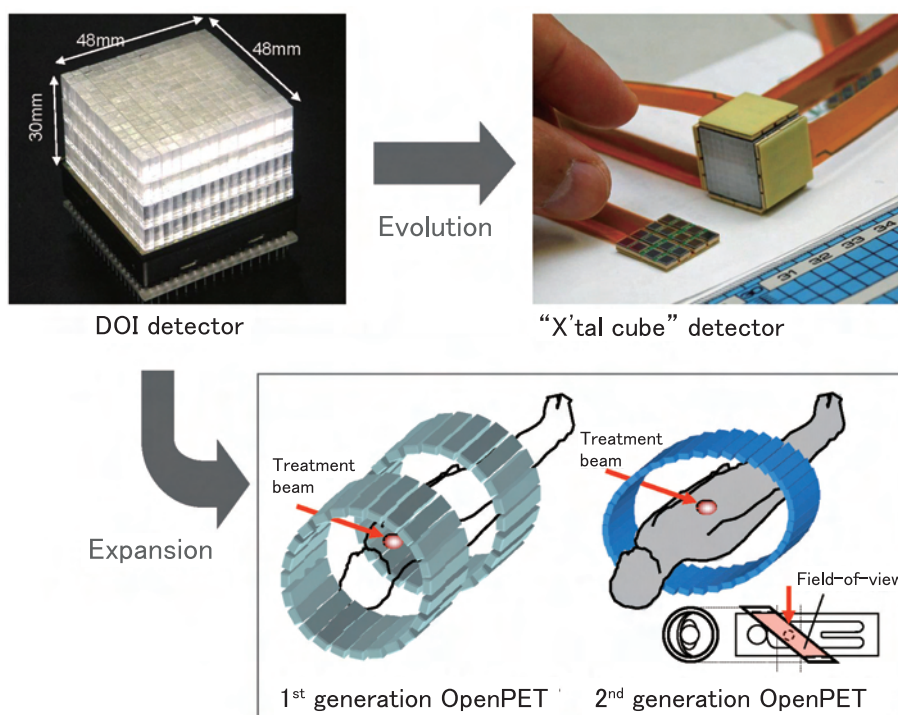


Fig.2 Development of next generation PET technologies

2) Development of novel PET probes

We designed and labeled novel analogs of hippuric acid for PET imaging of organic anion transporters. After labeling the analogs by [^{11}C]acylation or [^{11}C]methylation, the radioactive products were successfully obtained. Preliminary evaluation showed that one candidate product had promising properties as an in vivo PET probe and was worth further evaluation. This probe had potentials for measuring the functional activity of organic anion transporters in brain and multi-drug resistance protein 4 in heart. In addition, we demonstrated that an [^{11}C]amino acid agent [^{11}C]AIB is useful for imaging the function of the blood-brain-barrier in inflammatory and glioma animal models.

Using PET with [^{18}F]FEDAC, a radioligand for translocator protein (18 KDa), we successfully visualized lung inflammation and non-alcoholic fatty liver disease. On the other hand, dozens of PET candidates for metabotropic glutamate 1 receptor were designed and screened. Three promising probes showing high specific binding in brain were selected for an in vivo imaging study in primate brain and its periphery. Of these PET probes, [^{11}C]ITMM is undergoing clinical study for the imaging and quantitative analysis of metabotropic glutamate 1 receptor in human brain (Fig.1).

3) Production of SPECT, non-standard PET and alpha-emitting radionuclides

A basic study for the production method of $^{99\text{m}}\text{Tc}$, an important radionuclide in nuclear medicine, by proton-induced nuclear reactions was carried out. Several $^{99\text{m}}\text{Tc}$ -labeled radiopharmaceuticals were synthesized and analyzed successfully.

A system producing ^{89}Zr was developed and the efficient production procedures including extraction from the cyclotron target and purification were determined. Sufficient radioactivity of ^{89}Zr was produced for radiolabeling and an evaluation study on animals was made. In addition to the positron-emitting isotopes, we furthermore developed a remotely controlled system for produc-

ing ^{211}At as a useful short-lived alpha-emitting isotope for medical applications.

4) Production of useful PET probes for clinical application

For the past two years, we have improved and optimized the procedures of operation and quality control, and achieved standardization of many PET probes which are routinely produced in NIRS for human use. In addition, we prepared many kinds of documents for validation of the regular production and quality control methods for safe administration into human subjects, and for evaluation of the toxicity and radiation dosimetry of PET probe for clinical applications. Three new PET probes were approved by the IRB for clinical research in last fiscal year.

5) Contribution to quality control of clinical PET within Japan

We performed quantitative analysis and provides certificates for chemical impurities in [^{18}F]FDG and other radiopharmaceutical preparations which were produced in other PET facilities in Japan.

Biophysics Program

The Biophysics Program aims at development of next generation PET technologies and of methods for quantitative analyses of in vivo imaging. PET plays important roles in clinical diagnosis and molecular imaging research, but there are several potential points for which big improvements could be made including resolution, sensitivity and cost. Quantitative analyses of PET data are also important to measure physiological functions.

1) Next generation PET technologies

The Imaging Physics Team carries out basic studies on instrumentation, image reconstruction (Fig.2) and data corrections to improve image quality and quantity in nuclear medicine. A depth-of-interaction (DOI) detector will be a key device to get any significant improvement in sensitivity while maintaining high spatial

resolution. DOI measurement also has a potential to expand application of PET to new fields because it allows for more flexible detector arrangement. As an example, we are developing the world's first, open-type PET geometry OpenPET, which is expected to lead to PET imaging during treatment. We have developed a small prototype to show a proof-of-concept of OpenPET imaging. The DOI detector itself continues to evolve with the help of recently developed semiconductor photodetectors, often referred to as silicon photomultipliers (SiPMs). We are developing a SiPM-based DOI detector named X'tal cube to achieve sub-mm spatial resolution, which is reaching the theoretical limitation of PET imaging. We have developed a prototype for 1mm isotropic detector resolution, which equals the world record.

2) Quantitative analyses of in vivo imaging

The Imaging Physiology Team develops methods for quantitative analyses of in vivo imaging obtained from PET imaging, MRI, and optical imaging. In PET receptor imaging, a new graphic plot analysis was evaluated for a reliable quantification of binding potential, and it was shown that this could provide unbiased binding potentials. In MR diffusion-tensor imaging, an oscillating-gradient spin-echo sequence to diffusion-tensor imaging was applied to in vivo rat brain, and pixel-wise linear fits to the mean diffusivity found elevated changes across the cerebellum. Using laser-Doppler flowmetry, we found that the increase in red blood cell velocity during sensory stimulation was much larger than that of concentration in awake mice, supporting the PET measurement of CBF and CBV during neural activation in humans. An analytical method to quantitatively measure vessel diameters and flow dynamics was developed for fluorescent confocal microscopic imaging, and this method revealed that cortical surface vascular tone and parenchymal blood flow were coordinated in rat brain. In two-photon laser scanning fluorescence microscopy, the redistributed parenchymal microcirculation among the capillary networks induced by brain activation was demonstrated with gene manipulated rats in which red blood cells express green-fluorescent proteins.

Diagnostic Imaging Program

1) Basic clinical research on pathophysiological imaging with molecular imaging

We have conducted clinical PET research using ^{18}F -fluorothymidine, a marker of cellular proliferation, in lung cancer and malignant melanoma patients receiving carbon-ion radiotherapy and proved its role as a prognostic indicator. As a model of carcinogenesis, we have established a facilitated model of radiation-induced thymic lymphoma in mice and are applying various molecular imaging methods for imaging the process of lymphoma development. We have developed an efficient production method of an amino acid PET probe, ^{11}C -AIB, and proved that ^{11}C -AIB has a potential in differentiating cancer from inflammation (Fig.3). For the biological characterization of cancers that are refractory to treatment, we are focusing on tumor hypoxia, and clinical PET research using a hypoxia PET probe, ^{18}F -FAZA, is ongoing with regard to its ability to predict the responsiveness to treatment and prognosis, along with basic preclinical research for the biological characterization of intra-tumoral areas showing high accumulation of hypoxia PET probes.

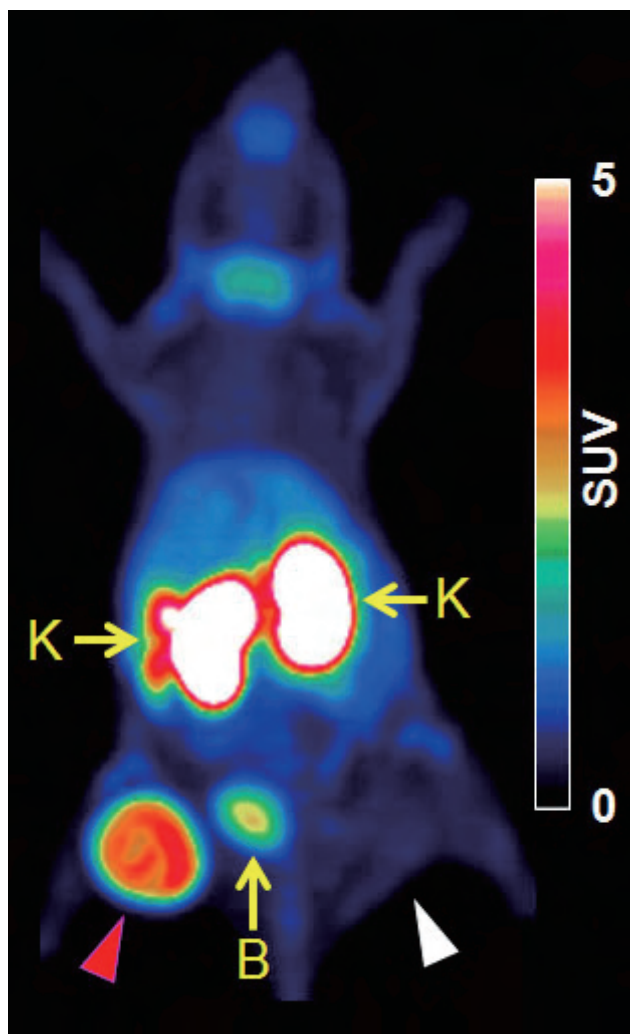


Fig.3 ^{11}C -AIB PET of a mice having subcutaneous tumor xenograft (red arrowhead) and inflammation (white arrowhead). ^{11}C -AIB is highly accumulated in the tumor, while uptake in inflammatory lesion is negligible. K: kidney, B: urinary bladder

2) Development of antibody and peptide probes for the targeted imaging of various cancer-related molecules

In research on the imaging of cancer molecular targets, we have developed antibody probes targeting pancreatic cancer-related molecules and successfully carried out PET imaging of subcutaneously and orthotopically transplanted pancreatic cancer in mice by using ^{89}Zr -labeled human monoclonal antibody recognizing transferrin receptor. We have also developed a PET probe to visualize cancer angiogenesis, a tetramer of cRGD peptide labeled with ^{64}Cu , targeting integrin $\alpha_v\beta_3$ expressed on activated endothelial cells, and proved that this probe could image cancer angiogenesis and also could evaluate the effect of anti-angiogenesis therapy (see Highlight for detail).

3) Development of MRI-based functional probes and nano-sized multi-functional probes and their application in various disease models

In research on the application of MRI-based functional probes, we have shown that the change in cellular uptake of manganese (Mn) after irradiation in Mn-enhanced MRI was related to radiation-induced alteration in the cell cycle. We have also developed an MRI probe to measure tissue redox status and applied it to

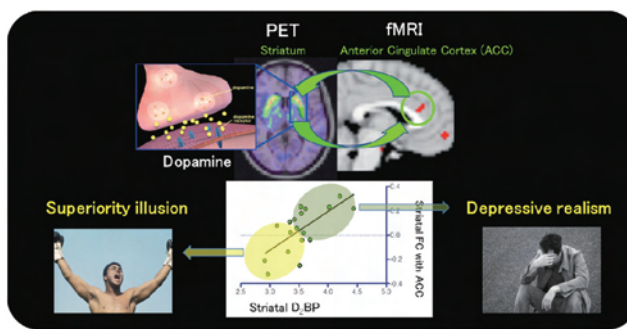


Fig.4 Relationship between symptom-related cognitive bias and dopamine neurotransmission

Assuming an inverse relationship between D2 receptor availability and presynaptic dopamine release, dopamine likely acts on striatal D2 receptors to suppress functional connectivity (FC) between striatum and ACC. This connectivity predicts individual differences in the superiority illusion.

healthy and cancer-bearing mice for depiction of the changes in tissue redox status according to the disease condition (see Highlight for detail). We have developed and improved a nano-sized drug-delivery system (nano-DDS) using liposomes coated with thermo-sensitive polymer containing anti-cancer agent, fluorescent dye and MRI contrast agent, and succeeded in getting efficient drug release by local heating that could be imaged by MRI; we also proved the treatment effect after combined nano-DDS, local heating and irradiation.

Molecular Neuroimaging Program

There are three major research targets of the Molecular Neuroimaging Program: the development and evaluation of imaging biomarkers of several types of dementia in the key process of their pathophysiology; the investigation of molecular mechanisms of the symptoms related to regional brain functions using both clinical data and model animal experiments; and, the development of surrogate imaging markers for evaluation of treatment of neuropsychiatric disorders.

1) Imaging biomarker of dementia

In the field of development and evaluation of imaging biomarkers of several types of dementia, we have found serotonin 1A receptor change in tau transgenic mice, metabotropic glutamate receptor change in amyloid precursor protein transgenic mice, and translocator protein (TSPO) change in mild cognitive impairment (MCI) patients. Those neurotransmission changes in model mice indicated that a possible target for the treatment of dementia and the TSPO change in MCI patients might indicate a possible involvement of an inflammation process even in early stage of dementia. The most important result in this field is the development of a tau imaging probe. We have successfully evaluated it in Alzheimer's disease (AD) brain; the accumulation of our tau probe was negligible in healthy control brain but significant accumulation was observed in the hippocampal region of AD brain where the accumulation of [¹¹C]PIB was relatively low compared to other cortical regions. Furthermore, our preliminary data suggested that our tau probe may be capable of capturing the temporospatial spreading of neurofibrillary tau pathologies from the transentorhinal cortex to other limbic and neocortical association areas with the progression of AD.

2) Molecular mechanism of regional brain functions

Regarding the mechanisms of human behavior, which has long been investigated by various disciplines including philosophy, psychology, economics, and biology, we have used functional MRI (fMRI) to investigate regional brain function mechanisms and PET to investigate molecular mechanisms. We provide unique neurobiological evidence to account for individual differences of reaction to unfairness; higher central serotonin transmission might allow humans to behave adroitly and opportunistically, being good at playing games while pursuing self-interest. We also elucidated neural circuits for mitigating criminal sentences. Individual differences on the inclination to mitigate, the sentence reduction per unit of judged sympathy, correlated with activity in the right middle insula, an area known to represent interception of visceral states. These results could help the legal system understand how potential jurors actually reach a decision and they could contribute to the growing body of knowledge about whether emotion and cognition are integrated sensibly in difficult judgments. Combining both fMRI and PET, we found an interrelationship between dopamine neurotransmission and fronto-striatal resting-state functional connectivity in the basis for cognitive bias such as a "superiority illusion". To clarify the direct molecular and physiological mechanisms of emotion and behavior, experiments with an animal model are quite important. Using a monkey model of hypothyroidism, which is associated with symptoms of low motivation characterized by instrumental task performance, we found the performance of goal-directed action was affected by dopaminergic manipulations. PET revealed that there was a change in dopamine D2 receptor in the ventromedial prefrontal cortex of the model monkey. The combination of different imaging techniques is essential in modern neuroscience to unite cognitive neuroscience and neuropsychopharmacology.

3) Surrogate imaging markers in therapy

In neuropsychopharmacology, various target molecules and the kinetics of drugs targeting them can be visualized using PET. We have examined dopamine receptor occupancy of antipsychotics and serotonin transporter occupancy of antidepressants. Another important target of antidepressants is norepinephrine transporter (NET). We have measured NET occupancy of 75-200 mg/day of nortriptyline and found approximately 50-70% occupancies in the living human brain.

Highlight

Synthesis and evaluation of [^{11}C]ITMM for positron emission tomography imaging of metabotropic glutamate receptor subtype 1 in rodent brain

Masayuki Fujinaga

E-mail: fujinaga@nirs.go.jp

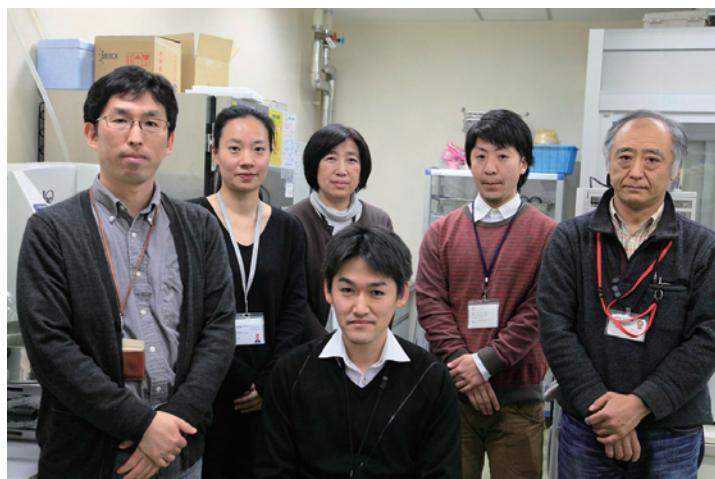
Objectives

Glutamate is an excitatory neurotransmitter in the central nervous system (CNS) and plays a role in neurotransmission via activation of its receptors e.g. ionotropic and metabotropic (mGlu) types. mGlu receptors are classified into three groups including eight subtypes according to sequence homology, coupling mechanisms to G-protein, and pharmacological activity. Group I of the mGlu receptors (mGlu1 and mGlu5) plays important physiological roles in regulating ion channels and synaptic transmission, and in synaptic plasticity, which underlies memory and learning. It has been reported that mGlu1 may be a drug target for the treatment of diseases such as stroke, epilepsy, pain, cerebellar ataxia, Parkinson's disease, anxiety, and mood disorders. To elucidate the role of mGlu1 for these diseases, many PET ligands have been developed for mGlu1^[1]. Recently, we developed [^{18}F]FITM as a novel PET ligand for imaging mGlu1 in the brain. To find a PET ligand with more favorable in vivo behavior, we designed various candidates using [^{18}F]FITM as a lead compound. In this report, we summarize our published findings^[2] on synthesis and evaluation of [^{11}C]ITMM and its [^{18}F]fluoroalkylated derivatives as new PET ligands for mGlu1 in the brain.

Overview

First, as shown in Fig.1A, the novel compounds ITMM and fluoroalkylated derivatives 2 and 3 were synthesized at 5-7 steps from 4,6-dichloropyrimidine. [^{11}C]ITMM was prepared by reaction of desmethyl precursor 1 with [^{11}C]CH₃I of two levels of specific activity (37-185 GBq/ μmol and 3700-7400 GBq/ μmol) at 70°C for 5 min in the presence of NaOH (Fig.1B). Two [^{18}F]fluoroalkoxy ligands [^{18}F]2 and [^{18}F]3 were synthesized by reaction of 1 with [^{18}F]FCH₂CH₂Br and [^{18}F]FCH₂CH₂CH₂Br, respectively, at 90°C or 120°C for 10 min.

In vitro binding affinities of ITMM, 2, and 3 for mGlu1 were measured from competition against the binding of mGlu1-selective [^{18}F]FITM using rat brain homogenates. Among these ligands, ITMM showed the highest binding affinity ($K_i = 12.6 \text{ nM}$) for mGlu1. On the other hand, fluoropropyl 3 displayed the lowest affinity ($K_i > 5 \mu\text{M}$). This result suggested that the bulk-increasing group attached to the 4-position of the benzene ring may not fit the binding site on the mGlu1 domain.



The lipophilicities (Log D) for [^{11}C]ITMM, [^{18}F]2, and [^{18}F]3 were 2.57-2.80 measured by the shake flask method and their values were found in the range normally considered favorable for PET.

In vitro autoradiography with [^{11}C]ITMM, [^{18}F]2, and [^{18}F]3, as for [^{11}C]ITMM, the distribution pattern of radioactivity was heterogeneous, with the highest level in the cerebellum. Moderate radioactivity was seen in the thalamus and a low level was seen in the striatum. This result was consistent with the distribution pattern of mGlu1 in the rat brain. Co-incubation with mGlu1-selective JNJ-16259685 reduced radioactivity in the sections to 30% of the ra-

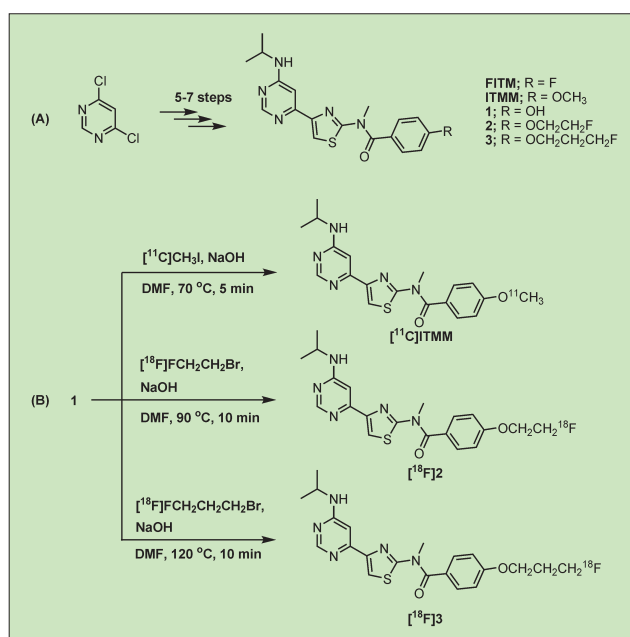


Fig.1 Chemical synthesis and radiosynthesis.

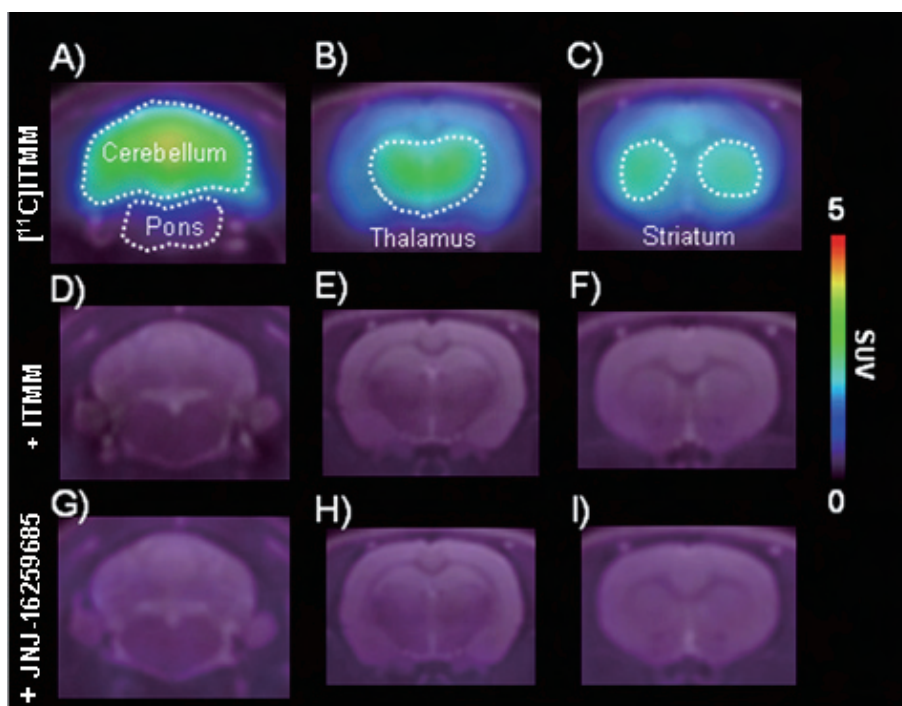


Fig. 2 PET images (A-I) were generated by summing the whole scan (0-90 min). (A-C) [^{11}C]ITMM only; (D-F) [^{11}C]ITMM after treatment with ITMM; (G-I) [^{11}C]ITMM after treatment with JNJ-16259685.

radioactivity in control sections. Thus, we found that [^{11}C]ITMM showed high specificity for mGlu1 *in vitro*. In the case of [^{18}F]2 and [^{18}F]3, both showed much lower radioactivity in the brain than [^{11}C]ITMM did. Moreover, co-incubation with JNJ-16259685 did not affect radioactivity in the brain. Therefore, we selected only [^{11}C]ITMM for *in vivo* evaluation.

The *in vivo* uptake, kinetics, and specific binding in the rat brains were examined using small-animal PET with [^{11}C]ITMM of 95-140 GBq/ μmol . [^{11}C]ITMM showed high brain penetration and accumulation of radioactivity in the brain regions as shown in Fig. 2. The highest uptake was seen in the cerebellum, followed by the thalamus, and striatum. The lowest radioactivity was determined in the pons. This distribution pattern of uptake reflected the distribution of mGlu1 in the brain^[3], which was similar to that *in vitro* autoradiograms for [^{11}C]ITMM. Regarding the kinetics, radioactivity in the cerebellum gradually increased after injection, peaked at 45 min, and decreased to 90% of the maximum at 90 min. Radioactivity in the thalamus and striatum peaked also at 45 min and declined slowly until the end of the PET scan. Pretreatment with unlabeled ITMM or JNJ-16259685 markedly reduced the uptake compared to the control.

Furthermore, PET scanning with [^{11}C]ITMM was performed in

mGlu1 knockout mice to confirm the specificity of [^{11}C]ITMM for mGlu1. In the wild-type mouse, accumulation of radioactivity was seen in the cerebellum and thalamus, which was similar to the accumulation seen in PET images of rat brains. On the other hand, in the mGlu1-knockout mouse, only a very low radioactivity was determined in the brain. The present results indicate that [^{11}C]ITMM is a promising PET ligand for mGlu1. Currently, [^{11}C]ITMM as the first useful PET ligand for mGlu1 is undergoing clinical trials in the human brain.

References

- [1] Fujinaga M, Maeda J, Yui J, *et al.*: Characterization of 1-(2-[^{18}F]fluoro-3-pyridyl)-4-(2-isopropyl-1-oxo-isoindoline-5-yl)-5-methyl-1H-1,2,3-triazole, a PET ligand for imaging the metabotropic glutamate receptor type 1 in rat and monkey brains. *J Neurochem*, 121, 115-124, 2012.
- [2] Fujinaga M, Yamasaki T, Yui J, *et al.*: Synthesis and Evaluation of Novel Radioligands for Positron Emission Tomography Imaging of Metabotropic Glutamate Receptor Subtype 1 (mGluR1) in Rodent Brain. *J Med Chem*, 55, 2342-2352, 2012.
- [3] Yamasaki T, Fujinaga M, Kawamura K, *et al.*: *In vivo* Measurement of the Affinity and Density of Metabotropic Glutamate Receptor Subtype 1 in Rat Brain Using ^{18}F -FITM in Small-Animal PET. *J Nucl Med*, 53, 1601-1607, 2012.

Highlight

Development of a ceramic target vessel with potentially wide applicability for remote production of metallic radionuclides

Kotaro Nagatsu

E-mail: nagatsu@nirs.go.jp

Objectives

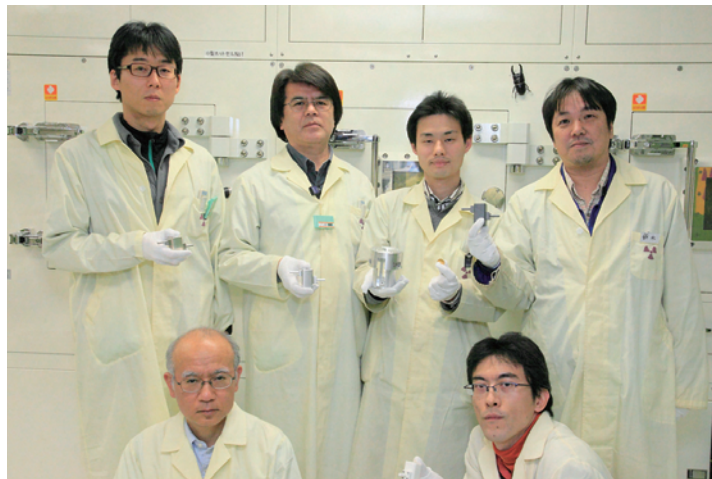
Metallic radionuclides play a prominent role in both diagnostic nuclear medicine and internal radiotherapy. While we, as the Radiopharmaceutical Production Team, have been providing many kinds of high quality metallic radionuclides routinely, we are also developing novel, cost-effective, and automated production methods for these radionuclides. To accommodate both routine production and research under the condition of limited beam time, easy operability with less effort and time or a least-waste production method is highly desirable.

Therefore, our research goal is not only achievement of products at high yield and with high quality, but also satisfying practical engineering needs; namely promoting efficiency of the production process from preparation to final purification and establishing remote production methods with less or no radiation exposure at low cost.

Overview

In the production of metallic radionuclides, using a conventional cyclotron or an irradiation system with a horizontal beam line is a laborious process and it takes a relatively long time to prepare the solid target, if secured metal foils or plates are unavailable commercially. One of the objectives in this research is to reduce the number of such time-consuming processes by applying a vertical irradiation system that produces radionuclides by using a downward transported beam^[1]. A target material, which is the source for the intended radionuclide, can be held in place easily by gravity with this system. This irradiation mechanism provides the great benefit of being able to use almost any form of chemical substance as the target material. Namely, non-self-supported materials, such as metal powders, granules, low melting point substances, or salts can be placed at the beam trajectory without the need for a prior solidification process. Thus, the time for target preparation is greatly reduced.

Remote handling of the highly radioactive material is another issue to be resolved. Briefly, the irradiated target should be removed remotely from the beam port, and then the target will be transferred to a hot cell for further processing. A versatile industrial robot, custom made remote-arms, or transporting cart on rails



is usually employed in conventional remote production systems. The purification process is then carried out by the following steps: i) disassembling the target vessel to take out the target material; ii) dissolving the irradiated target by strong acids; iii) isolating and purifying the intended radionuclide from other nuclides, especially those in the target material and impurities. These steps are also carried out remotely by using a manipulator or specialized device to reduce radiation exposure. As mentioned above, the handling of an "immobile" solid target, which is a counterpart of the "mobile" gaseous and liquid target, would need hand- or foot-like external driving forces. However, such devices are large-scale heavy systems that generally increase installation and maintenance costs, and occupy a sizable working place; therefore only a few facilities are able to accommodate them.

In this research, we demonstrated a simple and cost-effective remote production method by introducing strong acids into the target vessel to obtain the radio-metal solution in situ^[2]. The intended nuclide in liquid form should be easily transferable to the hot cell through a tube by applying appropriate pressure without using any huge robotic devices. However, conventional materials used for target vessels are metals, such as Al, Ti, or stainless steel, which are less durability against acids. Therefore, we designed new target vessels made of ceramics, namely alumina (Al_2O_3) or silicon carbide (SiC), to demonstrate the concept of in situ target dissolution (Fig. 1). Fortunately, both ceramics have favorable properties, such as excellent chemical resistance, fair thermal conductivity, and they are not molten in a practical temperature range, which are essential requirements for the target vessel materials.

We evaluated the feasibility of the ceramic target vessels with the vertical irradiation system for production of zirconium-89. ^{89}Zr is one of the most promising positron emitters applicable to

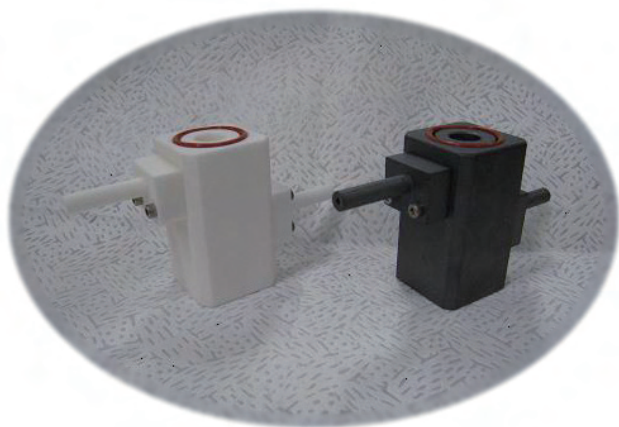


Fig.1 Ceramic target vessels made of high purity alumina (Al_2O_3 ; left) and silicon carbide (SiC; right).

immuno-PET studies due to its relatively long half life of 78 h, and it can be produced by a relatively low beam energy from yttrium-89 via the $^{89}\text{Y}(p,n)^{89}\text{Zr}$ nuclear reaction. Fortunately, the natural isotopic abundance of ^{89}Y is 100%; this makes it favorable for studies at modest cost, and the result can be obtained at high accuracy with less waste. Briefly, instead of secured Y foils, ^{89}Y powder prepared in the ceramic target vessel was employed as the target material. Under this condition, we evaluated the following items:

- 1) irradiation of a powder target while keeping the product yield at a sufficient level;
- 2) dissolution of the irradiated target remotely in the ceramic vessel by introducing an acid solution;
- 3) transfer of the radioactive solution to the hot cell through a tube automatically; and
- 4) capability to repeat the production while keeping the system integrity.

An automated apparatus for the purification of ^{89}Zr was also developed in this study (Fig.2). This apparatus design put emphasis on the production of highly concentrated ^{89}Zr by including reagent reservoirs and an ion-exchange column to purify the ^{89}Zr efficiently. All separation steps including the target-dissolving step were carried out remotely and automatically via a PC-based controller.

The integrity of the ceramic target vessel was kept while repeating the remote productions more than 10 times. The yield of ^{89}Zr with >99.9% radionuclide purity obtained by this method was about 90% of the expected value calculated from a previous report about the excitation function^[3]. The processing time for each production run was typically within 2.5 h. The product ^{89}Zr of 925 MBq in 90 μL of oxalic acid, obtained by 10 μA x 2 h irradiation, was successfully provided to immuno-PET studies. The irradiation of the powder target gave a successful result, and it was confirmed some of the laborious target preparation processes could be eliminated. Therefore, all of the objectives in this research were fully achieved.

Conclusion

Although we used Y powder as a target material in this pilot study, the production scheme is, in principle, applicable to other metal targets including isotopically enriched materials. Furthermore, the recovery process from the target vessel was similar to

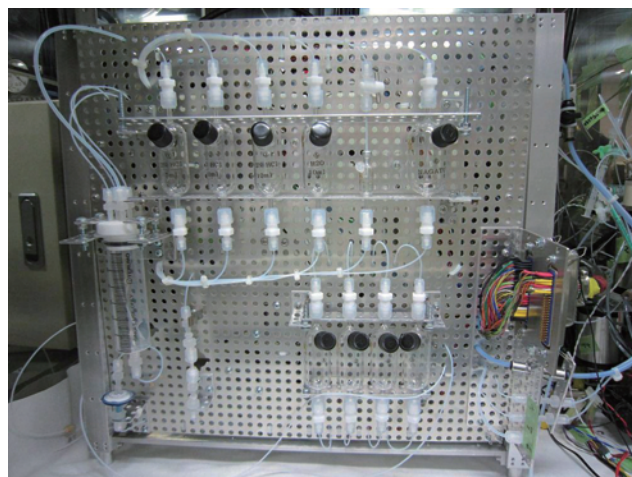


Fig.2 ^{89}Zr automated purification apparatus.

that of gaseous and liquid target production using the ceramic vessel. This means that the remote production of metallic radionuclides becomes accessible to many facilities with less effort and at lower cost.

Indeed, we have started to produce other metallic radionuclides by a modified method based on this result, and we strongly believe that novel production methods for medically important radionuclides will be shown in the near future.

Further expectations

The vertical irradiation technique is currently recognized as a specialized one because most cyclotrons or beam lines are designed to provide horizontal beams. However, we believe that a medical compact cyclotron with upright dee plates has inherent potential to deliver downward beams with minimal reconfiguration. By remodeling the magnetic fields and/or the position of the electron stripper, a downward or vertical beam can be obtained without using a huge bending magnet or extensive modification.

In the future, the development and distribution of cyclotrons equipped with vertical beam ports, used in combination with the ceramic target vessel developed here, are expected to make production of metallic radionuclides and associated applications more convenient and popular.

References

- [1] Nagatsu K, Fukada M, Minegishi K, *et al.*: Fully automated production of iodine-124 using a vertical beam, *Appl Radiat Isot*, 69, 146-157, 2011.
- [2] Nagatsu K, Suzuki H, Fukada M, *et al.*: An alumina ceramic target vessel for the remote production of metallic radionuclides by in situ target dissolution, *Nucl Med Biol*, 39, 1281-1285, 2012.
- [3] Steyn GF, Vermeulen C, Szelecsenyi F, *et al.*: Excitation functions of proton induced reactions on ^{89}Y and ^{93}Nb with emphasis on the production of selected radio-zirconiums, *J Korean Phys Soc*, 59, 1991-1994, 2011.

Highlight

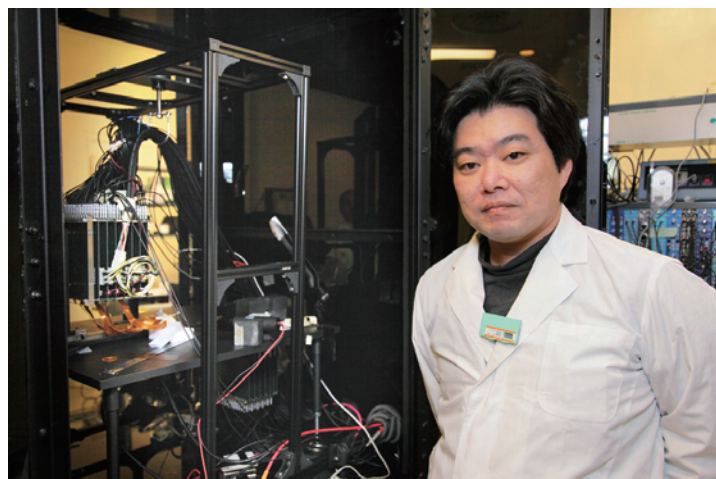
Impact of the laser-processed X'tal cube detector with 1 mm isotropic resolution in PET imaging

Eiji Yoshida

E-mail: rush@nirs.go.jp

We developed a novel, general purpose isotropic-3D PET detector X'tal cube which has high spatial resolution in all three dimensions. The research challenge for this detector was implementing effective detection of scintillation photons by covering six faces of a segmented crystal block with photo-detectors. Also, in order to fabricate the 3D crystal block efficiently and precisely, we applied a laser-processing technique to a monolithic crystal block instead of gluing segmented small crystals. Using the fabricated X'tal cubes, we evaluated its imaging resolution performance to show a proof-of-concept of isotropic resolution.

Typical PET detectors are designed with a 2D array of segmented scintillator crystals that are coupled to photomultiplier tubes on one side. However the parallax error caused by the thickness of the crystals degrades spatial resolution at the peripheral regions of the field-of-view (FOV). Therefore, depth-of-interaction (DOI) measurement is essential to achieve high spatial resolution. The X'tal cube^[1,2] is our original PET detector, which is being developed to achieve isotropic 3D positioning detectability.



The X'tal cube is based on a 3D segmented crystal block for which all surfaces are covered with photo-detectors (Fig.1 (a)). Instead of our initial approach of gluing segmented pieces of crystals, we successfully constructed a crystal block segmented by laser processing^[3], and we developed the first prototype of X'tal cube with the laser-processed 3D square grids of 2 mm length. Also, we extended the laser processing to 3D square grids of 1 mm length (Fig.1 (b)). The volume of a 1-mm crystal segment is 1/8 of that of a 2-mm crystal segment. We also evaluated imaging resolution performance with a newly developed one-pair prototype system to simulate a ring-type scanner. The one-pair prototype system consisted of two X'tal cubes, two rotating stages, and

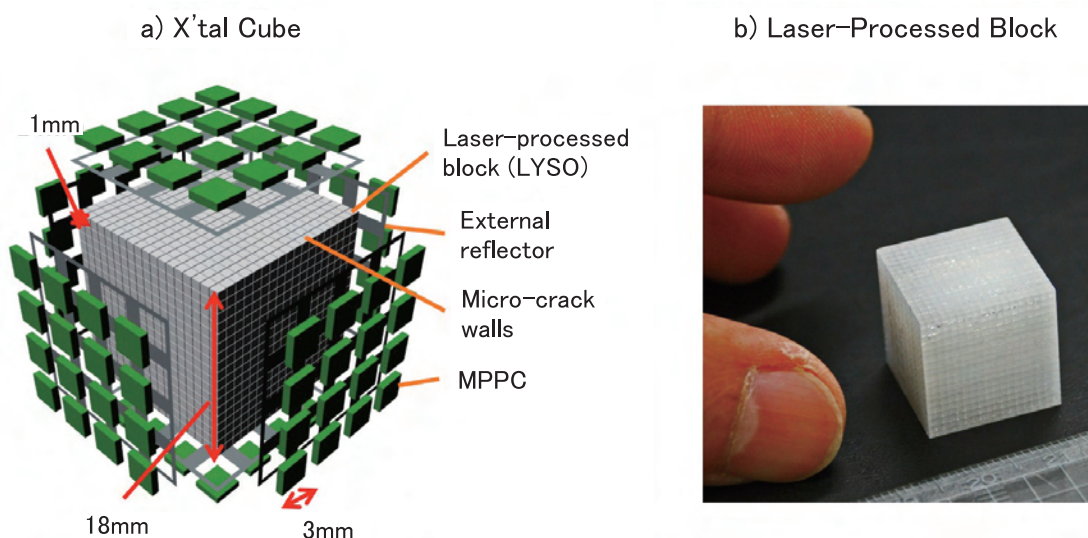


Fig.1 (a) Illustration of detector configuration and (b) photograph of the laser-processed block for a 1-mm X'tal cube.

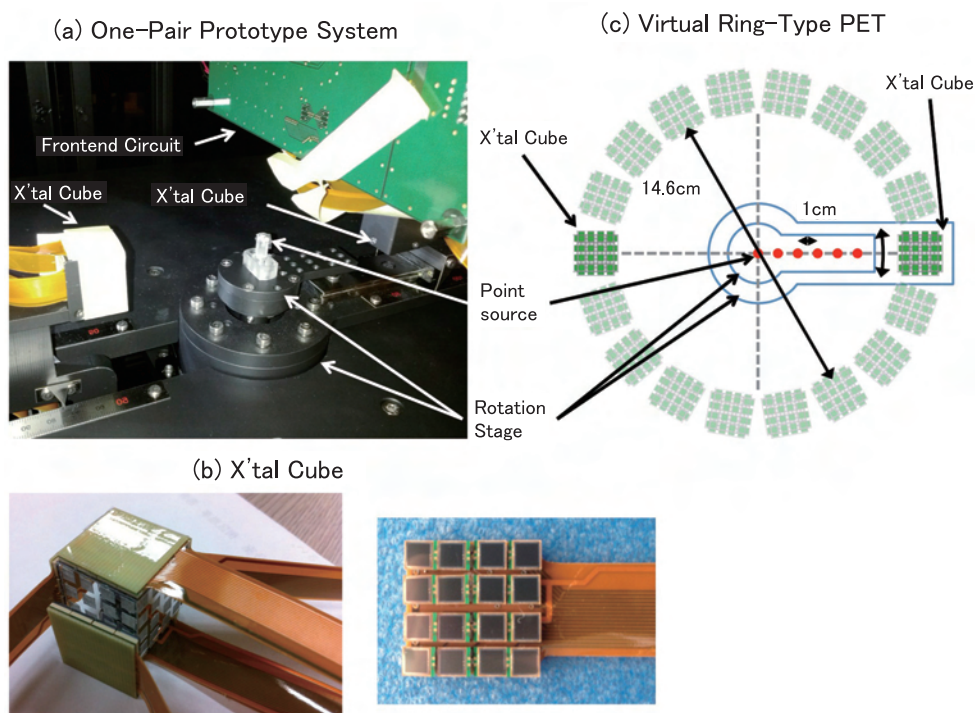


Fig.2 Photographs of: (a) the one-pair prototype system and (b) the X'tal cube. (c) Schematic illustration of the virtual ring-type PET scanner with a 14.6 cm diameter.

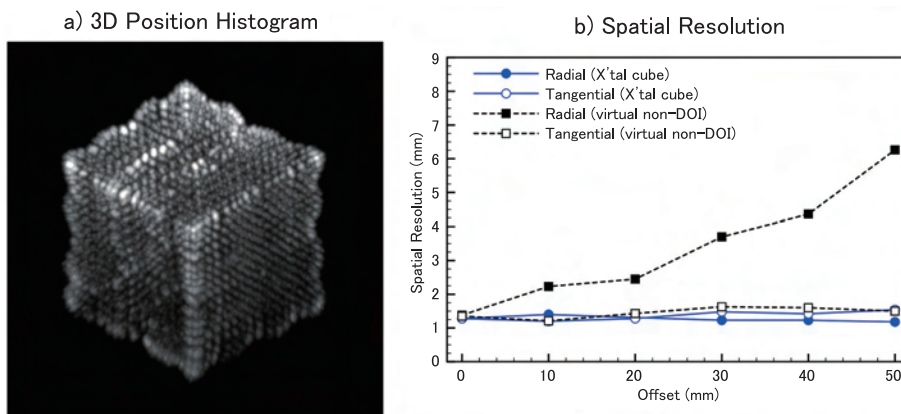


Fig.3 (a) 3D position histograms from the 511 keV uniform irradiation of the 1-mm X'tal cube and (b) radial and tangential FWHM resolutions for the 1-mm X'tal cube.

a 192-channel data acquisition system (Fig.2). Each X'tal cube consisted of the LYSO cubic crystal block of $(18 \text{ mm})^3$ in which the 3D square grids of 1 mm length were fabricated by internal laser processing. The 4×4 arrays of multi pixel photon counters (MPPCs) were optically coupled to each surface of the crystal block. The detector positions were automatically controlled to simulate a ring-type PET with a 14.6 cm diameter. Data were collected for all assumed detector positions and then a sinogram was obtained. The data were reconstructed using filtered back-projection. Fig.3(a) shows the 3D position histogram of the 1-mm X'tal cube obtained from the 511-keV uniform irradiation. Also, each spot corresponded to a 3D grid. Almost all the 3D grids on the 3D position histogram could be separated clearly. Fig.3(b) shows radial and tangential full width at half maximum (FWHM) resolutions for the 1-mm X'tal cube. Without DOI information, the spatial resolutions were degraded at off-center positions. The av-

erage spatial resolution of the 1-mm X'tal cube was 1.3 mm FWHM over the FOV. By applying deconvolution with the assumption that the point source was a Gaussian function of 1.0 mm FWHM, we estimated the average spatial resolution of the 1-mm X'tal cube as 0.83 mm FWHM. In conclusion, we confirmed the potential of the X'tal cube for uniform and high resolution imaging.

References

- [1] Yazaki Y, Inadama N, Nishikido F, *et al.*: Development of the X'tal Cube: A 3D position-sensitive radiation detector with all-surface MPPC readout, *IEEE Trans Nucl Sci*, 59(2), 462-468, 2012.
- [2] Yamaya T, Mitsuhashi T, Matsumoto T, *et al.*: A SiPM-based isotropic-3D PET detector X'tal cube with a three-dimensional array of 1 mm^3 crystals, *Phys Med Biol*, 56(21), 6793-6807, 2011.
- [3] Moriya T, Fukumitsu K, Sakai T, *et al.*: Development of PET detectors using monolithic scintillation crystals processed with sub-surface laser engraving technique, *IEEE Trans Nucl Sci*, 57(50), 2455-2459, 2010.

Highlight

Image-based head movement correction for reliable quantification of receptor binding in PET dynamic studies

Yoko Ikoma

E-mail: ikoma@nirs.go.jp

Positron emission tomography has been utilized for imaging neuroreceptors in the human brain. Because quantitative analysis of receptor binding potential (BP) usually requires 60-min PET scanning, head-movement correction is necessary for a reliable quantification. In the present study, a system for image-based motion correction was developed, and an optimal correction method was evaluated using a computer simulation and human data of [¹¹C]raclopride-PET.

Positron emission tomography (PET) can visualize receptor binding in living human brains. In this PET measurement for quantifying receptor binding potential (BP), a transmission scan is performed before administration of tracer to obtain the μ -map used for the attenuation correction, and after the tracer administration, a 60-90 min interval of consecutive emission data is acquired to obtain the time course of accumulated radioactivity. Therefore, head movement is often observed during the emission scanning, especially in the later frames, and it hampers reliable quantification. To correct head movement, in general, image-based or hardware-based motion correction is applied^[1-3]. In the image-based motion correction, information on head movement among time frames is computed by coregistering each frame of a reconstructed emission image to a reference frame image. Unlike hardware-based motion correction, this method is easy to implement and does not require an online tracking system. However, the reliability of frame-by-frame coregistration depends on the distribution of the radioisotope in emission images, signal-to-noise ratio, the reference image, and so on. Therefore, it is important to evaluate an optimal coregistration method according to specific administered tracers. In addition, frame-to-frame realignment of emission images causes a mismatch between the emission and transmission images, and it may result in error of the quantitative outcomes. In the present study, we developed a system for image-based motion correction in PET receptor imaging, and we evaluated an optimal method of image coregistration for PET studies with [¹¹C]raclopride by a computer simulation. Then, this methodology was applied to PET studies with [¹¹C]raclopride of normal volunteers, and the effect of this correction on quantitative analysis outcomes was investigated.



First, we constructed a data processing system for image reconstruction including head-movement correction for PET data acquired with Eminence SET-3000GCT/X (Shimadzu Corp., Kyoto, Japan). In this system, motion-corrected images are generated as follows (Fig.1). (1) A transformation matrix representing motion among time frames is calculated from automatic frame-by-frame coregistration using a reconstructed emission image. (2) A μ -map obtained through transmission scan is resliced using the transformation matrix so that its coordinate matches to the coordinate of each time frame of the emission image. (3) In the measured emission sinogram, that is a set of projection data of the administered tracer in the brain, attenuation is corrected frame-by-frame using attenuation data derived from forward-projection of the resliced μ -map. (4) Radioactivity image of each time frame is reconstructed by a filtered-back projection from the attenuation-corrected emission sinogram. (5) Each frame of the reconstructed radioactivity image is realigned to the coordinate of the first frame image using the transformation matrix.

Next, an optimal method of frame-by-frame image coregistration for estimating the transformation matrix was evaluated by a computer simulation. The emission sinogram that imitated human [¹¹C]raclopride-PET data with translation or rotation head movement was simulated, and reconstructed with or without attenuation correction. Each frame of these reconstructed images was automatically coregistered, using mutual information, to various reference images, such as the PET summation image of all frames, an early frame image, a high-count frame image, and a previous frame image. The reliability of coregistration was evaluated by comparing the estimated transformation matrix with true values. As a result, reconstructed images without attenuation correction could be coregistered precisely to early and high-count frame images.

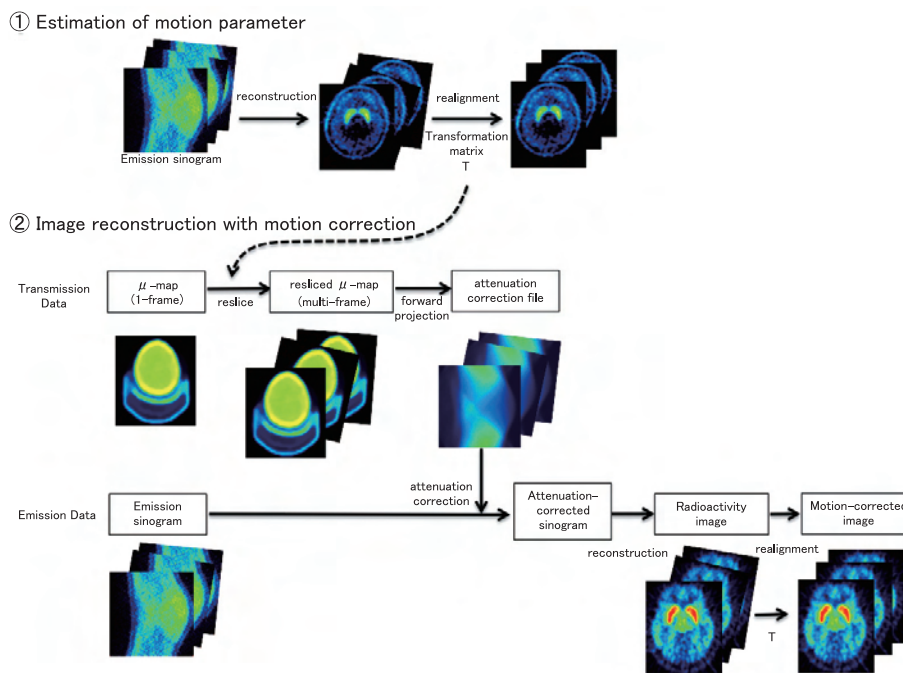


Fig.1 Strategy of image-based motion correction.

Finally, the image-based motion correction was applied to PET studies with [^{11}C]raclopride of normal volunteers. After the correction, reconstructed images were frame-to-frame realigned correctly (Fig.2), and discontinuity of time-activity curve in the striatum was mitigated (Fig.3). The binding potential estimated by a simplified reference tissue model became larger when obvious head movement was observed in the later frames.

In summary, head movement during a PET dynamic scan was accurately corrected by applying the optimal frame-by-frame coregistration and reconstruction with the resliced μ -map, and it remarkably improved the reliability of quantitative outcomes. This method is practical for clinical research, because it does not require a hardware system for online motion tracking and can be applied to all PET data, such as previous data acquired without motion tracking.

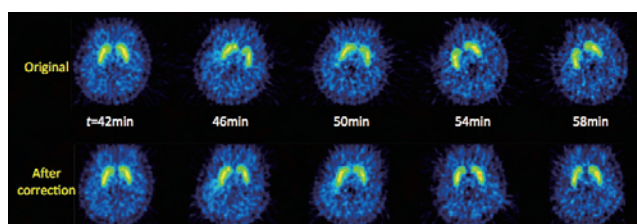


Fig.2 [^{11}C]raclopride-PET images of a normal volunteer before and after the motion correction.

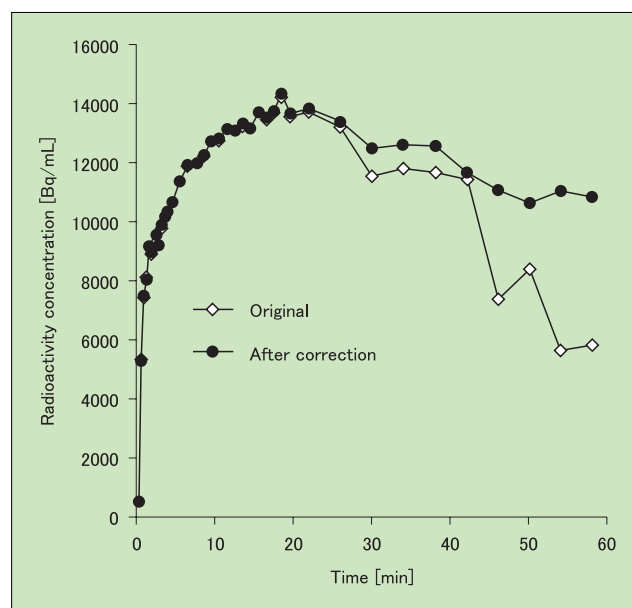


Fig.3 Typical example of time-activity curves for the striatum before and after the motion correction.

References

- [1] Mourik JEM, Lubberink M, van Velden FHP, *et al.*: Off-line motion correction methods for multi-frame PET data, *Eur J Nucl Med Mol Imaging*, 36, 2002-2013, 2009.
- [2] Wardak M, Wong KP, Shao W, *et al.*: Movement correction method for human brain PET images: application to quantitative analysis of dynamic ^{18}F -FDDNP scans, *J Nucl Med*, 51, 210-218, 2010.
- [3] Montgomery AJ, Thielemans K, Mehta MA, *et al.*: Correction of head movement on PET studies: comparison of methods, *J Nucl Med*, 47, 1936-1944, 2006.

Highlight

Development of a novel positron emission tomography probe ^{64}Cu -cyclam-RAFT-c(-RGDfK-) $_4$ for noninvasive visualization and quantification of tumor angiogenesis and monitoring of antiangiogenic efficacy via targeting the tumor $\alpha_v\beta_3$ integrin

Zhao-Hui Jin

E-mail: zhaohui@nirs.go.jp

Background and objectives

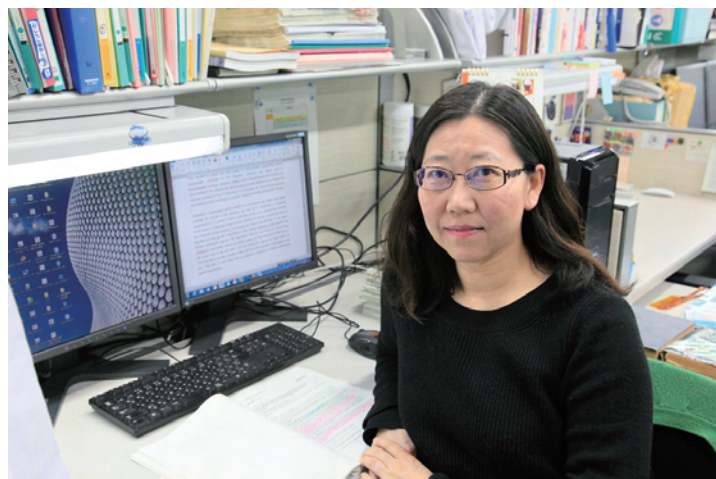
Angiogenesis, the formation of new blood vessels from pre-existing vasculature, in a tumor is a key feature of malignant solid tumors, plays a critical role in tumor growth, invasion, and metastasis, and has been accepted as an important target and indicator of therapeutic outcome and prognosis. $\alpha_v\beta_3$ Integrin, one of the key biomarkers for tumor angiogenesis, is a transmembrane glycoprotein receptor and highly expressed on activated endothelial cells during angiogenesis. Cyclic pentapeptides containing a tripeptide sequence RGD, cRGDs, are optimized synthetic ligands that have a high affinity and selectivity for $\alpha_v\beta_3$ integrin. RAFT-c(-RGDfK-) $_4$, designed and developed by Pascal Dumy and colleagues of Joseph Fourier University, is a tetrameric cRGD-containing peptide that is synthesized by separately grafting 4 cRGD motifs onto the upper side of the cyclic decapeptide platform called RAFT (regioselectively addressable functionalized template) to form the $\alpha_v\beta_3$ -targeting domain. On the lower side of RAFT, a variety of substances such as fluorescent dye, radioisotope or peptide can be linked to form the functional domain.

In collaboration with Dr. Dumy's group, we have developed a novel RAFT-c(-RGDfK-) $_4$ based positron emission tomography (PET) probe for noninvasive visualization and quantification of tumor angiogenesis and monitoring of antiangiogenic efficacy via targeting $\alpha_v\beta_3$ integrin^[1-3], as introduced in the following parts.

Major research results in FY 2011 for the development of ^{64}Cu -labeled cyclam-RAFT-c(-RGDfK-) $_4$.

1) Synthesis of cyclam-RAFT-c(-RGDfK-) $_4$ and radiolabeling with ^{64}Cu

RAFT-c(-RGDfK-) $_4$ was prepared through a combination of solid and solution-phase syntheses, and was conjugated with cyclam, a bifunctional chelator, to form a molecule (molecular weight ~ 5 kDa) for ^{64}Cu -labeling (Fig.1). The radiolabeling procedure for cyclam-RAFT-c(-RGDfK-) $_4$ is easy, mild, and straightforward. In brief, the peptide solution and $^{64}\text{CuCl}_2$ reconstituted in ammonium citrate buffer were mixed and incubated at 37°C within 1 h. The radiolabeling efficiency for cyclam-RAFT-c(-RGDfK-) $_4$ was $>99\%$, and the specific radioactivity that could be achieved was as high



as ~ 37 MBq/nmol.

2) In vitro and in vivo studies for determining the binding activity and specificity of ^{64}Cu -cyclam-RAFT-c(-RGDfK-) $_4$ for $\alpha_v\beta_3$ integrin

In vitro binding studies showed much stronger binding of ^{64}Cu -cyclam-RAFT-c(-RGDfK-) $_4$ for $\alpha_v\beta_3$ -overexpressing cells than for $\alpha_v\beta_3$ -negative cells, demonstrating its $\alpha_v\beta_3$ -binding activity and specificity. The $\alpha_v\beta_3$ specificity was further confirmed by the dose-dependent competitive binding inhibition using the $\alpha_v\beta_3$ -specific c(RGDfV) peptide. Compared to c(RGDfV), cyclam-RAFT-c(-RGDfK-) $_4$ showed a much higher affinity or avidity for $\alpha_v\beta_3$, as shown by comparing their IC₅₀ values (~ 39 nM for cyclam-RAFT-c(-RGDfK-) $_4$ versus ~ 2642 nM for c(RGDfV)).

Biodistribution studies demonstrated that ^{64}Cu -cyclam-RAFT-c(-RGDfK-) $_4$ had a rapid blood clearance, predominant renal excretion pathway, low-level uptake in nontumor tissues, and high tumor-to-background contrast. The tumor-targeting specificity of ^{64}Cu -cyclam-RAFT-c(-RGDfK-) $_4$ was confirmed by the blocking study.

3) Correlation of tumor $\alpha_v\beta_3$ integrin expression with tumor uptake of ^{64}Cu -cyclam-RAFT-c(-RGDfK-) $_4$

For determining the relationship, biodistribution assay was performed to measure the ^{64}Cu -cyclam-RAFT-c(-RGDfK-) $_4$ uptake values for various tumors, and the $\alpha_v\beta_3$ expression levels of these tumors were then quantified by SDS-PAGE/autoradiography. A linear and positive correlation was found between the $\alpha_v\beta_3$ expression and the tumor radioactivity accumulation of ^{64}Cu -cyclam-RAFT-c(-RGDfK-) $_4$.

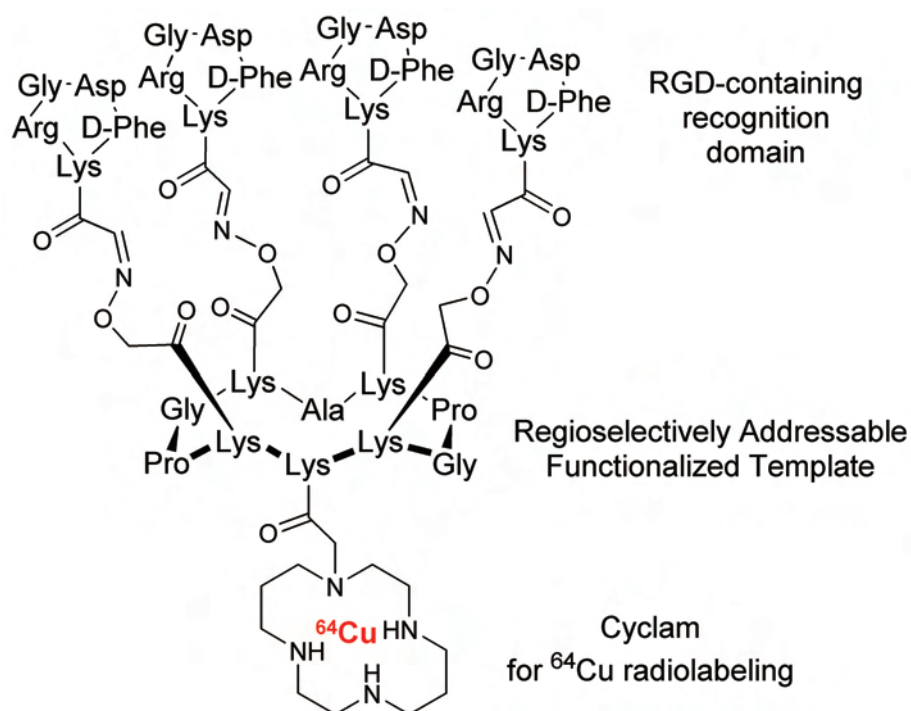


Fig.1 Molecular structure of ^{64}Cu -cyclam-RAFT-c(-RGDfK-)₄.

4) PET imaging of mice bearing tumors with different levels of $\alpha_v\beta_3$ integrin

^{64}Cu -cyclam-RAFT-c(-RGDfK-)₄ PET scans were finally performed in mice bearing tumors with different expression levels of $\alpha_v\beta_3$. As compared to HEK293(β_3) tumor with undetectable levels of $\alpha_v\beta_3$, HEK293(β_3) (high levels of $\alpha_v\beta_3$) and U87MG tumors (moderate levels of $\alpha_v\beta_3$) were clearly visualized with high contrast relative to the contralateral background at all the time points of 1-20 h p.i. The highest radioactivity accumulation in the tumor was visualized at 1 h p.i., and this was followed by a gradual washout with time. Fig.2 clearly shows a high, a moderate and a weak tumor uptake of ^{64}Cu -cyclam-RAFT-c(-RGDfK-)₄ for HEK293(β_3), U87MG and HEK293(β_1) tumors, respectively, corresponding to their $\alpha_v\beta_3$ expression levels. Overall, the PET images agreed well with the biodistribution data.

Major research results in FY 2012 for the application of ^{64}Cu -labeled cyclam-RAFT-c(-RGDfK-), for tumor angiogenesis study

1) Use of HuH-7 xenograft as a tumor angiogenesis model and PET imaging of tumor angiogenesis

We studied angiogenesis in a tumor xenograft derived from the $\alpha_v\beta_3$ -negative human hepatocellular carcinoma HuH-7 cell line to eliminate interference from $\alpha_v\beta_3$ integrin expressed on the tumor cells themselves. Our study proves that ^{64}Cu -cyclam-RAFT-c(-RGDfK-)₄ PET enabled visualization of tumor angiogenesis by targeting $\alpha_v\beta_3$ integrin. The imaging quality was good because the tumors could be clearly visualized at both 1 and 3 h p.i., which was supported by the biodistribution study showing high tumor-to-blood and tumor-to-muscle ratios of ~ 32 and ~ 7 , respectively, at 3 h p.i. In addition, no correlation was found between tumor

weight and tumor uptake (expressed as %ID/g, a percentage of injected dose per gram of tissue) of ^{64}Cu -cyclam-RAFT-c(-RGDfK-)₄, indicating that the tumor size itself is not a critical factor influencing tracer uptake.

2) Antiangiogenic efficacy as assessed and evaluated by PET imaging

Administration of the antiangiogenic drug TSU-68 (75 mg kg⁻¹ d⁻¹, i.p.) in HuH-7 tumor-bearing mice for 2 weeks resulted in retardation in tumor growth and reduction in tumor microvessel density (MVD) determined by CD31 immunostaining. The results obtained from the same set of experiments showed that the TSU-68-induced reduction in tumor MVD was accompanied by a reduction in the tumor standardized uptake value (SUV) determined by ^{64}Cu -cyclam-RAFT-c(-RGDfK-)₄ PET. Moreover, a positive and significant correlation was found between the tumor MVD and the corresponding SUV (either the mean or maximum value) or %ID/g evaluated by biodistribution assay. Representative PET images from the vehicle and TSU-68-treated mice acquired at 3 h p.i. of ^{64}Cu -cyclam-RAFT-c(-RGDfK-)₄ are shown in Fig. 3. Visually, the radioactivity was obviously lower in the tumors from the TSU-68-treated mice than in those from the controls. Further, while the radioactivity accumulated in the control tumors was homogeneous, the radioactivity signals in the TSU-68-treated tumors were heterogeneous. Autoradiographic examination and immunofluorescence staining (Fig.3) demonstrated the intratumoral colocalization of the tracer and vascular network distribution in which murine β_3 integrin was found positive. Taken together, our results strongly demonstrate that the antiangiogenic effects of TSU-68 can be monitored by quantitative ^{64}Cu -cyclam-RAFT-c(-RGDfK-)₄ PET imaging.

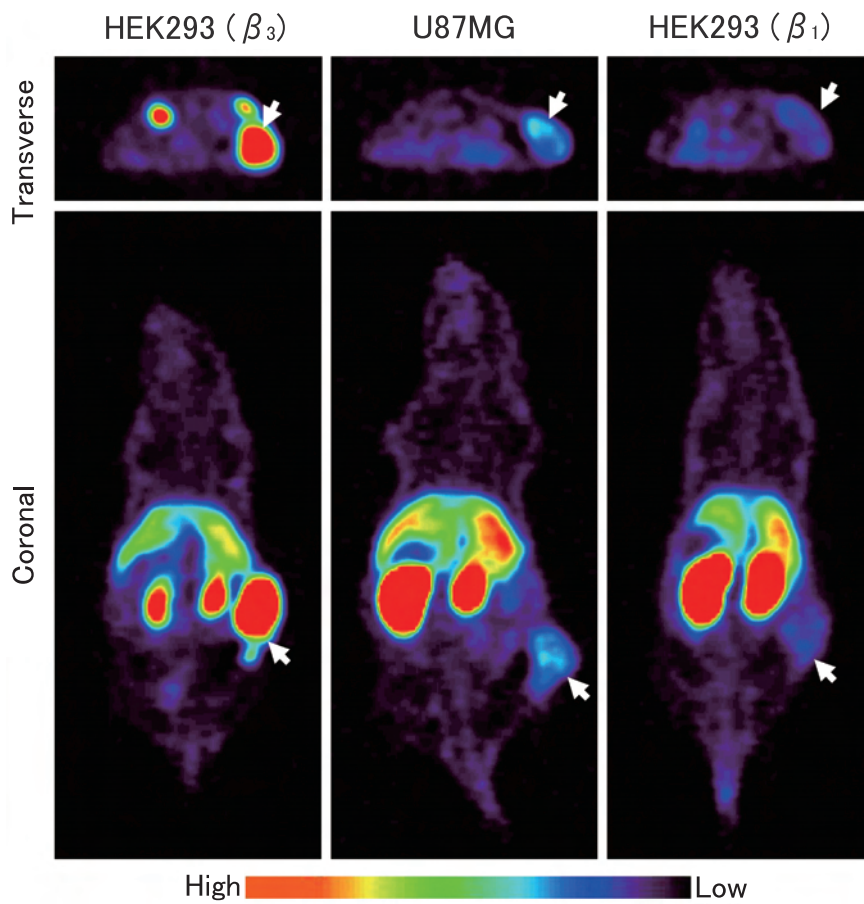


Fig.2 PET imaging of mice bearing subcutaneous HEK293(β_3), U87MG or HEK293(β_1) tumors at 3 h after i.v. injection of 11.1 MBq ^{64}Cu -cyclam-RAFT-c(-RGDfK) $_4$. Arrows indicate tumor localization.

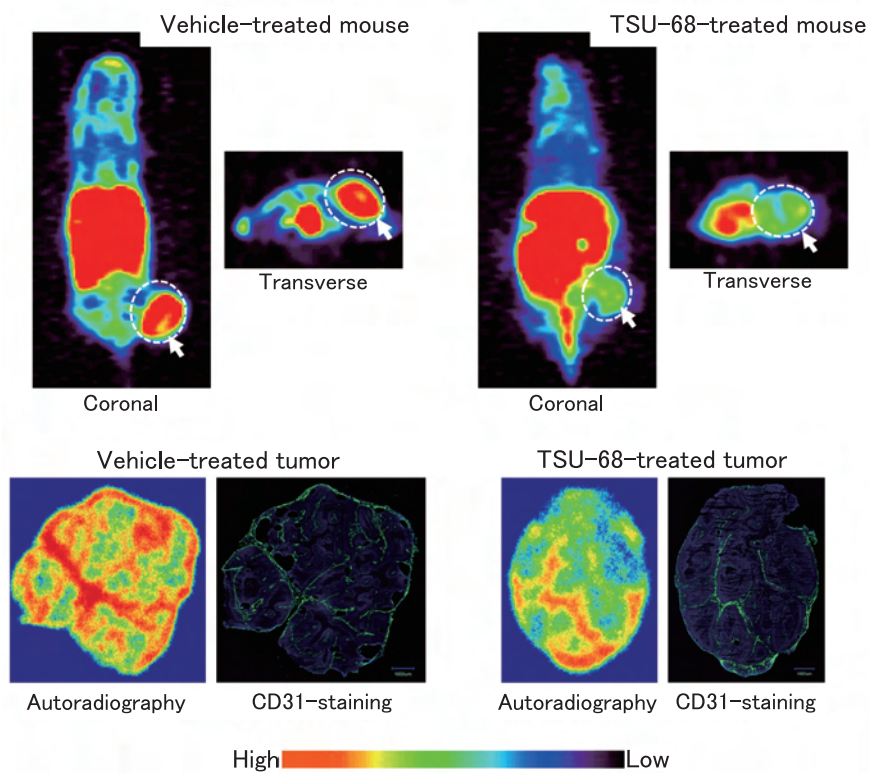


Fig.3 PET images of mice bearing subcutaneous HuH-7 tumor at 3 h after i.v. injection of 11.1 MBq ^{64}Cu -cyclam-RAFT-c(-RGDfK) $_4$ on day 15 after treatment with vehicle or TSU-68. Arrows indicate tumor localization. After PET imaging, tumors were excised, and autoradiographic examination and CD31 immunofluorescence staining were performed with the same whole-tumor sections.

Summary and prospectus

We have developed a PET probe ^{64}Cu -cyclam-RAFT-c(-RGDfK-)₄ that exhibited high binding affinity and specificity for the $\alpha_v\beta_3$ integrin, and favorable pharmacokinetics. Positive linear correlation was observed between tumor uptake of ^{64}Cu -cyclam-RAFT-c(-RGDfK-)₄ and tumor $\alpha_v\beta_3$ levels, which was also revealed by the noninvasive PET imaging study. We used murine xenografts from an $\alpha_v\beta_3$ -negative tumor cell line and showed that ^{64}Cu -cyclam-RAFT-c(-RGDfK-)₄ PET enables the clear visualization of tumor angiogenesis and helps monitor the effectiveness of antiangiogenic therapy. In future, we intend to determine whether this strategy is effective for tumors in which $\alpha_v\beta_3$ is expressed on both tumor cells and the neovasculature by using longitudinal PET imaging to detect not only changes in tracer uptake but also changes in the tracer distribution pattern. Further, it may also be applicable for monitoring angiogenic therapy in other angiogen-

esis-associated disorders such as ischemia, atherosclerosis, and myocardial infarction. Finally, because ^{64}Cu also emits β^- , the application of ^{64}Cu -cyclam-RAFT-c(-RGDfK-)₄ for internal radiotherapy to increase therapeutic gain should also be investigated.

References

- [1] Galibert M, Jin ZH, Furukawa T, *et al.*: RGD-cyclam conjugate: synthesis and potential application for positron emission tomography, *Bioorg Med Chem Lett*, 20, 5422-5425, 2010.
- [2] Jin ZH, Furukawa T, Galibert M, *et al.*: Noninvasive visualization and quantification of tumor $\alpha_v\beta_3$ integrin expression using a novel positron emission tomography probe, ^{64}Cu -cyclam-RAFT-c(-RGDfK-)₄, *Nucl Med Biol*, 38, 529-540, 2011.
- [3] Jin ZH, Furukawa T, Claron M, *et al.*: Positron emission tomography imaging of tumor angiogenesis and monitoring of antiangiogenic efficacy using the novel tetrameric peptide probe ^{64}Cu -cyclam-RAFT-c(-RGDfK-)₄, *Angiogenesis*, 15, 569-580, 2012.

Highlight

Tissue redox activity as a sensing platform for molecular imaging of cancer in vivo and in situ

Rumiana Bakalova

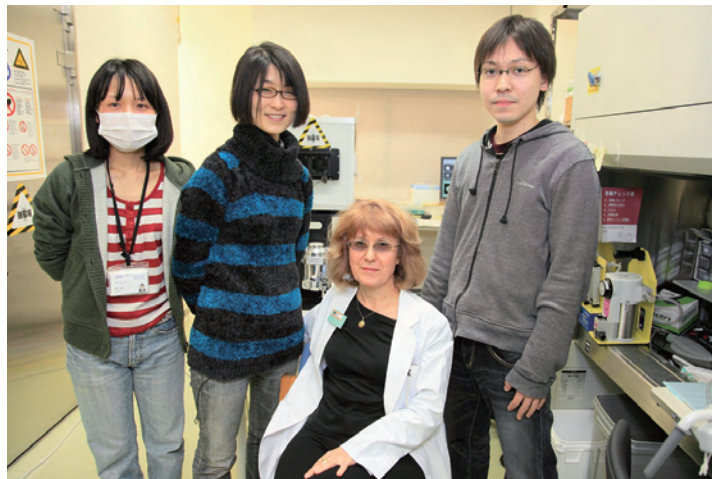
E-mail: bakalova@nirs.go.jp

Abstract

Experiences in free radical biology and medicine have shown the crucial role of redox signalling in carcinogenesis. The cells and tissues of healthy mammals are characterized by a low level of reactive oxygen species (ROS) and some constant (reference) level of reducing equivalents. Increasing the ROS above the critical level provokes genomic instability and normal cells become malignant.

The present study describes a universal methodology for direct imaging of tissue redox activity in carcinogenesis on intact animals; the method allows a differentiation of cancer development from the normal condition. Experiments were conducted on cancer-bearing mice (grafted with neuroblastoma, glioma or colon cancer) and healthy mice as controls. The tissue redox activity was visualized in vivo by nitroxide-enhanced MRI on anesthetized animals or in situ by EPR spectroscopy on isolated tissue and blood specimens. The method is based on the nitroxide redox cycle, coupled with appearance and disappearance of MRI/EPR signal. The half-life ($\tau_{1/2}$) of the nitroxide-enhanced MRI signal in the respective tissue was used as a diagnostic marker. The study provided direct evidence that healthy and cancer-bearing mammalian tissues were characterized by different redox activity — a basis for a cancer diagnostic term. The tissues (cancer and “normal”) of cancer-bearing mammals were characterized by a longer-lived MRI signal, a decrease of total antioxidant capacity, and an increase of matrix metalloproteinases (MMP2 and MMP9) relative to controls, indicating a higher oxidative activity. The tissues of healthy organisms were characterized by a shorter-lived MRI signal and a higher total antioxidant capacity, indicating a high reducing activity.

An important observation is that the oxidative status of non-cancer tissues of cancer-bearing organisms (even far from the primary tumour locus) increases with cancer progression and they become susceptible to oxidative stress and damage. The non-cancer tissues also have to be considered as a therapeutic target. The study directly relates to the cancer diagnosis and assessment of cancer progression, using molecular imaging, as well as to the therapeutic planning strategy. Since, the tissue redox status is very sensitive to radiotherapy and chemotherapy, the



proposed methodology can be used for assessment of therapeutic effects in dynamics using molecular imaging. The method is simple and applicable on isolated tissue and blood specimens. It has a real potential to be applied for in situ and in vivo imaging diagnosis on humans after development of cell-penetrating nitroxide probes with high contrast, low toxicity and minimal side effects.

Introduction

Over 50 years of experiences in free radical biology and medicine have shown the crucial role of redox signalling in carcinogenesis^[1]. The cells and tissues of healthy mammals are characterized by a low steady-state level of oxidizers (e.g., reactive oxygen species (ROS) and reactive nitrogen species (RNS)) and some constant (reference) level of reducers (e.g., endogenous redox pairs: NADH/NAD⁺, NADPH/NADP⁺, FADH₂/FAD, reduced/oxidized glutathione, reduced/oxidized ascorbate, etc.). It is widely accepted that increasing the ROS/RNS above the critical level provokes genomic instability and triggers uncontrolled proliferation. The normal cells become malignant.

Cancer cells are characterized by an abnormal production of reducing equivalents as a result of accelerated glycolysis (Warburg effect) and the pentose phosphate cycle, but also by a rapid consumption of these reducers to maintain accelerated anabolism, which is necessary for cell proliferation and immortalization. Cancer cells need also a lot of antioxidants to maintain ROS/RNS below the threshold level, above which apoptosis and cell death are induced, but this level has to be high enough to ensure genomic instability. These processes provoke redox disbalance in cancer and this parameter can be used as a diagnostic marker, a therapeutic target, and a hallmark for evaluation and planning of the therapeutic strategy.

There is no universal non-invasive methodology for estimation of tissue redox activity in intact mammals. The oxidizing and/or reducing status of tissues are determined by the levels of many parameters (e.g., ROS/RNS of different types and origins, products of free radical oxidation of biomacromolecules, status of natural non-enzymatic and enzymatic antioxidant systems, status of various endogenous redox pairs, etc.). Each parameter is analysed separately by different methodologies in vitro or in situ. The estimation of redox status of cancer and healthy tissues is based on comparative analysis of one or several of these parameters and the conclusions are usually controversial.

We propose an approach for direct imaging of tissue redox activity in vivo on intact healthy and cancer-bearing mammals, which allows a differentiation of cancer development from the normal (healthy) condition. The method is based on the redox cycle of *cell-penetrating nitroxide derivatives* and their MRI (magnetic resonance imaging) contrast properties, which makes them useful molecular sensors for tissue redox activity (Fig.1). The nitroxide radical (which is characterized by T_1 contrast) participates in electron-transfer reactions with oxidizers and reducers with formation of contrast or non-contrast intermediate products^[2]. The rate constants of these reactions determine the intensity of the nitroxide-enhanced MRI signal in living cells and tissues. In healthy mammals, the half-life of the nitroxide-enhanced MRI signal ($\tau_{1/2}$) in the selected region of interest (ROI) is considered as a reference value of tissue redox activity in the normal condition

(healthy organism). We established that in the same or similar ROI of cancer-bearing mammalian tissues, $\tau_{1/2}$ was completely different from the reference value and this parameter is a valuable diagnostic marker for carcinogenesis.

Nitroxide radical can also be characterized by electron paramagnetic resonance (EPR) spectroscopy, allowing determination of the exact concentration and redox status of nitroxide derivative in cancer or non-cancer tissues. The comparative analysis of the results, obtained by both imaging techniques, gives accurate information about tissue redox activity in vivo and in situ.

Experimental

In our study, we used cell- and blood-brain barrier (BBB)-penetrating nitroxide with DNA-annealing and anti-cancer effects – nitroxide-labelled nitrosourea (SLENU), for MR imaging of tissue redox activity in healthy and cancer-bearing mice (grafted with neuroblastoma, glioma or colon cancer). The aims of the study were to examine: (i) which of the two processes – oxidation or reduction, dominates in cancer and non-cancer tissues, using a single measurement on intact mammals; (ii) whether the nitroxide-enhanced MRI is suitable for cancer diagnosis in various cancer models; and (iii) what are the potential molecular mechanisms underlying redox signalling in carcinogenesis.

All experiments were conducted in accordance with the guidelines of the Physiological Society of Japan and were approved by the Animal Care and Use Committee of NIRS.

Several experimental schemes were used: (i) comparison of tissue redox activity between healthy and cancer-bearing mice; (ii) comparison of tissue redox activity between cancer-bearing mice in different stages of cancer development (early, intermediate and terminal); (iii) investigation of the molecular mechanisms underlying redox signalling in carcinogenesis – from early to terminal stages of cancer, including the role of matrix metalloproteinases, total antioxidant capacity, reactive oxygen species and integrin signalling cascade.

To distinguish the tissues of healthy mice from those of cancer-bearing mice, we used the following terminology: normal tissue – tissues of healthy mice (controls); “normal” tissue – non-cancer tissues of cancer-bearing mice; and cancer tissue – tissue in the cancer area, which is visualized structurally by MRI. Representative figures are presented below. Details are described in our recently published studies^[2,3].

Results

Fig.2A shows typical kinetics of MRI signal intensity in the brain (ROI1) and surrounding tissues (ROI2) of healthy mice after injection of nitroxide. In both ROI, the signal increased after injection, followed by rapid decrease to the baseline. The half-life of nitroxide-enhanced MRI signal ($\tau_{1/2}$) was ~ 80 s. This value can be considered as a reference for the redox activity of both tissues at normal conditions (e.g., healthy mice). The increase of the MRI signal in the beginning was due to the presence of nitroxide in the blood and its penetration and accumulation in the subsequent tissue, while the rapid decrease was due to its reduction to non-contrast hydroxylamine in the cells. This was confirmed by EPR spectroscopy on isolated tissue specimens. This profile of the histograms indicated a high reducing activity of normal (healthy) tissues to the nitroxide radical.

In neuroblastoma-bearing mice (in the terminal stage of cancer), the kinetics of the MRI signal intensity in both ROIs after in-

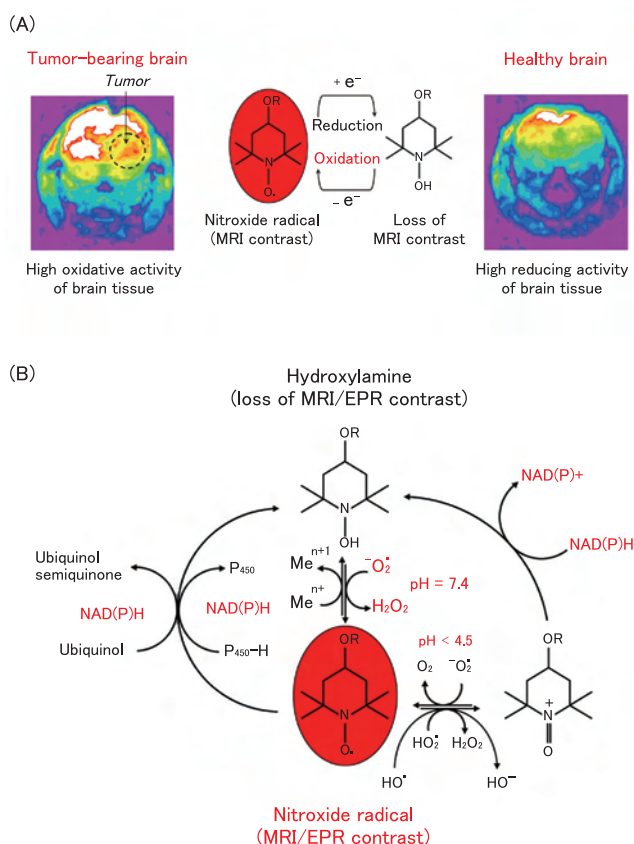


Fig.1 (A) Magnetic resonance imaging of carcinogenesis based on tissue redox activity (the principle of the method). T_1 -weighted MR images (gradient-echo sequence) of mouse brain, obtained ~ 2 min after injection of nitroxide. (B) Molecular mechanism(s) participating in the reduction and oxidation of nitroxide derivative, which reflects MRI and EPR signal intensity^[3].

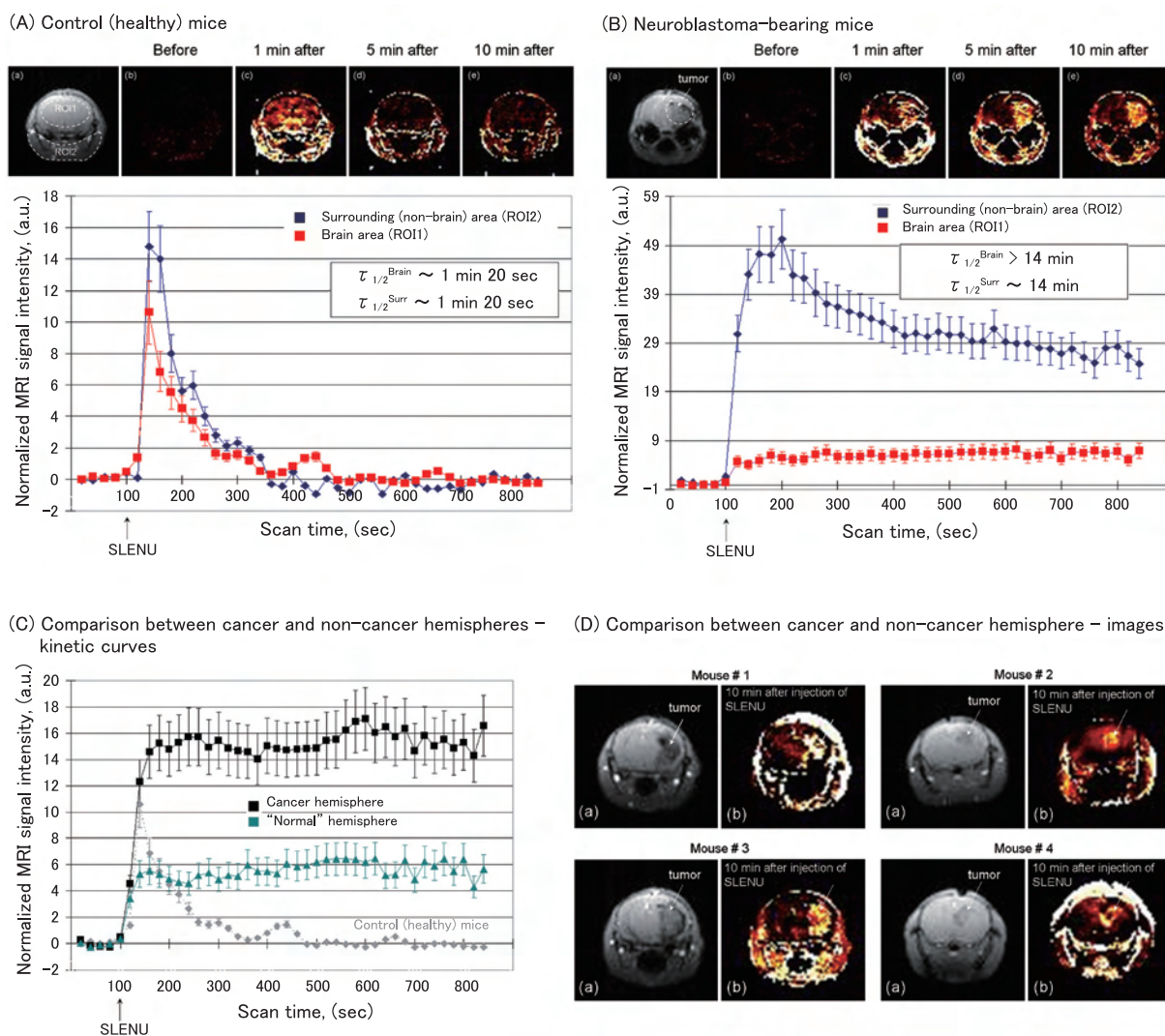


Fig.2 Healthy and neuroblastoma-bearing mice. (A) Kinetics of the nitroxide-enhanced MRI signal in the brain (ROI1) and surrounding tissues (ROI2) of healthy mice. The data are mean \pm SD from 10 animals. ROI are indicated with dotted lines on MR images: (a) MR image of mouse brain (control); (b-e) extracted MRI signal enhancement, obtained after injection of SLENU. (B) Kinetics of the nitroxide-enhanced MRI signal in the brain (ROI1) and surrounding tissues (ROI2) of neuroblastoma-bearing mice. The data are mean \pm SD from 10 animals. The tumor area is indicated with a dotted line on the MR images: (a) MR image of mouse brain; (b-e) extracted MRI signal enhancement, obtained after injection of SLENU. The MRI signal intensity in the tumor area is markedly higher in comparison with other areas. (C) Kinetics of the nitroxide-enhanced MRI signal in a cancer hemisphere (black line) and a "normal" hemisphere (green line) of neuroblastoma-bearing mice. The data are mean \pm SD from 10. Kinetics of the nitroxide-enhanced MRI signal in healthy brain is given for comparison (gray dotted line). (D) MR images of brain of neuroblastoma-bearing mice: (a) MR image of mouse brain; (b) extracted MRI signal enhancement, obtained after injection of SLENU. The MRI signal intensity in a cancer hemisphere is markedly higher in comparison with a "normal" hemisphere. All MR images were obtained by T₁-weighted gradient-echo sequence^[3].

jection of SLENU was completely different from the reference profiles (Fig.2B). In ROI1, the signal increased after injection and reached a plateau without decreasing within 14 min ($\tau_{1/2} > 14$ min). In ROI2, the signal increased after injection, then decreased slowly without reaching the baseline within 14 min ($\tau_{1/2} \sim 14$ min). These histograms indicated a high oxidative activity of the cancer tissue and surrounding "normal" tissues of cancer-bearing mice to the nitroxide radical. This was also confirmed by the pharmacodynamics and redox status of nitroxide in the brain, detected by EPR spectroscopy on isolated tissue specimens.

The kinetic curves of the MRI signal had the same profiles in both hemispheres – cancer-bearing and "normal" (Fig.2C), however the signal intensity was significantly higher in the cancer area (Fig.2D). This was direct evidence about the higher oxidative ac-

tivity of cancer tissue in comparison with "normal" tissues of cancer-bearing organism and tissues of healthy organism.

Similar results were obtained on glioma-bearing and colon-cancer bearing mice in the terminal stage of cancer^[3]. The data from biochemical analyses showed an enhancement of the plasma matrix metalloproteinases (MMP2 and MMP9), a decrease of tissue total antioxidant capacity, and an activation of integrin-signalling cascade in cancer-bearing mice, in comparison with healthy mice (Fig.3).

Conclusion

In conclusion, the study shows that tissue redox activity can be used as a sensing platform for molecular imaging of cancer by nitroxide-enhanced MRI and cell-penetrating nitroxides. We give

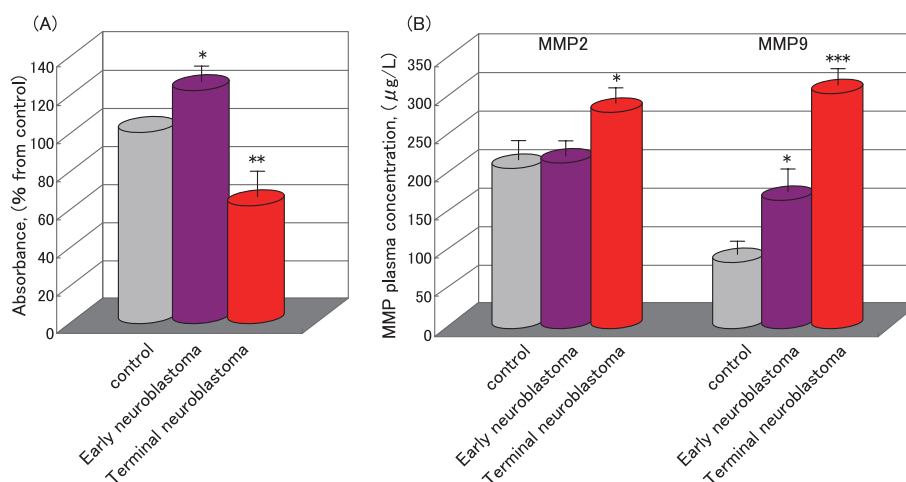


Fig.3 (A) Total antioxidant capacity of brain tissue in healthy and neuroblastoma-bearing mice, measured with the OxiSelect™ Total Antioxidant Capacity Assay Kit (Cell Biolabs, Inc.). The data are mean \pm SD from 4 animals for each group. (B) Plasma levels of matrix metalloproteinases (MMP2 & MMP9) in healthy and neuroblastoma-bearing mice, measured by Enzyme-Linked Immunosorbent Assay. The data are mean \pm SD from 4 animals for each group. * $p < 0.05$; ** $p < 0.01$; *** $p < 0.001$ vs control group (Clin Cancer Res, 19, 2503-17, 2013).

direct proof in vivo that the tissues of cancer-bearing mammals are characterized by high oxidative activity, while the tissues of healthy organisms are characterized by high reducing activity to the nitroxide. The high oxidative activity of cancer tissue is a fact despite hypoxia development in solid tumours. It relates to the abnormal production of ROS/RNS, but not to high oxygen tension. This is in agreement with the widely-accepted opinion that cancer cells are characterized by increased production of ROS/RNS relative to normal cells, which ensures genomic instability^[1].

The most significant observation is that the oxidative status of non-cancer tissues of cancer-bearing organisms (even far from the primary tumour locus) increases with cancer progression and they become susceptible to oxidative stress and damage. This finding shows that it is necessary to develop a more tolerant and efficient therapeutic strategy. In this context, combining anticancer therapy with protection of non-cancer tissues against oxidative stress could be essential for survival and recovery of the organism. Since tissue redox status is very sensitive to radiotherapy and chemotherapy, the proposed methodology can be used for dynamic assessment of therapeutic effects using molecular imaging (MRI/EPR).

The present study has a high translational relevance. It is directly related to cancer diagnosis, assessment of cancer progression, and planning of therapeutic strategy. It shows that the tissue redox balance is very sensitive to the cancer development and can be used as a hallmark of carcinogenesis. The method is simple and applicable to isolated tissue and blood specimens. We think it has a real potential for future applications to in vivo imaging diagnosis in humans.

References

- [1] Trachootham D, Alexandre J, Huang P.: Targeting cancer cells by ROS-mediated mechanisms: a radical therapeutic approach?, *Nat Rev Drug Disco* 8, 579-91 2009.
- [2] Zhelev Z, Gadjeva V, Aoki I, et al.: Cell-penetrating nitroxides as molecular sensors for imaging of cancer in vivo, based on tissue redox activity. *Mol Biosyst*, 8, 2733-2740, 2012.
- [3] Zhelev Z, Aoki I, Gadjeva V, et al.: Tissue redox activity as a sensing platform for imaging of cancer based on nitroxide redox cycle, *Eur J Cancer*, 49, 1467-1478, 2013.

Highlight

Integrating cognitive neuroscience: from molecules to neural responses, to society

Makiko Yamada

E-mail: myamada@nirs.go.jp

The evolution of cognitive neuroscience has been largely driven by the development of quantitative measures of human brain function (e.g., fMRI). This methodological advancement has enabled researchers to address hypotheses that were previously inconceivable, such as a causal relationship between patterns of neural activity, cognitive processes and complex human behavior. In addition to the quest for localization of function, another approach to study the human mind has been nurtured by examining molecular mechanisms, particularly in clinical domains. An emerging emphasis is now being placed on integrating multiple levels of neural responses from a molecular system to a neural response/circuit - to produce adaptive behavior, paralleling the social world in which humans live.

Integration of different disciplines has also borne fruit in the field of cognitive neuroscience by the convergence of perspectives (e.g. neuroscience, social psychology, economics, and ethology). This new wave of research has moved past basic work aimed at understanding brain function toward examining the neural underpinnings of issues critically important to humanity. This is admittedly a lofty goal, but cognitive neuroscience has already made significant contributions across several spheres of society, given by an illuminating example of our study, which is the integration of cognitive neuroscience and the law⁽¹⁾.

Neural circuits for mitigating criminal sentences

Philosophers, psychologists and legal scholars have long debated whether mercy, sympathy and compassion should reduce moral culpability of defendants in criminal cases. People have negative emotional responses to a wide range of situational factors that are not normatively justifiable legally. Social and moral neurosciences provide converging evidence of the interplay between negative emotion and moral judgments (e.g., a trolley dilemma), but the influence of sympathy on legal decision-making is unknown. The legal domain is unusual because it may be especially challenging to map emotions into numerical legal outcomes. Uncovering the cognitive and neural mechanisms of sympathy that motivate mitigation will inform the role of emotion in the jurors' decision process, and what role emotional evidence can and should play in trials.



We measured brain activity using functional MRI while subjects were making hypothetical sentence reduction decisions in dramatic scenarios adapted from actual murder cases. Mitigating circumstances were of two types: Those that would induce sympathy, and those that would not. The sympathy scenarios included desperate situations of defendants suffering from domestic violence, disease, or poverty. After reading about the circumstances, subjects decided how much they would change the sentence given for the defendant (initially 20 years) if they were on a jury (Fig.1A). After scanning, subjects were again presented with the same scenarios and asked to rate how much sympathy they felt for the defendant. Behavioral performance confirmed the internal validity of the sympathy manipulation (Fig.1B).

We first searched for brain regions that responded, during the description, to the subjects' trial-by-trial ratings of sympathy and their amounts of punishment reduction. Activity in the precuneus, dorsomedial prefrontal cortex (DMPFC) and left temporo-parietal junction (TPJ) were correlated with sympathy ($P < 0.05$, small-volume-corrected; Fig.1C). Signal increase in the precuneus, DMPFC and anterior cingulate cortex (ACC) were also associated with the reduction of punishment ($P < 0.05$, small-volume-corrected, Fig.1C).

The DMPFC is involved in general mentalizing and is active when empathizing with others in pain. The precuneus has been linked to subjective perspective taking. The TPJ is also commonly identified as a part of the theory-of-mind circuit and was activated in one study on judging innocence of intentions. This suggests that the sympathy judgment is an engagement with a reasoned simulation of what the defendant was thinking when committing the crime or how most people would judge the normative basis for mitigation. Precuneus activation is also correlated with more iterated steps and higher-value strategic thinking in game theory

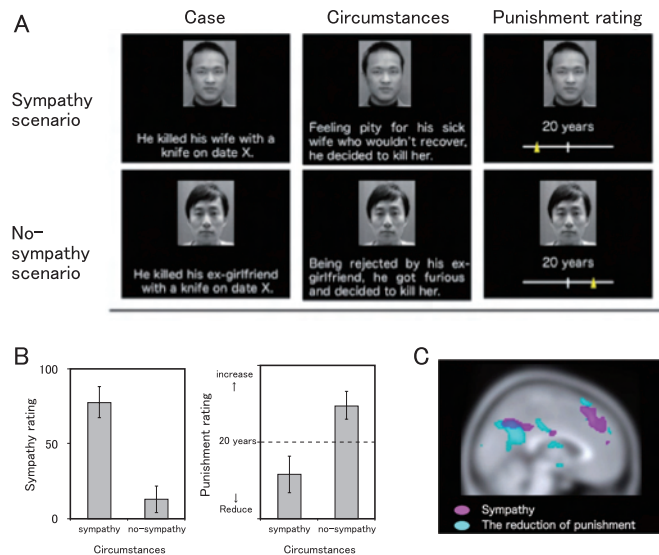


Fig.1 (A) Study paradigm. (B) Mean sympathy ratings for sympathy and no-sympathy trials (left), and mean punishment ratings for sympathy and no-sympathy trials (right). (C) Brain regions activated during trial-by-trial sympathy and punishment reduction. Regions in which activity correlated with parametric regressors of increasing sympathy (magenta) and reduced punishment (cyan).

tasks. The overlapping precuneus activity between a feeling of sympathy and judged mitigation of punishment suggests that the precuneus may be a region that accepts emotional judgment input, and maps it into concrete punishment actions. Activations in the ACC and caudate are interpreted as conflict resolution and pro-social choices, respectively, which are associated with mitigating behavior.

We note that one fMRI study reports right DLPFC activity associated with responsibility judgments. The absence of DLPFC activation in our study is possibly because there is no doubt about the defendants' guilt, so the most morally burdensome question of guilt versus innocence is resolved (the DLPFC is discharged from jury duty, so to speak).

Next, we constructed an individual-specific measure of an inclination to mitigate, by reducing sentences, as a function of sympathy. The b_1 coefficient of the regression in punishment = $b_0 + b_1 \cdot \text{sympathy} + \text{error}$ represents a complex mapping from an emotional response to a number representing prison time for a defendant (a years-per-emotion coefficient).

A negative linear regression between the individual-specific b_1 coefficient and BOLD responses in sympathy minus no-sympathy trials found activity in the right middle insula ($P < 0.05$, small-volume-corrected, Fig. 2). Individuals who had larger activities in the insula when reading circumstances showed higher tendencies to mitigate, reducing sentencing years more as their sympathy increased. The middle or posterior insula has been linked to interoceptive processing in various social tasks (e.g., inequity), which suggests this area is sensitive to emotions linked to sociality. Our study provides unusual evidence of this processing associated with a unique high-impact social judgment that affects others.

Taken together, the identified brain activity is encouraging about the capacity of the average brain to translate sympathetic feelings into appropriate legal action. Activity in these "sympathy" regions is evident in our study when judging sympathy alone, and in choosing sentence mitigation. However, not every brain maps sympathy to prison sentences in the same numerical way (as reflected in differential mid-insula activity). Differences represent a

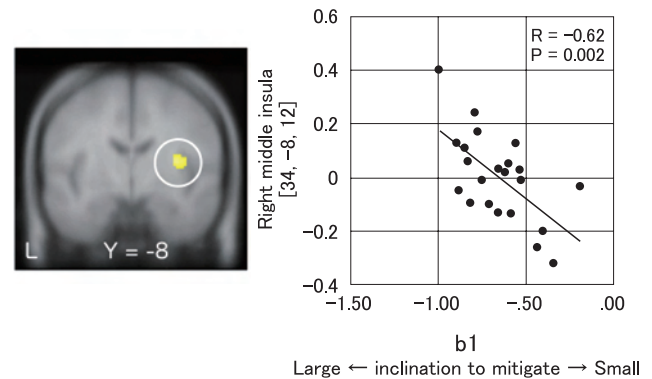


Fig.2 Individual differences in inclination towards mitigation. Activation in the right middle insula in the contrast sympathy minus no-sympathy trials correlated with the participant-wise coefficient of mitigation.

legal challenge about how to tolerate and weigh differential juror responses. There is also mixed evidence about the normative basis of legal judgment, including a recent finding that judges' decisions are affected by timing of meals.

Finally, we note that many legal principles treat emotional responses as likely to be prejudicial and prone to inflammatory manipulation (i.e., an ideal juror would suppress them, and legal rules limit their influence). Weighing mitigating circumstances during sentencing (*after* a verdict) represents an unusual case in which emotional sympathy judgment is actually required. Ironically, the fact that sympathy is clearly evident in brain activity, and influences sentence mitigation (as it should), raises interest in the opposite question: Can people also suspend emotions when the law instructs them to? More generally, a deeper understanding of the brain could help figure out how highly-evolved brain structures, which were sculpted to maintain order in small-scale ancestral societies, can be put to work under modern legal rules in much more challenging cases, to create modern justice.

References

- [1] Yamada M, Camerer CF, Fujie S, *et al.*: Neural circuits in the brain that are activated when mitigating criminal sentences, *Nat Commun*, 3(759), doi: 10.1038/ncomms 1757, 2012.

Highlight

β -Amyloid in Lewy body disease is related to Alzheimer's disease-like atrophy

Hitoshi Shimada

E-mail: shimada@nirs.go.jp

Introduction

Dementia with Lewy bodies (DLB) and Parkinson's disease with dementia (PDD) are categorized as belonging to the same spectrum, Lewy body disease with dementia. In addition to pathognomonic Lewy body pathology, DLB/PDD frequently has Alzheimer's disease (AD)-type pathology, particularly amyloid beta ($A\beta$) plaque. The contribution of $A\beta$ to the development of DLB/PDD remains unclear.

More than half of all DLB patients, and about one-third of all PDD patients had a cortical $A\beta$ burden in previous studies using [^{11}C]PIB-PET. Meanwhile, previous MRI volumetric studies suggested that DLB/PDD patients showed the AD-like cortical atrophy in several brain regions including the parahippocampal area. It is still unclear, however, whether the AD-like brain atrophy observed in DLB/PDD is associated with $A\beta$ burden or not.

To elucidate this issue, we compared the grey matter volume measured by voxel-based morphometry (VBM) among DLB/PDD patients with and without cortical $A\beta$ burden, AD patients, and healthy control subjects.

Methods

1) Subjects

Participants were 8 patients with DLB, 7 patients with PDD, 13 patients with AD, and 22 healthy controls (HC) diagnosed as PIB-negative (PIB (-)) by visual assessment of distribution volume ratio (DVR) images of [^{11}C]PIB PET (Table 1).

2) PET and MR images acquisition

A dose of [^{11}C]PIB was intravenously injected and sequential PET scans were performed for 90 min by Siemens ECAT EXACT HR+ scanner.

Subjects were also scanned with a 3D T1-weighted turbo gradient echo sequence on a Philips 1.5T Intera.

3) PET data preprocessing

All imaging data were preprocessed and analyzed with SPM5. We estimated DVR using Logan plot graphical analysis with the cerebellum as the reference region. VOIs were identified on DVR images in each subject's frontal, medial and lateral temporal, pa-



rietal, occipital, anterior and posterior cingulate and sensorimotor cortices and striatum in both hemispheres using the Wake Forest University (WFU) PickAtlas.

Subjects with significantly increased DVR greater than or equal to mean + 2.5 SD of the HC group in at least one brain region were classified as PIB(+), and subjects with no significantly increased PIB uptake in any brain region were classified as PIB (-). Furthermore, voxel-based analysis of DVR among the HC, PIB (-) and PIB(+) DLB/PDD, and AD groups was performed.

4) Voxel-based morphometry

We performed VBM analysis using the unified segmentation approach implemented in SPM5 for each 3D T1-weighted MR image. VOIs were identified on modulated, normalized and warped class images using the WFU PickAtlas.

Table 1 Demographic and neuropsychological test results of participants *Mov Disord*, 28(2), 169-75, 2013.

	HC	DLB/PDD	AD
Number of subjects	17	15(DLB8/PDD7)	13
Male : Female	11:6	9:6	3:10
Age	68.3±9.7	72.9±5.6	75.7±4.6
Disease duration (yr)	—	4.8±2.5	3.0±1.9
UPDRS motor part	—	30.6±16.6	—
MMSE	28.2±2.1	21.8±3.2	19.5±2.7
FAB	15.8±1.6	11.5±3.5	11.7±3.6
NPI	0.1±0.5	7.2±6.6	5.3±6.7

Values are listed as mean±SD.

HC: healthy controls, DLB: dementia with Lewy bodies, PDD: Parkinson's disease with dementia, AD: Alzheimer's disease, UPDRS: unified Parkinson's disease rating scale, MMSE: mini-mental state examination, FAB: frontal assessment battery, NPI: neuropsychiatric inventory

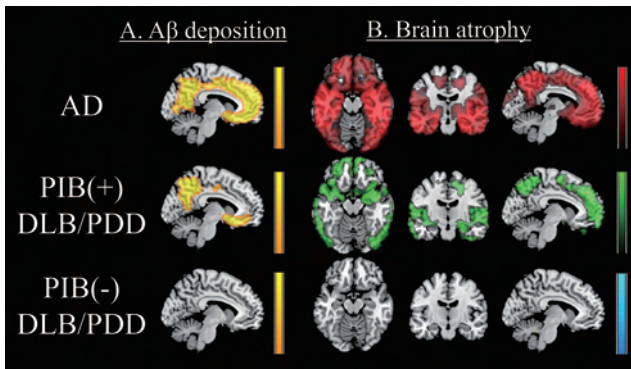


Fig.1 *Mov Disord*, 28(2), 169-75, 2013.

Results

1) PET

All HCs were PIB (-), while all AD patients, half (4/8) of the DLB patients and 29% (2/7) of the PDD patients were PIB(+). There were no significant differences between the PIB (-) and PIB(+) DLB/PDD groups in respect to any clinical profiles.

All PIB(+) DLB/PDD patients showed a similar distribution pattern of increased DVR in the brain to AD patients (Fig.1A).

2) Voxel-based morphometry

SPM analysis showed more profound cortical atrophy in both the AD and PIB(+)/DLB/PDD groups than in the HC group especially in the temporal (including parahippocampus) and parietal areas (including precuneus) (Fig.1B), whereas the PIB (-) DLB/PDD group did not show significant cortical atrophy. The brain regions where grey matter volume was significantly reduced compared to the HC group in the PIB(+) and PIB (-) DLB/PDD groups overlapped with those in the AD group by 95.2% and 0%, respectively.

VOI analysis (Table 2) revealed that, compared with the HC group, parahippocampal grey matter volumes were reduced in both the PIB(+) DLB/PDD (Z score = 1.94 ± 0.60 , $p = 0.002$, 25.8% reduction) and AD (1.91 ± 0.78 , $p < 0.001$, 25.5% reduction) groups, whereas those in the PIB (-) DLB/PDD group did not differ from the HC group (0.76 ± 0.60 , $p = 1.000$, 10.2% reduction). Furthermore, in the AD and PIB(+) DLB/PDD groups, significant grey matter volume reduction compared to controls was shown in frontal, parietal, occipital and lateral temporal cortices, striatum, hippocampus and amygdala; while there was no significant grey matter reduction in the PIB (-) DLB/PDD group.

Discussion

The present study demonstrated that DLB/PDD patients with high cortical PIB uptake had AD-like cortical atrophy in the parahippocampal area, lateral temporal and parietal cortices compared to the HC subjects. Furthermore, the DLB/PDD patients with high cortical PIB uptake showed parahippocampal atrophy similarly to the AD patients, as compared to the DLB/PDD patients with low cortical PIB uptake. These results suggest that A β deposition is associated with AD-like atrophy in DLB/PDD patients.

In previous reports, the patterns of cortical atrophy observed in

Table 2 Reduction of grey matter volumes; values were normalized by total intracranial volumes compared to controls *Mov Disord*, 28(2), 169-75, 2013.

	DLB/PDD		AD	
	PIB(-)	PIB(+)		
Frontal	1.65 ± 1.54	3.04 ± 1.52	2.60 ± 1.40	b; †; c; †
Sensorimotor	0.85 ± 1.15	1.42 ± 0.84	1.22 ± 1.05	
Parietal	1.34 ± 1.22	2.28 ± 0.40	2.08 ± 1.30	b, c; †
Striatum	1.22 ± 1.30	2.23 ± 1.60	2.14 ± 2.06	b; **; c; *
Occipital	1.18 ± 0.86	1.70 ± 1.02	1.94 ± 1.04	b; *; c; †
Lateral temporal	1.40 ± 0.93	2.81 ± 1.26	3.22 ± 1.24	a; *; b; c; †; d; **
Parahippocampal area	0.76 ± 0.50	1.94 ± 0.60	1.91 ± 0.78	b; c; †; d; e; * †
Hippocampus	0.66 ± 1.07	1.82 ± 0.94	2.21 ± 0.96	b, d; *; c; †
Amygdala	0.83 ± 1.43	2.67 ± 1.51	3.71 ± 1.59	b; **; c, d; †

Grey matter volume reduction compared to controls adjusted by each intracranial volume was expressed by Z score, and values are listed as mean \pm SD.

a: HC vs PIB(-) DLB/PDD; b: HC vs PIB(+) DLB/PDD; c: HC vs AD; d: PIB(-) DLB/PDD vs AD; e: PIB(-) DLB/PDD vs PIB(+) DLB/PDD, * $p < 0.05$, ** $p < 0.01$, † $p < 0.005$, ‡ $p < 0.001$ (ANCOVA, adjusting for differences in age, followed by Bonferroni correction)

DLB and PDD were controversial. The different results of previous studies could be explained by the difference in the prevalence of subjects with high cortical A β deposition.

A pathological study by Foster *et al.*^[1] reported that a high cortical A β score along with an older age at onset were associated with a shorter time-to-dementia period in PDD. Rowe *et al.*^[2] reported that cortical PIB-binding was correlated inversely with the interval from onset of cognitive impairment to diagnosis in DLB. Longitudinal studies in DLB/PDD patients will be required to elucidate whether A β deposition accelerates the progression of dementia and brain atrophy, and whether α -synuclein accelerates A β deposition in the brain.

It may perhaps be a more interesting finding in this study that there was no striking grey matter atrophy despite the presence of dementia in PIB (-) DLB/PDD patients. Graff-Radford *et al.*^[3] reported that patients with DLB but without the imaging features of coexistent AD-related pathology, such as parahippocampal atrophy and PIB(+), were more likely to cognitively improve with acetylcholinesterase (AChE) inhibitor treatment. These findings would suggest a predominant subcortical mechanism, such as cholinergic dysfunction, underlying the dementia in the beta-amyloid negative Lewy body patients with dementia.

In conclusion, our results suggest that A β deposition is associated with AD-like atrophy in DLB/PDD. Early intervention against A β may prevent or delay AD-like atrophy in patients with DLB/PDD with A β deposition.

References

- [1] Foster ER, Campbell MC, Burack MA, *et al.*: Amyloid imaging of Lewy body-associated disorders, *Mov Disord*, 25(15), 2516-2523, 2010.
- [2] Rowe CC, Ng S, Ackermann U, *et al.*: Imaging beta-amyloid burden in aging and dementia, *Neurology*, 68(20), 1718-1725, 2007.
- [3] Graff-Radford J, Boeve BF, Pedraza O, *et al.*: Imaging and acetylcholinesterase inhibitor response in dementia with Lewy bodies, *Brain*, 135(Pt 8), 2470-2477, 2012.

Research on Radiation Protection

Kazuo Sakai, Ph.D.

Director of Research Center for Radiation Protection

E-mail: kzsakai@nirs.go.jp

Overviews

The primary aim of the Research Center is to provide a scientific basis for radiation protection and safety. Toward this goal, radiation exposure from various sources is measured, the dose-effect relationships for various endpoints are examined, and the mechanisms underlying the effects are investigated. The Research Center disseminates its research results to promote public understanding of radiation effects and to encourage the enactment of more reasonable regulations concerning the use of radiation. The scope of its activities is not limited to Japan. It has been appointed a collaborating center by the International Atomic Energy Agency (Fig. 1).

The Research Center consists of the Planning and Operation Unit, three research programs (Radiobiology for Children's Health Program, Radiation Risk Reduction Research Program, and Regulatory Science Research Program) and one Research and Development Team; the activities in each of these are summarized below.

Planning and Operation Unit

In addition to management of the mid-term research plan, after the Fukushima Daiichi Nuclear Power Plant accident, the unit organized telephone consultations, which were carried out with the



help of members of other centers. The number of consultations has reached more than 18,000 (Fig.2). The Unit also organized a number of international and domestic meetings.

1) Regional Meeting on Occupational Radiation Protection in Emergency Exposure Situations (November 22-25, 2011)

This meeting was held in the framework of the TC (Technical Cooperation) Program and the RCA (Regional Co-operative Agreement for Research, Development and Training Related to Nuclear Science and Technology for Asia and the Pacific) of the IAEA. The meeting focused on subjects in the context of the Fukushima NPP accident. Thirty participants from 15 countries joined the meeting and discussed topics such as occupational exposure and protection under the emergency situation after the accident (Fig.3).



Fig.1 Designation of NIRS as an IAEA Collaborating Centre.

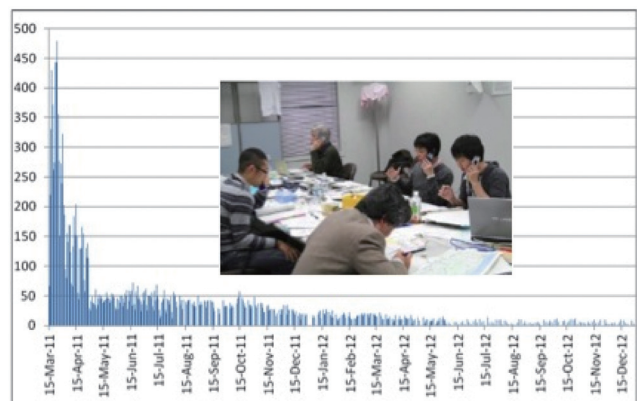


Fig.2 Trend in the number of telephone consultations (Total calls: 18,033 as of Dec. 31, 2012)

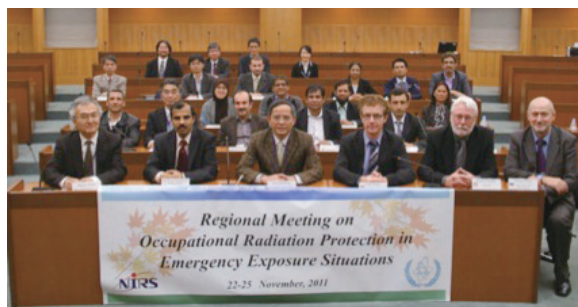


Fig.3 Participants in the RCA.



Fig.4 The ceremony to present certificates to two trainees on Dec. 21, 2012.

2) Research Center Symposium: One Year after the Fukushima Accident: Lessons Learned and Issues Forward from the Viewpoint of Radiation Protection Research (March 28, 2012)

One hundred and twenty participants joined this meeting and discussed the lessons learned and issues to be clarified in the aftermath of the Fukushima NPP accident, including low dose-rate radiation effects, effects on children, and effects of internal exposure.

3) Short-Term Training Course on Biological Dosimetry (December 10-21, 2012)

The Training Course was organized in co-operation with IAEA and co-organized by the Research Center for Emergency Medicine.

Two trainees from Indonesia and Vietnam participated in the course. The course covers the basics for chromosome aberration analysis, including dicentric analysis and FISH, as a measure of exposure. Upon completion of the course, the trainees understood calibration curves, were able to get trouble-shooting hints to obtain better metaphase images and to score dicentric chromosomes more properly for triaging and dose estimation, and they had practical knowledge and experience on using an automated microscopic image-analysis system for chromosome aberrations. On the last day of the training course, a ceremony was held and NIRS President Yonekura presented certificates to the two trainees (Fig.4).

4) NIRS International Symposium in collaboration with IAEA: Tackle the Challenges: Low Dose Radiation Effect on Human Body (December 21, 2012)

About 120 researchers participated in this symposium which was intended to give experts of related areas the latest scientific

findings about low dose radiation effects as determined by epidemiological surveys as well as by experiments using cells and animals. The experts shared their ideas with participants on the issues to be addressed in this field and the challenges related to the Fukushima accident were also discussed.

Invitations were extended to two experts from Europe, one from the US, three experts from Asia, four domestic experts, and the two trainees of the training course on biological dosimetry. Asian experts presented their findings on impacts of the Fukushima accident in their own countries; this was very useful for NIRS researchers to better know what kinds of information are needed in neighboring countries. A summary of IAEA activities related to Radiation Biology and Health Effects of Radiation was also presented.

Radiobiology for Children's Health Program

1) Objectives

In this era of low birthrate and prolonged longevity, concerns about the safety of fetuses and children have been growing. Progressive increases in the use of medical radiation for children have recently forced the ICRP, IAEA and WHO to draft global initiatives on radiation protection of children. In this program, we carry out studies to provide information on the risk of carcinogenesis due to radiation exposure, from single or repeated doses, during fetal and childhood periods, for which there is insufficient data. We study the effects of radiation exposure on cancer induction and lifespan shortening using animal models. The ultimate objectives of this research program are to propose age-weighting factors and relative biological effectiveness (RBE) of heavy ions and neutrons, for both fetuses and children. In addition, we are seeking to understand the effect of dose fractionation in children.

2) Life span shortening

Life span shortening was investigated in B6C3F1 mice of both genders exposed to gamma-rays (^{137}Cs), carbon ions (energy, 290 MeV/u; LET, 13 keV/um) and neutrons (1-2 MeV) at various ages from fetus to mature adult. For gamma-ray exposures, linear dose-response curves were obtained with a slope (% of life span loss per unit dose) of 9%/Gy for mice exposed to gamma-rays at 1 week of age. No gender difference was observed. For mice exposed at 7 weeks of age, the slope of the dose-response was reduced for males, i.e. 3%/Gy, whereas the slope was unchanged for females. In utero exposures had a negligible effect for both genders. Carbon ions and neutrons were more effective in reducing life span than gamma-rays, particularly when fetal and neonatal mice were exposed. These results suggest a larger relative biological effectiveness (RBE) of carbon ions and neutrons for fetuses and infants compared to adults.

3) Cancer induction

We have previously reported that there are susceptible age-windows for radiation carcinogenesis which are organ dependent. We have now demonstrated the age-windows for a range of organs. (1) Brain tumors: *Ptch1* heterozygous mice are a model for medulloblastoma in children with Gorlin syndrome. The perinatal period is the most susceptible for radiation-induced medulloblastoma, with decreasing sensitivity thereafter. (2) Renal cell carcinoma: Renal cell carcinoma in *Tsc2* heterozygous rats is also most efficiently induced by irradiation at the perinatal stage. (3) Hepatocellular carcinoma: B6C3F1 mice show the highest inci-

dence of liver tumors after irradiation at 1 week of age. (4) **Intestinal tumors**: the greatest incidence of intestinal tumors in *Apc^{Min/+}* mice was observed with irradiation at 1-2 weeks of age. (5) **Mammary cancers**: The incidence of mammary cancers developed by 80 months of age was larger for post-pubertal (7 weeks of age) than for pre-pubertal (3 weeks of age) irradiation. (See details in the Highlight) (6) **Lung tumors**: in contrast to other organs, the incidence of radiation-induced lung tumors does not increase as a function of age-at-exposure, consistent with the result seen for A-bomb survivors. In summary, most organs show radiation-sensitivity in juveniles, and the susceptible age-windows for radiation carcinogenesis vary by tissue.

In additional experiments, combined effects of chemical carcinogen and radiation during puberty were investigated. We established levels for radiation and ENU doses for risk assessment, as well as determined the importance of the order and timing of the exposures, as shown in the Highlight.

Radiation Risk Reduction Research Program

1) Aims of the program

Cancer susceptibility after exposure to radiation differs depending on individuals. Age and gender are known factors causing individual differences in radiation sensitivity. Smoking has also been identified to elevate the individual sensitivity to α -particles. In addition to these well-defined factors, there are other potential factors which have been suggested to modulate radiation sensitivity of individuals. First, variable efficiency of DNA repair resulting from single nucleotide polymorphisms (SNPs) located in genes for DNA repair-related proteins is thought to cause individual differences in radiation sensitivity. As non-homologous end joining (NHEJ) is the major mammalian system for repair of DNA double strand breaks, a genetic variation in NHEJ-related proteins is expected to have a strong correlation with radiation sensitivity of individuals. Second, there is evidence suggesting that individual radiation sensitivity is modulated by life styles; especially the calorie intake has been shown to have a significant impact on radiation carcinogenesis in laboratory animals.

In the last Mid-term Plan, we studied the mechanisms for an untargeted radiation carcinogenesis where tumors were induced in the thymus transplanted from unirradiated donor mice depending on radiation doses to which the host mice were exposed. We demonstrated that microenvironment could modulate cellular sensitivity to radiation carcinogenesis. In addition, we confirmed the functional involvement of NHEJ-related factors, such as XRCC4, Artemis, and MDC1, in cellular protection from radiation effects, and found that the activity of these factors may modify the radiation risks. Furthermore, we demonstrated a correlation between radioadaptive responses (low dose radiation-inducible resistance to subsequent high dose radiation) and elevated DNA repair efficiency. This finding suggested a possibility that individual radiation sensitivity may be artificially modulated by regulating radioadaptive responses.

Based on these accomplishments, we extended our research efforts in a new program in the current Mid-term Plan. The purpose of this program is to identify factors, whatever genetic and epigenetic, causing individual differences in radiation sensitivity, and also to present a possible way to reduce individual radiation risks by artificially regulating these factors.

2) Research teams in the program

There are two research teams in the program: Radiation Risk Modifier Research Team and Active Radiation Protection Research Team. The Radiation Risk Modifier Research Team is aiming at identification of lifestyle-related factors and protein markers which are usable to identify high radiation risk individuals. The Active Radiation Protection Research Team studies the mechanisms for biological responses to radiation, especially radioadaptive responses and DNA damage responses, to find a way to modulate individual radiation risks through manipulation of these responses.

3) Overview of accomplishments

We have identified some variants of non-homologous end joining (NHEJ)-related factors such as Ku70 and Ku80 having a point mutation in domains required for interaction with other molecules. These variant proteins are candidates for the protein markers for high radiation risk groups. And we also suggested a possibility that the mutagenic effects of radiation may be reduced by modulating the activity of another NHEJ-related factor, Artemis. This factor is a promising target to manipulate in order to reduce radiation risks. Furthermore, we could demonstrate a possible way to reduce radiation risks by combination of restriction of calorie intakes and radioadaptive responses.

4) Activities other than research (e.g. Fukushima Daiichi NPP accident related activities)

Within the framework of a human resources development program conducted by Kyoto University, we hold a training course for university students where they could learn about some of the newest and most exciting aspects of radiation biology. After the accident at the Fukushima NPP, we have actively contributed to easing the mental anxiety for residents in contaminated areas in Fukushima and Kanto by answering questions concerning health effects of radiation.

Regulatory Science Research Program

Aims of the program are to investigate necessary information for development of radiation safety standards and guidelines and to propose scientifically based measures for radiation regulation and policy aiming at a more reasonable system of radiation protection. The research of the program is focused on three subject areas.

1) Measures for regulation and optimization of exposures from natural radiation

The program carried out studies on evaluation of occupational and public exposures from natural radiation sources such as radon, NORM (naturally occurring radioactive materials), and cos-



Fig.5 Translated versions of IAEA reports.

mic ray exposure when flying in air craft. Regarding indoor radon exposure, the efficiency of mitigation methods using under-floor ventilation was investigated in a Japanese traditional wooden house. International comparison of radon measurements was carried out for their standardization. Occupational exposure due to utilization of NORM was studied to obtain the relationship between activity concentration of the materials and dose received by various workers, which is useful information to set the exemption criteria for the NORM level. The measurement system for cosmic rays in a facility on the top of Mt. Fuji was developed to evaluate the sudden increase of dose due to solar flares.

2) Policy for radiation regulation based on radiation risk

In order to propose a radiation protection policy with consideration of social rationality, the program has made a comprehensive analysis of epidemiological data using advanced statistics analysis and has also developed an effective method for risk communication. A tool for risk assessment using the latest risk information was developed to estimate radiation risk among a specified group of exposed people.

3) Measures for environmental protection

For the purpose of developing new standards for environmental protection against radiation exposure, analysis of transfer of radioactive materials to animals using a dynamic model was carried out. The results of the assessment showed higher activity concentration in a standard animal than that estimated by a model using a static value for the transfer factor.

4) Activities other than research

As activities other than research, members of the program have addressed considerable requests from regulatory bodies responsible for radiation protection of people against exposure to radioactive materials due to the Fukushima Daiichi NPP accident. Members of the program also have cooperated in activities of international organizations, especially UNSCEAR.

R & D Team for Biospheric Assessment for Waste Disposal

This team aims at providing environmental transfer parameters for radiation dose assessments from radionuclides released from radioactive waste disposal sites. To obtain suitable parameters for the Japanese biosphere, this team has been working in four study areas: (1) behavior of radionuclides in Japanese estuarine areas; (2) estimation of the behavior of the key radionuclides (C-14 and I-129) in transuranic (TRU) waste; (3) transfer of radon from soil to the air; and (4) development of estimation methods for environmental parameters. Some details of these study areas are listed below.

1) Behavior of radionuclides in Japanese estuarine areas

Radionuclides that can reach estuarine areas will be from river water; and thus their behaviors will be the same as those of stable elements. In this study, more than 40 stable elements in water, sediment and biota samples were analyzed. Estuarine water to biota concentration ratio (CR) of various elements for algae, molluscs, and crustaceans were calculated using these data. When the obtained geometric means of CRs were compared with the CRs recommended in IAEA Technical Report Series 422 for marine organisms, no big differences between them were found.

Sediment-seawater distribution coefficients (K_d s) were also obtained.

2) Estimation of the behavior of the key radionuclides (C-14 and I-129) in TRU waste

^{14}C , especially in low molecular weight organic forms (e.g. acetic acid, formic acid and formaldehyde) will affect dose estimation and thus it is necessary to understand their behaviors in soil and plant systems. Soil-soil solution distribution coefficients (K_d s) of acetic acid ($[1\text{-}^{14}\text{C}]$, $[2\text{-}^{14}\text{C}]$ and $[1,2\text{-}^{14}\text{C}]$), formic acid, and formaldehyde were obtained; it was found that radiocarbon in these forms is easily released as gas (mostly as $^{14}\text{CO}_2$) in Japanese agricultural soils. Probably because of the $^{14}\text{CO}_2$ gas generation, when soil-to-plant transfer (TF) of ^{14}C was studied using tracer experiments in a growth chamber, relatively higher values were found than expected from open field observations with a stable carbon isotope ratio.

3) Transfer of radon from soil to the air

Radon generation and discharge into the air from waste disposal sites is an issue for dose estimation. In order to understand the fate, radon exhalation rates in agricultural fields were investigated for various soil types widely observed in Japan. Also, tracer experiments with increasing water moisture contents in several types of soils were studied with a ventilation-type accumulation chamber for radon exhalation rate determination. Radon exhalation rates obtained in Fukuoka, Kochi and Hokkaido Prefectures were $6.6 \pm 3.8 \text{ mBq m}^{-2} \text{ s}^{-1}$, $12.1 \pm 24.4 \text{ mBq m}^{-2} \text{ s}^{-1}$ and $2.0 \pm 1.7 \text{ mBq m}^{-2} \text{ s}^{-1}$, respectively.

4) Development of estimation methods for environmental parameters

Some environmental parameters, such as TF, K_d and CR, for important radionuclides are sometimes difficult to obtain in situ. To estimate these values, empirical multiple regression models (Fig. 6) were developed using NIRS databases and generally available databases collected by this team; the databases included soil characteristics (pH, water content, size distribution, elemental concentrations), and elemental concentrations in crops, estuarine water and biota, etc. . Data related to the Fukushima Daiichi NPP accident were also collected for the models.

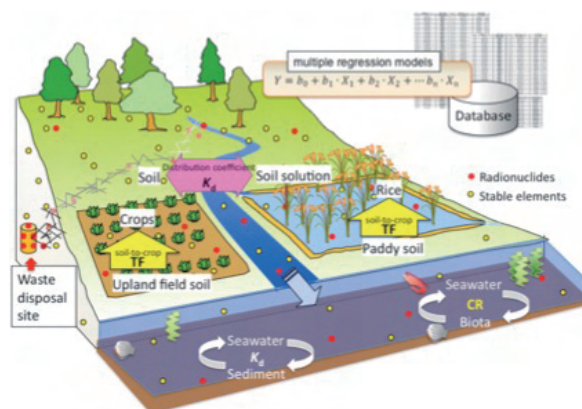


Fig.6 Environmental transfer parameters for radiation dose assessments from radionuclides released from radioactive waste disposal sites and application of multiple regression models to estimate parameters of radionuclides.

Highlight

Isotopic evidence of Pu release into the environment from the Fukushima nuclear accident

Jian Zheng

Email: jzheng@nirs.go.jp

Abstract

Here we report a study on the accurate determination of Pu isotopic composition in surface soil and litter. The results provide isotopic evidence for the release of Pu into the atmosphere and deposition on the ground in northwest and south of the Fukushima DNPP in the 20-30 km zones. The high activity ratio of $^{241}\text{Pu}/^{239+240}\text{Pu}$ (> 100) from the Fukushima DNPP accident highlights the need for long-term ^{241}Pu dose assessment, and the ingrowth of ^{241}Am .

Introduction

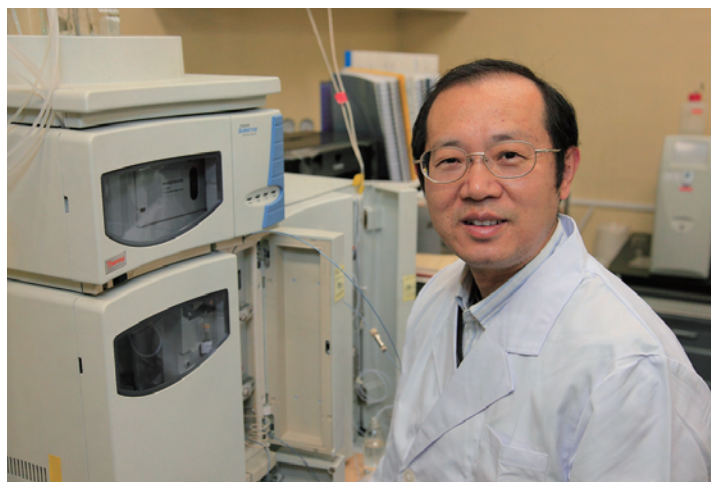
The Fukushima Daiichi nuclear power plant (DNPP) accident caused massive releases of radioactivity into the environment. The released highly volatile fission products, such as $^{129\text{m}}\text{Te}$, ^{131}I , ^{134}Cs , ^{136}Cs and ^{137}Cs were found to be widely distributed in Fukushima and its adjacent prefectures in eastern Japan. However, the release of non-volatile actinides, in particular, Pu isotopes remains uncertain more than half a year after the accident.

Experimental

We collected surface soil samples for the determination of activities of ^{137}Cs and Pu, and Pu atom ratios ($^{240}\text{Pu}/^{239}\text{Pu}$, $^{241}\text{Pu}/^{239}\text{Pu}$) in: Chiba, Kamagaya, and Mito Cities in the Kanto Plain; the Evacuation-Prepared Area (J-Village, 20 km south of Fukushima DNPP); and the Deliberate Evacuation Area (S1, in Katsurao Village, 25 km WNW of Fukushima DNPP; S2, in Namie Town, 26 km NW of Fukushima DNPP; and S3, in Iitate Village, 32 km NW of Fukushima DNPP) (Fig.1). The determination of Pu isotopes was done using a sector-field ICP-MS.

Results

For the samples collected in Fukushima Prefecture, activities of $^{239+240}\text{Pu}$ ranged from 0.019 to 1.400 mBq/g, within the typical global fallout $^{239+240}\text{Pu}$ activity range of 0.15 to 4.31 mBq/g observed in Japanese soils before the Fukushima DNPP accident. However, high activities of ^{241}Pu ranging from 4.52 to 34.8 mBq/g were detected in samples of the J-Village surface soil (0-2 cm) and of litter at sites S2 and S3. ^{241}Pu was released into the environment through atmospheric nuclear weapons tests in the last cen-



tury. Due to its short half-life of 14.4 years, the activity of ^{241}Pu in Japanese soils is quite low (ca. 1.2 for $^{241}\text{Pu}/^{239+240}\text{Pu}$ activity ratio, ^{241}Pu decay corrected to 15 March 2011). Therefore, the finding of high ^{241}Pu activities in these samples suggested an additional Pu input. The $^{240}\text{Pu}/^{239}\text{Pu}$ and $^{241}\text{Pu}/^{239}\text{Pu}$ atom ratios found in these samples ranged from 0.303 to 0.330 and from 0.103 to 0.135, respectively. They were significantly higher than those of global fallout and the atmospheric fallout deposition in Japan from 1963 to 1979, indicating new Pu input from the Fukushima DNPP accident. We noted that in the surface soil (0-1cm) under the litter layer at sites S3 and S2, no ^{241}Pu was determined and $^{240}\text{Pu}/^{239}\text{Pu}$ atom ratios were 0.144 and 0.177, respectively, close to the global fallout value. This phenomenon indicated that the released Pu deposited in the litter layer, had not reached the underlying surface soil by May 2011 when the samples were collected. We considered that the atom ratios of $^{240}\text{Pu}/^{239}\text{Pu}$ and $^{241}\text{Pu}/^{239}\text{Pu}$ found in the litter layer reflected the isotopic composition of the released Pu from the Fukushima DNPP accident. Compared to the Pu isotopic composition seen after the Chernobyl accident, the Fukushima accident Pu had a slightly higher $^{241}\text{Pu}/^{239}\text{Pu}$ atom ratio, but lower ratio of $^{240}\text{Pu}/^{239}\text{Pu}$ (Fig.2).

The atom ratios of $^{240}\text{Pu}/^{239}\text{Pu}$ and $^{241}\text{Pu}/^{239}\text{Pu}$ found in the surface soil of J-Village were slightly lower than those in litter samples in Namie Town (S2) and Iitate Village (S3) in the NW direction of the Fukushima DNPP. The plot of $^{241}\text{Pu}/^{239}\text{Pu}$ vs. $^{240}\text{Pu}/^{239}\text{Pu}$ for the global fallout, the soil in J-Village and the litter at sites S2 and S3 could be described by a linear function ($r^2=0.9901$): $^{241}\text{Pu}/^{239}\text{Pu} = 0.9024 \times (^{240}\text{Pu}/^{239}\text{Pu}) - 0.1656$ (Fig. 2). This indicated that the Pu in J-Village surface soil (0-2 cm) contained a small proportion of global fallout Pu. Using a two end-member mixing model we found the percentage of Fukushima-derived $^{239+240}\text{Pu}$ in the J-Village soil was 87 %; and the other 13 % $^{239+240}\text{Pu}$ was of global

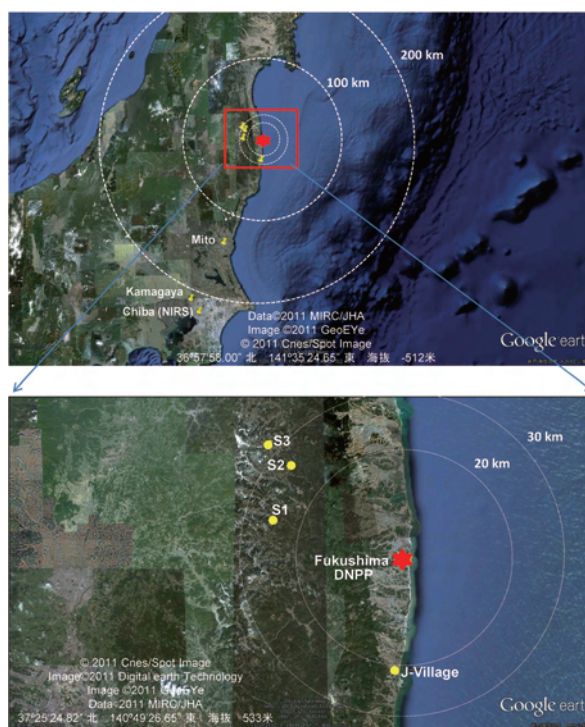


Fig.1 Map showing the locations of soil sampling sites^[1].

fallout origin. We noted that Pu activities in the J-Village surface soil were ca. one order of magnitude lower than those northwest of Fukushima DNPP.

In the samples that showed Pu contamination from the Fukushima accident, we detected extremely high ^{137}Cs activities. They ranged from 1.15×10^4 to 4.65×10^6 mBq/g. The activity ratios of $^{137}\text{Cs}/^{239+240}\text{Pu}$ for these samples ranged from 1.95×10^5 to 2.53×10^7 , and they were several orders of magnitude higher than that of the Chernobyl accident (770, ^{137}Cs corrected for decay to June 1997), indicating that the release of $^{239+240}\text{Pu}$ from the Fukushima DNPP accident was very small.

In this study, the $^{241}\text{Pu}/^{239+240}\text{Pu}$ activity ratio of the Fukushima-derived Pu was found to be higher than 100. The additional dose contribution from ^{241}Pu has to be estimated. As an example, assuming a similar contamination of ^{241}Pu in the surface soil as that in the litter layer and using the method of IAEA-TECDOC-955, we estimated the ^{241}Pu dose for a person living for 50 years in the vicinity of S2 site to be 0.44 mSv, about 4 times the $^{239+240}\text{Pu}$ dose estimated by the MEXT.

^{241}Pu is a beta-emitting isotope, as a result of ^{241}Pu decay the increase of ^{241}Am may significantly enhance the alpha-activity level in the contaminated area for a certain period of time. We made a prognostic predication on the ingrowth of ^{241}Am ^[1]. The result showed that the $^{241}\text{Am}/^{239+240}\text{Pu}$ activity ratio would increase quickly to reach a maximum value of 3.12 in the year 2081, followed by a gradual decrease. This predicated maximum value of 3.12 is almost one order of magnitude higher than that of the expected global fallout $^{241}\text{Am}/^{239+240}\text{Pu}$ in the year 2042. Furthermore, the increased amount of ^{241}Am may remain in the surface soil for decades together with Pu isotopes, as demonstrated in our previous study on the downward migration of ^{241}Am and Pu released from the atomic bomb detonation in Nishiyama area, Nagasaki, Japan^[2]. Therefore, it is highly necessary to investigate the distribution and surface activity of ^{241}Pu inside the 20 km zone, where much higher ^{241}Pu could be expected. This is important for the

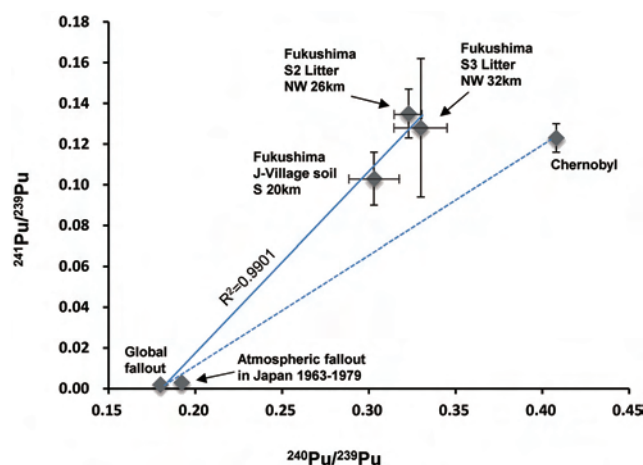


Fig.2 Mixing plot of $^{241}\text{Pu}/^{239}\text{Pu}$ atom ratio vs. $^{240}\text{Pu}/^{239}\text{Pu}$ atom ratio for litter and surface soil samples collected in the 20-30 km zones around the Fukushima daiichi Nuclear Power Plant, Japan, and a comparison of isotopic composition with those of the Chernobyl accident and the global fallout sources^[1].

long-term dose assessment of actinides contamination.

For soil samples collected in Mito, Chiba, and Kamagaya Cities, although ^{137}Cs activities were significantly higher than the activity level before the accident, the $^{239+240}\text{Pu}$ activities and $^{240}\text{Pu}/^{239}\text{Pu}$ atom ratios were typical values of global fallout and no ^{241}Pu could be detected. We concluded that the Fukushima source contribution to the total Pu activity was negligible.

References

- [1] Zheng J, Tagami K, Watanabe Y, *et al.*: Isotopic evidence of plutonium release into the environment from the Fukushima DNPP accident, *Sci Rep*, 2: 304, doi:10.1038/srep00304, 2012.
- [2] Zheng J, Yoshida S, Yamada M, *et al.*: Current status of ^{241}Am in Nishiyama soil: six decades after Nagasaki A-bomb explosion. *Proceedings of the Tenth Workshop on Environmental Radioactivity*. 2009-8, 39-44 (2009).

Highlight

Monitoring of radioactive fallout at National Institute of Radiological Sciences

Nobuyoshi Ishii

E-mail: nobu@nirs.go.jp

Abstract

Fallout from the disaster at TEPCO's Fukushima Daiichi Nuclear Power Plant (FDNPP) has been monitored at NIRS, located about 220 km south-southwest of the FDNPP. Sampling was started from 15 March 2011, 2-3 times a day for the first 10 days and then once a day until 22 April 2011. Gamma-ray spectrometry of fallout deposition samples revealed the presence of ^{131}I , ^{132}I , ^{132}Te , ^{134}Cs and ^{137}Cs . The largest deposition was observed during 7:00-16:00, on 21 March. The estimated total deposition densities at NIRS were $1.40 \times 10^5 \text{ Bq/m}^2$ for ^{131}I , $4.12 \times 10^4 \text{ Bq/m}^2$ for ^{132}Te , $1.45 \times 10^4 \text{ Bq/m}^2$ for ^{134}Cs , and $1.48 \times 10^4 \text{ Bq/m}^2$ for ^{137}Cs (corrected to 11 March 2011). The obtained densities of ^{134}Cs and ^{137}Cs were also supported by the accumulated amount of ^{134}Cs and ^{137}Cs in soil near the deposition sampling site.

Introduction

The Fukushima Daiichi Nuclear Power Plant (FDNPP) suffered severe damage from an earthquake of magnitude 9.0 and the subsequent huge tsunami on 11 March 2011. In the following days, large release of radionuclides occurred from the plant. According to estimates from the former Nuclear and Industrial Safety Agency (NISA), the released ^{131}I was $1.6 \times 10^{17} \text{ Bq}$ and $1.5 \times 10^{16} \text{ Bq}$ for ^{137}Cs . For comparison, $1.76 \times 10^{18} \text{ Bq}$ of ^{131}I was released by the Chernobyl nuclear power plant accident.

Environmental radioactivity levels in the Kanto Plain have become of growing concern to the public. Quantitative data and isotope ratios of different radionuclides for the fallout deposition, however, have been limited, although such data may provide useful information for the estimation of public exposure dose and the emission inventory of radionuclides. In this annual report, we present initial results of measured fallout deposition at the National Institute of Radiological Sciences (NIRS), located about 220 km south-southwest from the FDNPP. Details of this investigation were reported by Ishii et al.^[1]

Material and methods

Fallout deposition samples were collected on the roof of a five-story building at NIRS (Fig. 1). The sampling periods are listed in



Table 1. A total of 52 samples were collected during the investigation period. Two stainless steel containers, each with a 0.2 m^2 of surface area, were placed at a height of 20 cm above the roof surface. These containers included at least 300 mL of 1% tetramethyl ammonium hydroxide (TMAH; super-pure grade, vol to vol), which prevents iodine losses through volatilization. At the end of each sampling, 100 mL of the sample was transferred into a 250 mL polypropylene container for gamma-ray spectrometry.

The total deposition of ^{137}Cs was also estimated using soil in flowerpots ($n = 3$), which were placed on a building roof near the fallout deposition sampling site from 11 March to 19 May 2011. The soil sample was dried and well mixed to make a homogeneous radioactive cesium concentration at the end of the experiment (19 May 2011) and transferred into a U8 polystyrene container for gamma-ray spectrometry. This estimation was carried out to ensure reliability of our investigation for fallout deposition at the rooftop.

The gamma-ray spectrometry was done using germanium detectors (Seiko EG&G). The measurement values were corrected to 15:27 on 11 March, when the first tsunami struck the FDNPP.

Results and discussion

Fallout deposition samples contained ^{131}I , ^{132}I , ^{132}Te , ^{134}Cs , and ^{137}Cs . In this annual report, results of ^{131}I and ^{137}Cs are described. Figure 2 shows the fallout deposition rates per unit area ($\text{Bq/m}^2/\text{h}$), obtained by dividing deposition densities (Bq/m^2) by collection time (h). A small peak of the fallout deposition rate per unit area for ^{131}I was observed at sampling #3 (from 7:30 to 13:20 on 6 March,). The rate, however, decreased from $3.6 \times 10^2 \text{ Bq/m}^2/\text{h}$ at sampling #3 to $3.1 \text{ Bq/m}^2/\text{h}$ at sampling #8. The maximum rate of

Table 1 Beginning time and ending time of sampling at NIRS

Number of sampling	Beginning time	Ending time	Number of sampling	Beginning time	Ending time	Number of sampling	Beginning time	Ending time	Number of sampling	Beginning time	Ending time
1	3/15 13:25	3/15 16:50	14	3/20 7:00	3/20 16:00	27	3/27 9:00	3/28 9:00	40	4/9 9:00	4/10 9:00
2	3/15 17:00	3/16 7:30	15	3/20 16:00	3/21 7:00	28	3/28 9:00	3/29 9:00	41	4/10 9:00	4/11 9:00
3	3/16 7:30	3/16 13:20	16	3/21 7:00	3/21 16:00	29	3/29 9:00	3/30 9:00	42	4/11 9:00	4/12 9:00
4	3/16 13:30	3/16 17:00	17	3/21 16:00	3/22 7:00	30	3/30 9:00	3/31 9:00	43	4/12 9:00	4/13 9:00
5	3/16 17:00	3/17 7:00	18	3/22 7:00	3/22 16:00	31	3/31 9:00	4/1 9:00	44	4/13 9:00	4/14 9:00
6	3/17 7:00	3/17 12:00	19	3/22 16:00	3/23 7:00	32	4/1 9:00	4/2 9:00	45	4/14 9:00	4/15 9:00
7	3/17 12:00	3/17 17:00	20	3/23 7:00	3/23 16:00	33	4/2 9:00	4/3 9:00	46	4/15 9:00	4/16 9:00
8	3/17 17:00	3/18 7:00	21	3/23 16:00	3/24 7:00	34	4/3 9:00	4/4 9:00	47	4/16 9:00	4/17 9:00
9	3/18 7:00	3/18 12:00	22	3/24 7:00	3/24 16:00	35	4/4 9:00	4/5 9:00	48	4/17 9:00	4/18 9:00
10	3/18 12:00	3/18 17:00	23	3/24 16:00	3/25 7:00	36	4/5 9:00	4/6 9:00	49	4/18 9:00	4/19 9:00
11	3/18 17:00	3/19 7:00	24	3/25 7:00	3/25 16:00	37	4/6 9:00	4/7 9:00	50	4/19 9:00	4/20 9:00
12	3/19 7:00	3/19 16:00	25	3/25 16:00	3/26 9:00	38	4/7 9:00	4/8 9:00	51	4/20 9:00	4/21 9:00
13	3/19 16:00	3/20 7:00	26	3/26 9:00	3/27 9:00	39	4/8 9:00	4/9 9:00	52	4/21 9:00	4/22 9:00

7.0×10^3 Bq/m²/h was observed at sampling #16, and the rate gradually decreased to 0.9 Bq/m²/h at the end of our investigation. No rainfall was observed at Chiba City until 16 March, and thus dry deposition was the main mechanism during this period for this radionuclide. The importance of dry deposition of ¹³¹I was also reported for the Chernobyl accident of 1986.

The largest deposition event at NIRS started from 21 March. From 7:00 to 16:00 that day, the deposition rates were 7.0×10^3 Bq/m²/h for ¹³¹I and 1.4×10^3 Bq/m²/h for ¹³⁷Cs. These significant in-



Fig.1 Sampling site of fallout deposition at NIRS^[2].

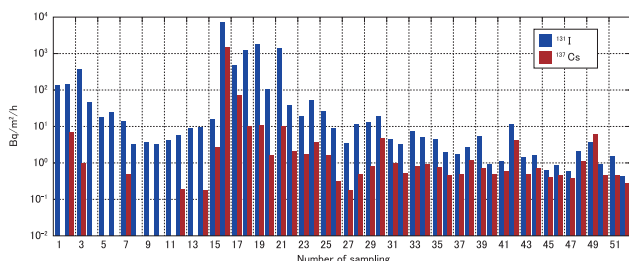


Fig.2 Fallout deposition of ¹³¹I and ¹³⁷Cs during our investigation periods^[2].

creases in fallout deposition rates could be related to rainfall. This was the first rainy day around the Kanto Plain after the large release of radionuclides from the FDNPP on 15 and 16 March, and the rainfall continued for 3 days. The results show that wet deposition was the main pathway for fallout deposition of these radionuclides to the ground during the investigation periods.

Fallout deposition was also monitored at the Japan Chemical Analysis Center (JCAC) and the Chiba Prefectural Environmental Research Center (CPERC) in addition to NIRS within the prefecture. Both centers are located within 15 km from NIRS. Then, the fallout deposition densities were compared among those sites using the data from 18 March to 22 April, because the monitoring of fallout deposition at CPERC began from 18 March and ended 22 April at NIRS. The total deposition densities were 4.7×10^3 Bq/m² at JCAC, 4.9×10^3 Bq/m² at CPERC, and 1.5×10^4 Bq/m² at NIRS. One reason for the differences in the total deposition densities may be rainfall intercepting the plume. When we sampled the fallout deposition at 9:00 on 21 March, it was raining heavily, but no rainfall was recorded at the CPERC sampling site at that time.

To ensure reliability of the fallout deposition densities at NIRS, the total amount of radioactive cesium in the soils of some flowerpots were also measured, and the densities were estimated as $1.4 \times 10^4 \pm 2.5 \times 10^3$ Bq/m² (corrected to 11 March 2011). These estimated densities from the soil were only slightly less than the total deposition densities at NIRS. Our estimation of fallout deposition densities gave no indication of a three-fold overestimation. The loss may be due to leakage of radioactive cesium through the interspace between the soil and the wall of the flowerpot when it was raining and blowing away of small soil particles contaminated with radioactive cesium under dry conditions.

References

[1] Ishii N, Tagami K, Takata H, *et al.*: Deposition in Chiba Prefecture, Japan, of Fukushima Daiichi Nuclear Power Plant Fallout, *Health Phys*, 104, 189-194, 2013.
 [2] Ishii N, Tagami K, Uchida S.: Environmental radioactivity levels at NIRS after TEPCO Fukushima Daiichi Nuclear Power Plant accident, KUR Report of the Research Reactor Institute of Kyoto University, KURRI-KR-170, 5-10, 2012.

Highlight

Age-dependent relative biological effectiveness of carbon ion radiation for rat mammary carcinogenesis

Tatsuhiko Imaoka, Mayumi Nishimura,
Kazuhiro Daino, Toshiaki Kokubo, Kazutaka Doi,
Daisuke Iizuka, Yukiko Nishimura,
Tomomi Okutani, Masaru Takabatake,
Shizuko Kakinuma, Yoshiya Shimada
E-mail: t_imaoka@nirs.go.jp

Introduction

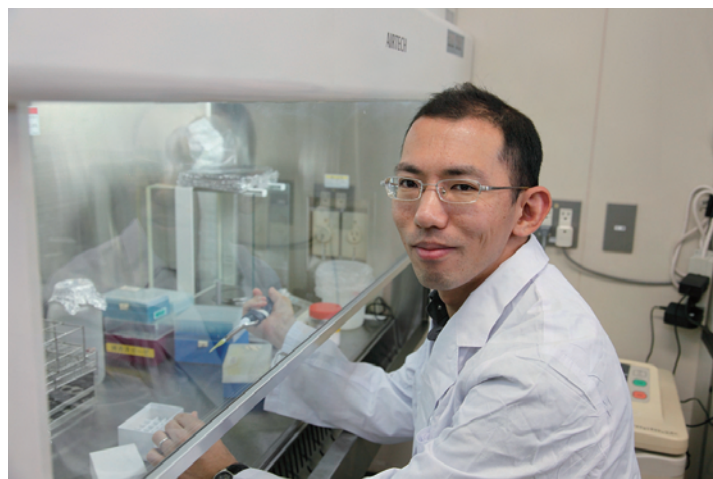
Heavy ion radiotherapy using HIMAC continues to improve cancer treatment by permitting accurate dose localization and strong biological effects attributed to the sharp Bragg peak and high linear energy transfer (LET). Because Bragg peaks are normally too narrow for therapeutic applications, spread-out Bragg peaks (SOBP) have been devised to obtain a broad and uniform dose distribution. Fractionated irradiation with a beam with a 6-cm SOBP, which is possible from 290-MeV/u carbon ions and has an LET range of 40-90 keV/ μm within the SOBP component, has been used to treat several cancer types.

There is increasing concern that medical radiation exposure can increase the risk of cancer, especially in children. Breast tissue is susceptible to radiation-induced carcinogenesis, and epidemiological studies have suggested a high risk of breast cancer after radiation exposure during childhood. Carbon-ion radiotherapy is currently not applied for the treatment of childhood cancers, partly because of the potential risk of promoting secondary cancer. We previously reported a high relative biological effectiveness (RBE) for the induction of mammary carcinogenesis in rats irradiated with a 6-cm SOBP carbon-ion beam at early adulthood (7 weeks)^[1]. As the mammary gland is one of the organs irradiated during radiotherapy for tumors in the chest area, it is likely that healthy mammary tissue will be exposed to the relatively low-LET (13 keV/ μm) component of the carbon-ion beam. Nevertheless, there is no published information from studies conducted in humans or using animal models about the risk of carcinogenesis following carbon-ion irradiation, whether fractionated or single, during childhood.

Apart from clinical issues, evidence suggests high susceptibility of the fetus to radiogenic cancer. In the present program, we used a common rat model of mammary carcinogenesis to investigate the effects of irradiation with 13 keV/ μm carbon ions on rats of various ages in comparison with rats irradiated with γ rays. The study has been published in the *International Journal of Radiation Oncology Biology Physics*^[2].

Results

1) Age window of susceptibility



Female Sprague-Dawley rats at various ages (embryonic days 3, 13 and 17, and 1, 3, 7 and 15 weeks after birth) were irradiated with ^{137}Cs γ rays or 290 MeV/u carbon ions (with an LET of 13 keV/ μm) at 0.2, 0.5, 1.0 and 2.0 Gy. A group of non-irradiated rats was subjected to the same analysis to enable comparison. All rats were observed weekly for development of palpable mammary tumors until 90 weeks of age (or earlier if general deterioration of an animal required that it be euthanized), after which the animals were euthanized. Excised mammary tumors were analyzed histologically and classified as either adenocarcinoma or benign tumors, such as adenoma and fibroadenoma. The hazard ratio for the development of palpable carcinoma in 1.0-Gy-irradiated groups was calculated based on using Cox's proportional hazard model (Fig. 1). Herein, γ irradiation at 1 week of age and carbon-

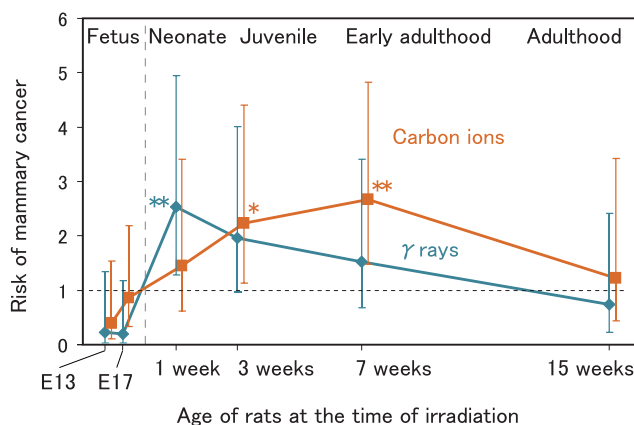


Fig. 1 Risk of mammary carcinoma in rats irradiated with 1 Gy of γ rays or carbon ions at various ages. Mean and 95% confidence interval of hazard ratios. E, embryonic day. *, $P < 0.05$; **, $P < 0.01$.

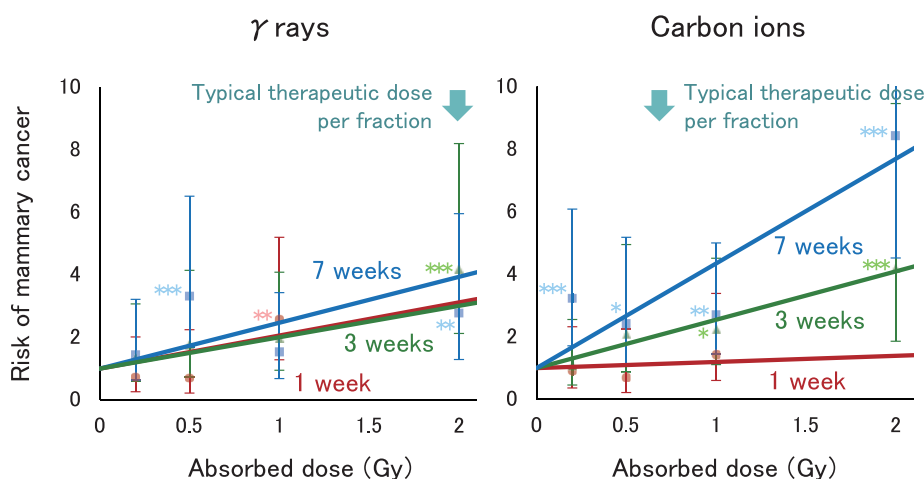


Fig.2 Dose-effect relationship for risk of mammary carcinoma induction in rats irradiated with γ rays or carbon ions at neonatal, juvenile and early adulthood stages. Mean and 95% confidence interval of hazard ratios. *, $P < 0.05$; **, $P < 0.01$; ***, $P < 0.001$.

ion irradiation at 3 and 7 weeks of age significantly increased the risk of carcinogenesis. Thus, for rats, the period of susceptibility to radiation-induced mammary carcinogenesis lies between 1-7 weeks after birth, with minimal susceptibility following irradiation during either the embryonic or full-adulthood stage.

2) Dose-effect relationship

Dose-effect relationships were then analyzed for experiments involving irradiation with γ rays or carbon ions at 1, 3 and 7 weeks after birth. The highest dose (2.0 Gy) of radiation at 1 week of age was excluded from this analysis because premature cessation of the estrous cycle was induced in these rats (data not shown). In this analysis, plotting of hazard ratios against dose indicated similar effects of γ irradiation among the groups of rats irradiated between 1-7 weeks after birth (Fig. 2). In contrast, the effect of carbon ions was greater for animals irradiated at later stages of development.

3) RBE values

We first calculated the value of ERR (Gy^{-1}) for each combination of radiation and age, as defined by the increase in the hazard ratio with unit dose (Table 1). The ERR values of the γ -ray groups fell within close proximity, having mutually overlapping 95% confidence intervals. Therefore, we combined these γ -ray groups to form a new set of dose-effect relationship data to obtain a better estimation of ERR for γ rays (Table 1, bottom row); as mentioned above, data of 2.0 Gy irradiation at 1 week of age were excluded. The RBE values for carbon-ion irradiation were calculated as the ratio of ERR for carbon ions to ERR for the combined γ -ray data as a reference, giving the values 0.2, 1.3, and 2.8, respectively (Table 1, rightmost column). Thus, the data suggested lower RBE values for mammary cancer risk from carbon-ion irradiation of neonatal and juvenile rats compared with that of young adult rats.

Clinical implications

Use of carbon ions for thoracic tumors of children (e.g., osteosarcomas and chordoma) would result in exposure of the mammary tissue to doses and LET commensurate with the experimental situation used here (~ 1.5 Gy/fraction, ~ 13 keV/ μm). Irradiation of other areas will result in exposure to very low radiation doses from scattered beams^[3], which were not tested in these experiments. The absorbed dose from carbon ions to the normal tis-

Table 1 Excess relative risk (ERR) per Gy and RBE (mean and 95% confidence interval) of carbon ions for rat mammary carcinogenesis.

Age at exposure	ERR (Gy^{-1})		RBE
	γ rays	Carbon ions	
1 week	1.1 [−0.3, 2.4]	0.2 [−0.4, 0.8]	0.2 [−0.3, 0.7]
3 weeks	1.5 [1.2, 1.7]	1.5 [1.3, 1.8]	1.3 [1.0, 1.6]
7 weeks	1.0 [0.1, 1.9]	3.3 [2.2, 4.5]	2.8 [1.8, 3.9]
All ages combined	1.2 [1.0, 1.3]	—	—

sue is generally less than one-third of that used in photon radiotherapies because of the high biological effect and improved dose localization (Fig. 2, arrows); therefore, even for the highest RBE postulated in our study (i.e., 2.8), the expected cancer risk would be lower than that anticipated for photon radiotherapies. Our findings imply that carbon-ion therapy may be associated with a risk of secondary breast cancer in humans, the extent of which may depend on the age of the patient at the time of irradiation.

References

- [1] Imaoka T, Nishimura M, Kakinuma S, *et al.*: High relative biologic effectiveness of carbon ion radiation on induction of rat mammary carcinoma and its lack of H-ras and Tp53 mutations, *Int J Radiat Oncol Biol Phys*, 69, 194-203, 2007.
- [2] Imaoka T, Nishimura M, Daino K, *et al.*: Influence of age on the relative biological effectiveness of carbon ion radiation for induction of rat mammary carcinoma, *Int J Radiat Oncol Biol Phys*, 85, 1134-1140, 2013.
- [3] Yonai S, Matsufuji N, Namba M.: Calculation of out-of-field dose distribution in carbon-ion radiotherapy by Monte Carlo simulation, *Med Phys*, 39, 5028-5039, 2012.

Highlight

Combined exposure to X-irradiation and *N*-ethyl-*N*-nitrosourea treatment alters the frequency and spectrum of *Ikaros* point mutations in murine T-cell lymphoma

Shizuko Kakinuma

E-mail: skakinum@nirs.go.jp

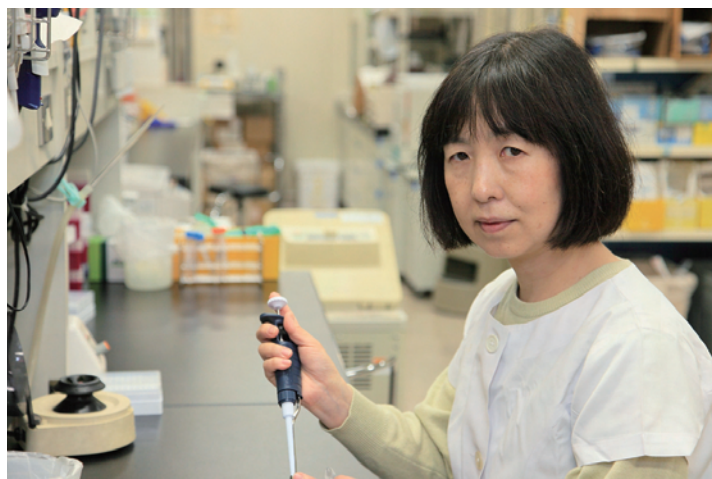
Introduction

Children are considered to be more sensitive to both radiation and carcinogenic chemicals as compared with adults because: (i) children's tissues are growing rapidly; and (ii) children have a longer life expectancy. As highlighted by the Fukushima nuclear power plant accident, cancer risk from radiation exposure to children is one of the central concerns for radiation protection.

The fact that individual carcinogens induce specific mutations in cancer-related genes contributes to researchers' understanding of the molecular pathways and mechanisms underlying cancer development. The major cause of human cancer is natural and man-made carcinogens in food and the environment; therefore, tumor induction by radiation exposure should always be considered in the context of the possible contributions from other environmental factors. For example, the combined effect of radiation exposure and smoking among atomic bomb survivors is additive, whereas that of exposure to radon progeny and smoking on lung cancer in underground miners is sub-multiplicative. The risk of the combined effect of radiotherapy and chemotherapy for Hodgkin's disease is additive, but the effects of radiotherapy and smoking are synergistic.

We used two genotoxic carcinogens, X-rays and *N*-ethyl-*N*-nitrosourea (ENU), to probe the mechanism of carcinogenesis caused by the combination of two distinct agents. X-rays cause double- or single-strand breaks in DNA, which can result in deletions or recombination, while ENU forms DNA adducts that can generate point mutations. Thus, it would be expected that the two carcinogens would each produce a different mutation spectrum. Indeed, we previously demonstrated that high-dose X-ray- and ENU-induced lymphomas each harbored a distinct mutation spectrum of the gene *Ikaros*, which encodes a transcription factor that plays a key role in lineage commitment and differentiation in lymphoid cells, and is also a tumor suppressor in acute lymphoblastic leukemia.

In this research highlight, we describe determination of the mode and mechanism of the carcinogenic effect of radiation combined with ENU, focusing on the dose-dependent effects of both carcinogens. In addition, we detail our comparison of the mutation spectrum of *Ikaros* in lymphomas induced by both agents with



those induced by treatment with X-rays or ENU alone.

Results

1) Combined exposure with X-rays followed by ENU shows both synergistic and antagonistic effects but simultaneous exposure to both carcinogens shows only a synergistic effect

We studied the mode and mechanism of the carcinogenic effect of radiation in combination with ENU. Induction of T-cell lymphomas by X-ray irradiation or ENU treatment showed thresholds at 0.4 Gy or 100 ppm, respectively. For combined exposures (X-ray→ENU), 4-week-old B6C3F1 female mice were irradiated with X-rays for 4 consecutive weeks (Kaplan's method) followed by 4 weeks of ENU treatment (Fig. 1A). For simultaneous exposures (X-rays+ENU), the mice were irradiated with X-rays by the same method while being treated with ENU from 4 weeks of age. To clarify the combined effect, doses of X-rays (0, 0.2, 0.4, 0.8, or 1.0 Gy per fraction) and ENU (0, 50, 100, or 200 ppm) were selected,

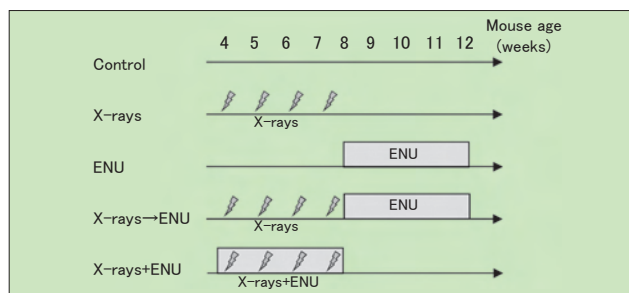


Fig. 1 Experimental protocol for combined exposure to X-rays followed by ENU (X-rays→ENU) and simultaneous exposure of X-rays and ENU (X-rays+ENU). Mice were exposed to X-rays every week (lightning bolts) starting at age of 4 weeks. ENU treatment was started at age 4 or 8 weeks.

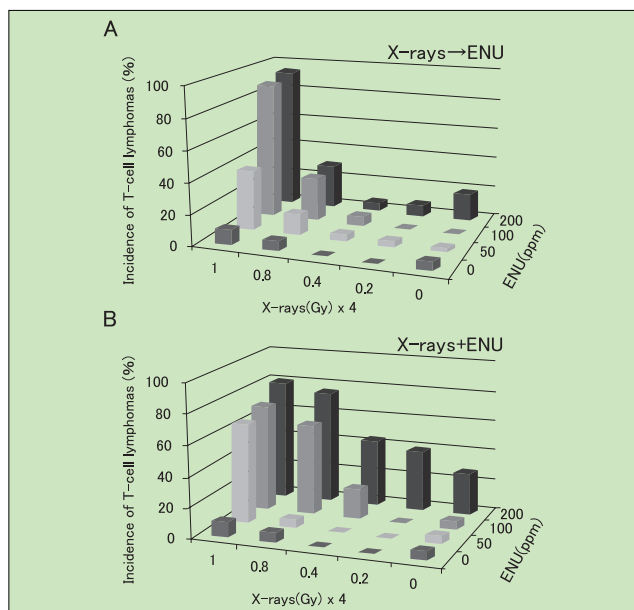


Fig. 2 Incidence of T-cell lymphoma (TL) induction by combined exposure to X-rays followed by ENU (X-rays→ENU) (A) and simultaneous exposure of X-rays and ENU (X-rays+ENU) (B).

centered on the threshold doses for T-cell lymphoma induction (0.4 Gy and 100 ppm, respectively). B6C3F1 mice exposed to X-rays→ENU developed T-cell lymphomas in a dose-dependent manner. Radiation doses above an apparent threshold acted synergistically with ENU to promote lymphoma development, whereas radiation doses below that threshold antagonized ENU-induced lymphoma development (Fig. 2A). For mice exposed simultaneously to X-rays+ENU, radiation doses above an apparent threshold showed a synergistic effect, but lower doses did not show any antagonistic effect (Fig. 2B). Interestingly, the combination of doses below the threshold for both carcinogens, i.e. the combination of 0.2 or 0.4 Gy of X-rays with 50 or 100 ppm of ENU, did not induce T-cell lymphomas, except for simultaneous exposure to 0.4 Gy X-rays and 100 ppm ENU.

2) Combined exposure alters the frequency of loss of heterozygosity (LOH) on chromosome 11 in lymphomas

We next investigated carcinogen-associated molecular changes to delineate the carcinogenic pathways activated by combined exposure. We previously reported that frequent LOH on chromosome 11 is characteristic of lymphomas induced by X-rays (1.6 Gy per fraction) but that LOH is rarely observed in spontaneous or ENU-induced lymphomas^[1]. The frequency of LOH at the *Ikaros* locus was significantly lower in ENU-induced, X-ray→ENU-induced, and X-rays+ENU-induced lymphomas (22%, $P < 0.001$; 17%, $P < 0.001$; 23%, $P < 0.001$, respectively; Chi-square test), compared with X-ray-induced lymphomas (51%) (Fig. 2). Thus, the pathway associated with *Ikaros* LOH was significant for X-ray-induced lymphomagenesis, but not for ENU, X-ray→ENU or X-rays+ENU exposures.

3) Combined exposure changes the proportion of *Ikaros* alteration types

Various types of *Ikaros* mutations have been reported in both human and mouse lymphomas. Therefore, we identified *Ikaros* alterations by analyzing mRNA and protein expression, and by sequencing the gene of lymphomas to distinguish differences be-

tween lymphoma-inducing treatments. Four types of *Ikaros* alteration (point mutation, insertion or deletion, null expression, and altered splicing) were observed in X-ray-induced lymphomas, and the proportions of these alterations differed among the lymphomas induced by combined exposure. The X-ray→ENU-induced and X-rays+ENU-induced lymphomas most frequently exhibited *Ikaros* point mutations, in the former accompanied by LOH at low frequency (18%), and in the latter accompanied by LOH more frequently (40%). The results suggest that X-ray→ENU exposure activated an ENU-induced mutagenic pathway, but X-rays+ENU exposure activated both radiation and ENU-induced pathways.

4) Combined exposure changes the distribution and frequency of base substitutions in *Ikaros*

We further analyzed the frequency and spectrum of *Ikaros* base substitutions in the lymphomas in detail. X-ray-induced lymphomas harbored G:C to A:T substitutions at CpG sites, and A:T to G:C substitutions; while ENU-induced lymphomas showed mainly A:T to G:C substitutions. In X-ray→ENU-induced lymphomas, four types of base substitutions (G:C to A:T at non-CpG, A:T to G:C, G:C to T:A, and A:T to T:A) were frequently observed. In contrast, X-ray+ENU-induced lymphomas showed only G:C to A:T at non-CpG sites, and A:T to G:C substitutions. These data suggest that G:C to A:T at non-CpG substitutions were associated with both combined exposure, while the G:C to T:A, and A:T to T:A substitutions were uniquely associated with X-ray→ENU exposure. Base substitution in the lymphomas was altered by the order of exposure to the two carcinogens.

Summary

In this study, we determined the mode and mechanism of the carcinogenic effect of radiation and ENU treatment, focusing on dose-dependent effects of both carcinogens. [2, 3] We found both dose-dependent synergistic and antagonistic effects of X-ray→ENU exposure on T-cell lymphomagenesis, but only the synergistic effect of X-rays+ENU exposure. In addition, The X-ray→ENU- and X-rays+ENU-induced lymphomas predominantly harbored *Ikaros* point mutations. The data on point mutation and LOH status suggest that X-rays→ENU-induced lymphomas activated an ENU-induced mutagenic pathway, but X-rays+ENU-induced lymphomas activated both X-ray- and ENU-induced mutagenic pathways. These data highlight the importance of the radiation and ENU doses for risk assessment, as well as the order and timing of the exposures. These findings will likely contribute to the assessment of human cancer risk following exposure to multiple carcinogens.

The carcinogenic effects of ionizing radiation and chemicals vary markedly with age at exposure. The effect of combined exposure to radiation and environmental carcinogens in children is still a major concern, and warrants further study.

References

- [1] Shimada Y, Nishimura M, Kakinuma S, *et al.*: Radiation-associated loss of heterozygosity at the *Znfn1a1* (*Ikaros*) locus on chromosome 11 in murine thymic lymphomas, *Radiat Res*, 154, 293-300, 2000.
- [2] Kakinuma S, Nishimura M, Amasaki Y, *et al.*: Combined exposure to X-irradiation followed by *N*-ethyl-*N*-nitrosourea treatment alters the frequency and spectrum of *Ikaros* point mutations in murine T-cell lymphoma, *Mutat Res*, 737, 43-50, 2012.
- [3] Hirano S, Kakinuma S, Amasaki Y, *et al.*: *Ikaros* is a critical target during simultaneous exposure to X-rays and *N*-ethyl-*N*-nitrosourea in mouse T-cell lymphomagenesis, *Int J Cancer*, 132, 259-268, 2013.

Highlight

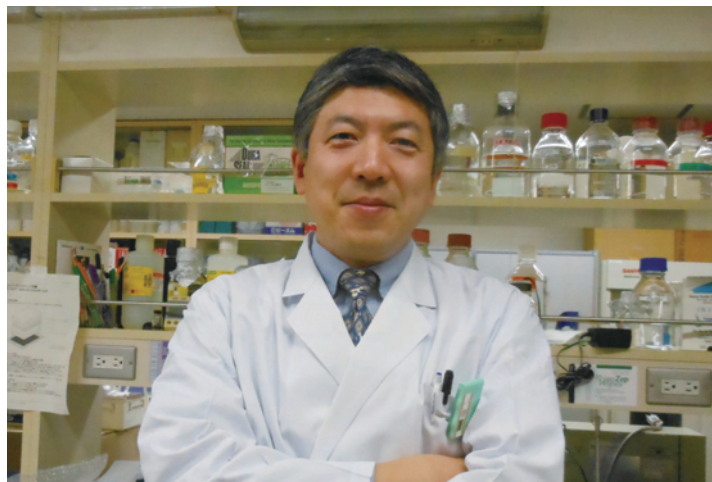
Reduction of high-dose-radiation-induced delayed genotoxic effects by radioadaptive response in mice

Bing Wang

E-mail: jp2813km@nirs.go.jp

Radiation-induced adaptive response (AR) is a phenomenon manifesting as a priming low-dose-induced resistance to a subsequent challenge exposure at higher doses. Investigations of AR are expected to provide an important scientific basis for radiation risk estimates, protection and practical applications, which are of great interest for both public health and academic research. AR has been studied for nearly three decades since the concept was first introduced into radiation biology and demonstrated in a variety of *in vitro* and *in vivo* systems. Among the documented *in vivo* AR models, the mouse AR model (Yonezawa Effect) was originally established by using sparsely ionizing (low linear energy transfer (low-LET)) X-rays as both the priming and challenge irradiations, and it was characterized by significantly decreased mortality in the 30-day survival test. The underlying mechanism was due to radioresistance occurring in blood-forming (hematopoietic) tissues. Reproducibility of the Yonezawa Effect was verified and confirmed previously in our lab using C57BL/6J female mice. Irradiations were performed by delivering a priming low dose of X-rays (0.50 Gy) in combination with a challenge high dose from either X-rays or densely ionizing (high-LET) accelerated ion particles^[1,2]. In this study, we further investigated the residual damage in the hematopoietic system in surviving animals^[3]. By verifying the residual damage in the hematopoietic system in the mouse survivors from the AR group (receiving both the priming and challenge irradiations) and the non-AR group (receiving only the challenge irradiations), we aimed at studying whether the priming irradiations could relieve the detrimental late effects induced by the challenge irradiations in this mouse model of AR.

C57BL/6J Mice strain female mice were used and all experimental protocols involving them were reviewed and approved by The Institutional Animal Care and Use Committee of the National Institute of Radiological Sciences (NIRS). The experiments were performed in strict accordance with the NIRS *Guidelines for the Care and Use of Laboratory Animals*. X-rays were generated with an X-ray machine (Pantak-320S, Shimadzu, Japan) operated at 200 kVp and 20 mA, using a 0.50-mm Al + 0.50-mm Cu filter. For high-LET heavy-ion irradiations, a monoenergetic beam of carbon or neon particles was generated and accelerated by the synchrotron (a cyclic particle accelerator with its guiding magnetic field syn-



chronized to the particle beam) of the Heavy Ion Medical Accelerator in Chiba (HIMAC), at NIRS. The beam energy was 290 MeV/nucleon for carbon ions and 400 MeV/nucleon for neon ions, corresponding to average LET values of about 15 keV/ μm and 30 keV/ μm , respectively.

Residual damage in the hematopoietic system was studied in the peripheral blood hemogram (a complete blood count) in the surviving animals one day after the 30-day survival test. Results showed that the priming low dose of X-rays could relieve the detrimental effects on the hematopoietic system. The priming low dose of X-rays significantly reduced the decrease in peripheral blood platelet count induced by the challenge exposure (X-rays or heavy ions) (data not shown). Because bone marrow failure (loss of blood-forming ability) was the main cause of animal death in this AR mouse model, we also measured residual damage in the bone marrow cells of surviving animals one day after the 30-day survival test. Results obtained in surviving animals from the positive control group (receiving both priming and challenge doses from X-rays), the carbon ion group (receiving the priming dose from X-rays and challenge dose from carbon ions), and the neon ion group (receiving the priming dose from X-rays and challenge dose from neon ions) are shown in Fig. 1. We observed both an improvement in the ratio of immature red blood cells (polychromatic erythrocytes (PCEs)) to the sum of PCEs and mature red blood cells (normochromic erythrocytes (NCEs)) (Fig. 1A) and a marked reduction of both the incidences of PCEs with small nuclei (micronucleated (MN)) (MNPCEs) (Fig. 1B) and the incidences of NCEs with small nuclei (MNNCEs) (Fig. 1C). The small nuclei are the by-products resulting from chromosomal damages caused by radiation.

Low doses of low-LET irradiations induce protective effects through mechanisms such as enhancement of antioxidative ca-

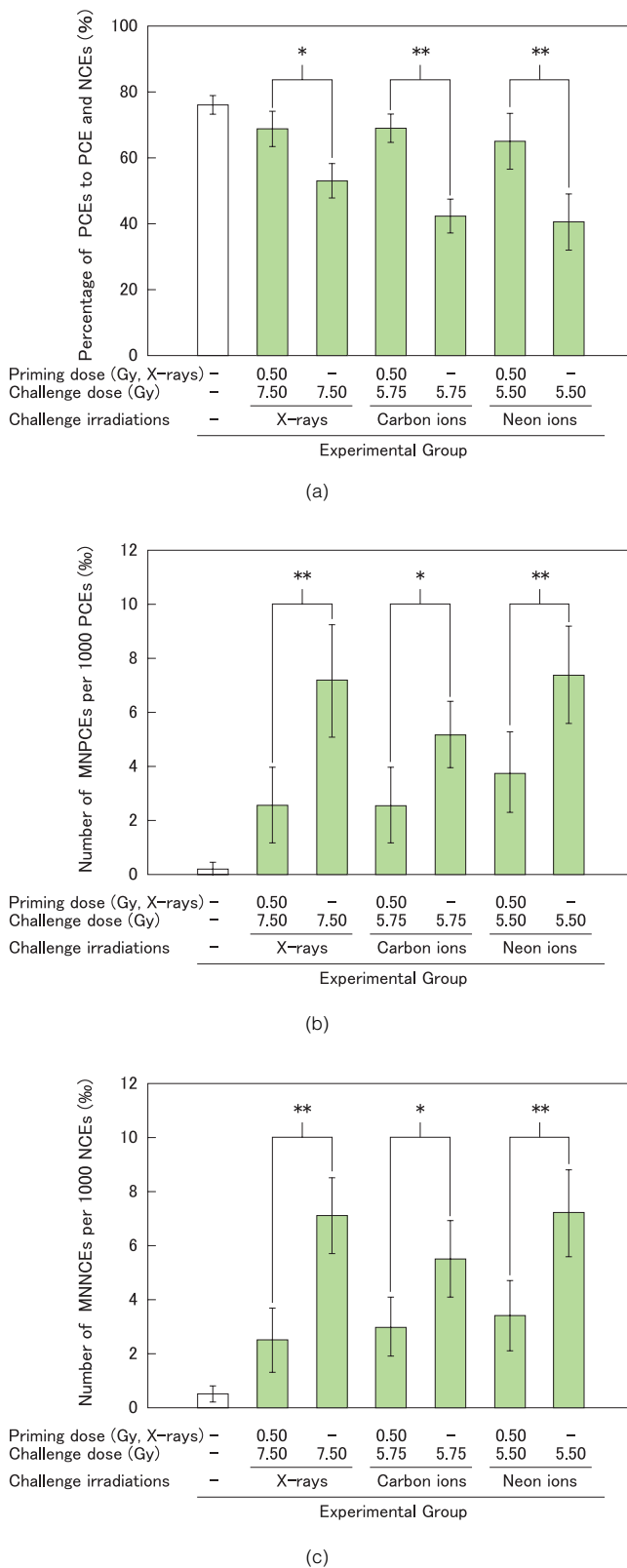


Fig.1 Relief by a priming dose of 0.50 Gy X-rays of delayed genotoxic effects on the femur bone marrow of mice from a challenge dose of 7.50 Gy X-rays, 5.75 Gy carbon or 5.50 Gy neon. The percentage of PCEs to PCEs and NCEs (A), the per-mille of MNPCEs to PCEs (B), and the per-mille of MNCEs to NCEs (C) are shown. * $P < 0.05$; ** $P < 0.01$ [3].

capacities, increase in cellular DNA double-strand break repair capacity leading to reduction of initial DNA damage in AR in mice *in vivo*, and reduction of cell death, chromosomal aberrations, mutations and malignant transformation *in vitro*. These induced responses have been tightly conserved throughout evolution, suggesting that they are basic responses critical to life. In addition to the acute mouse killing effect in the AR animal model, examination of residual damage and late detrimental effects on the hematopoietic system, such as the decrease in blood cell production (myelosuppression) and delayed genotoxic (toxic to DNA) effects, is of importance from the viewpoint of AR study and radiation protection.

Taken together, our results showed that a priming low dose of low-LET X-rays could relieve detrimental late effects including the decrease in blood-forming function (anhematopoiesis) and delayed genotoxic effects that were induced by high dose of either low-LET X-rays or high-LET heavy ions in bone marrow cells. These findings suggested that the priming low dose of low LET irradiations induced a protective effect on the hematopoietic system, which may play an important role in both rescue from acute lethal damage (mouse killing) and prevention of late detrimental consequences (residual anhematopoiesis and delayed genotoxic effects) caused by exposure to a high challenge dose from either low-LET or high-LET irradiations. Results indicated the significance and possible application of AR to the reduction of genomic instability induced by high-dose irradiations. These findings bring new knowledge to the characterization of the Yonezawa Effect by providing new insight into the mechanistic study of AR *in vivo*.

References

- [1] Wang B, Tanaka K, Vares G, *et al.*: X-rays-induced radioresistance against high LET irradiations from accelerated heavy ions in mice, *Radiat Res*, 174, 532-536, 2010.
- [2] Wang B, Tanaka K, Ninomiya Y, *et al.*: X-ray-induced radioresistance against high-LET radiations from accelerated neon-ion beams in mice, in: Neno M (ed), *Current Topics in Ionizing Radiation Research*, Rijeka: Intech-Open Access Publisher, 199-214, 2012.
- [3] Wang B, Tanaka K, Ninomiya Y, *et al.*: Relieved residual damage in the hematopoietic system of mice rescued by radiation-induced adaptive response (Yonezawa Effect), *J Radiat Res*, 54, 45-51, 2013.

Highlight

Looking for biomarkers that identify potentially sensitive individuals: Development of technology to discover genetic radiation risk-modifying factors and their biomarkers useful for radiation risk reduction

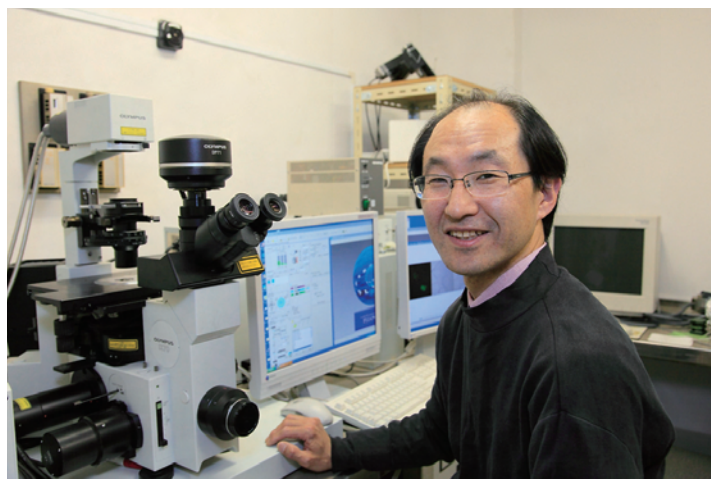
Manabu Koike, PhD.

E-mail: m_koike@nirs.go.jp

One of the purposes of our research program is to provide a scientific basis for radiation risk reduction. Therefore, it is important to discover genetic radiation risk-modifying factors in the human population. The first step for achieving this purpose is to develop a method to discover genetic radiation risk-modifying factors that will help to advance an individual-oriented risk assessment of low-dose radiation.

Development of new technology to discover genetic radiation risk-modifying factors useful in the individual-oriented risk assessment of low-dose radiation

Human cancer development is a multi-step process, and many mutations are necessary for a cell to become a cancer cell. It is unlikely that low-dose radiation dramatically induces and accumulates many mutations in genetically normal human cells. The DNA repair system protects the human genome from radiation. In



humans, non-homologous end joining (NHEJ) is the predominant repair system for DNA double-strand breaks (DSBs). It is suggested that a more error-prone pathway, i.e., microhomology-mediated end joining, repairs DSBs, if the NHEJ pathway is inactivated. Therefore, defects in the DNA repair genes, especially core-NHEJ genes, are assumed to be key process for radiation carcinogenesis and oncogenesis. In fact, it has been reported that genetic variations in NHEJ genes can influence DNA repair capacity and confer predisposition to several types of clinical hu-

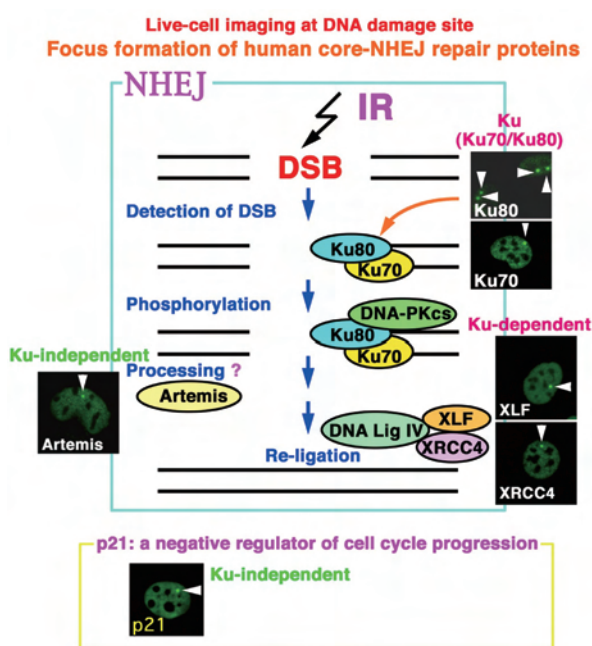


Fig.1 Live cell imaging of human core-NHEJ repair proteins at DNA damage sites and molecular mechanisms of human NHEJ repair system; modified from figures in [1], [3] and *J. Vet. Med. Sci.*, 74, 1269-1275, 2012.

Look for biomarker to look for radiation sensitive individuals

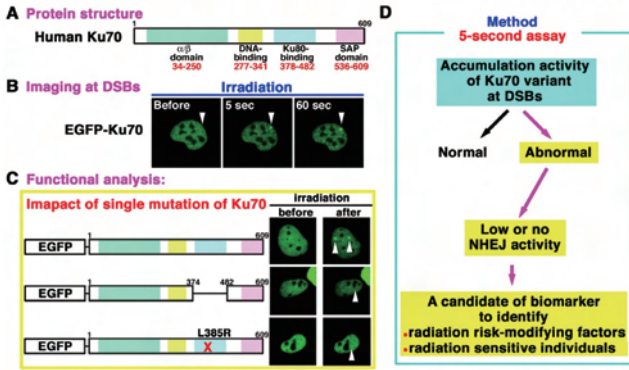


Fig.2 Development of new method to discover genetic radiation risk-modifying factors using technology which combined the microirradiation and live-cell imaging techniques; modified from figures in [1].

man cancer. Furthermore, patients who have a mutation (or mutations) in core-NHEJ genes, i.e., Artemis, DNA-PKcs, DNA ligase IV, or XLF, have already been reported, and some of these patients and animal models showed cancer predisposition. Therefore, we are interested in the idea that significant defects in NHEJ functions might confer genetic susceptibility to radiation.

The NHEJ is considered to begin with the binding of Ku, i.e., a heterodimer of Ku70 and Ku80 (Fig. 1). Human lung cancer causes many deaths worldwide. Recently, a significant association between the polymorphisms of genes in the NHEJ pathway and lung cancer susceptibility or prognosis has been reported. Thus, we have established and characterized Ku70-deficient epithelial cell lines (MLEs) from murine lungs lacking Ku70^[1,2]. Expectedly, the Ku70^{-/-} MLE cells were markedly sensitive to X-irradiation at low doses, from 0.125 to 2 Gy as compared with Ku70^{+/-} MLE cells. The accumulation mechanism of Ku70 at DSBs plays key roles in regulating the NHEJ activity. We hypothesized that influence on NHEJ activity of a genetic variation of Ku70 could be evaluated, if the accumulation at DSBs of Ku70 and its mutants could be observed. We examined whether EGFP-tagged human Ku70 expressed in Ku70^{-/-} MLE cells accumulated at DSB sites^[1]. As shown in Fig. 2, we could observe that EGFP-Ku70 accumulated at DSBs immediately after irradiation, when the DSBs were induced using our simple live-cell imaging technique with a laser. On the other hand, the Ku70 deletion mutant (EGFP-Ku70 (Δ375-481)) failed to accumulate at the irradiated sites. Next, we investigated the association of a single mutation of Ku70 with DNA repair capacity using the same method (Fig. 2). Our findings showed that a single mutation of Ku70 at amino acid 385 in the Ku80-binding domain inhibits the interaction of Ku70 with Ku80, and EGFP-Ku70(L385R) cannot accumulate at DSBs. These results indicate that we can evaluate whether the variation of Ku70, e.g., single nucleotide polymorphisms (SNPs), modifies the repair activity of NHEJ using this method. Altogether, we have succeeded in developing a new method to discover genetic radiation risk-modifying factors, although it is a prototype (Fig. 2).

Next, using the Ku70^{-/-} MLE cells established, we showed that Ku70 is essential for the accumulations of XRCC4 and XLF, but not of Artemis and p21, at DSBs in the early stage following irradiation of lung epithelial cells (Fig. 1)^[1,3]. Thus, the accumulation of the core-NHEJ factors XRCC4 and XLF is dependent on Ku; however, that of another NHEJ factor, Artemis, which plays a role

Live cell imaging at DNA damage sites in EGFP-XRCC4 expressed cells

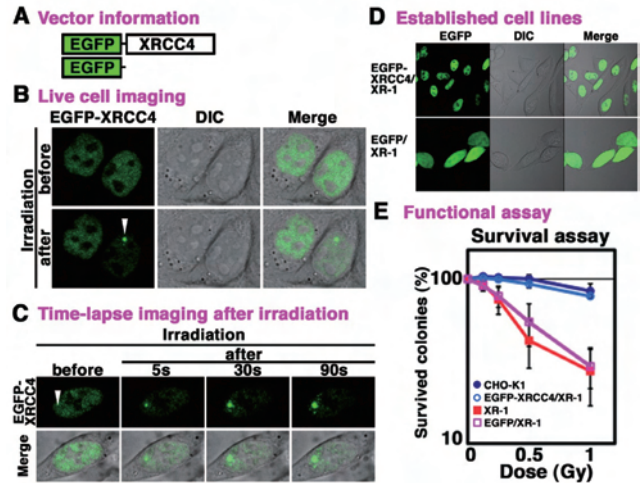


Fig.3 Establishment and characterization of cell lines with EGFP-tagged human XRCC4 useful to identify potentially sensitive individuals; modified from figures in *J. Vet. Med. Sci.*, 74, 1269-1275, 2012.

in both the NHEJ and homologous recombination (HR) pathways, is independent of Ku in MLE cells. This information will be useful to clarify the functional significance of SNPs of NHEJ genes.

We have also established and characterized cell lines with EGFP-tagged human XRCC4 (Fig. 3). These cell lines might be useful for the study of the molecular mechanism underlying the cellular resistance via the XRCC4-dependent NHEJ repair pathway to low-dose radiation. Furthermore, these cell lines might be useful to identify potentially sensitive individuals, who have an abnormality in the XRCC4-dependent DNA repair function.

Conclusion and Perspective

It is possible that certain human populations possess a lower DNA repair capacity due to a genetic factor, and thus they experience a greater effect due to radiation exposure. In this program, until now, we have identified two genes, i.e., Ku70 and XRCC4, as candidates for genetic radiation risk-modifying factors useful in the risk assessment of low-dose radiation. Furthermore, the cell lines we have established might be useful to discover a more highly precise biomarker that will help to assess the risk and identify potentially sensitive individuals. We consider that the characterization of a large number of SNPs in all NHEJ-related genes will be a valuable source of information for assessment of radiation risk, and ultimately contribute to the *in silico* prediction of the risk from type of SNPs. In the near future, our strategy can be used to discover more candidates of genetic radiation risk-modifying factors useful in the individual-oriented risk assessment of radiation and, if this study is further extended and advanced it can become a basis for the development of an appropriate regulatory framework.

References

- [1] Koike M, Yutoku Y, Koike A.: Accumulation of Ku70 at DNA double-strand breaks in living epithelial cells, *Exp Cell Res*, 317, 2429-2437, 2011.
- [2] Koike M, Yutoku Y, Koike, A.: Establishment of Ku70-deficient lung epithelial cell lines and their hypersensitivity to low-dose X-irradiation, *J Vet Med Sci*, 73, 549-554, 2011.
- [3] Koike M, Yutoku Y, Koike A.: Accumulation of p21 proteins at DNA damage sites independent of p53 and core NHEJ factors following irradiation, *Biochem Biophys Res Commun*, 412, 39-43, 2011.

Highlight

Risk perception in Japan of nuclear power and other risk factors during 25 years before the Fukushima Daiichi Nuclear Power Plant accident

Reiko Kanda

E-mail; kanda_r_@nirs.go.jp

Introduction

The difference between the risks perceived by people and the objective risk (or the technically estimated risk) has been regarded as the biggest problem in public acceptance or in the risk communication of modern technologies. Risk perception was a popular subject of investigation during the 1980s, and the interests of researchers were diverted from the actual risk perception itself to its interpretation or application for risk communication/management from 1990 onwards. There have been a few studies about risk perception of nuclear power by carrying out fixed-point observations.

The present study described the results of three 'fixed-point' surveys in Japan on perceived risk related to a list of social and individual risk events during the 25 years prior to the Fukushima Daiichi Nuclear Power Plant accident.

Materials and Methods

Risk perception by employees at NIRS in Japan was examined in 1983, 1992 and 2007. These surveys are called the NIRS-1983 survey, the NIRS-1992 survey and the NIRS-2007 survey, respectively. The subjects and results of the surveys in 1983 and 1992 have already been reported^[1].

In 2007, we undertook a similar survey of public perception in all parts of Japan using Web-based questionnaires, called the Web survey, and obtained 638 responses. We asked participants about their occupations, academic careers, families and lifestyles.

The perceived risk was examined by the risk ranking technique, which is essentially the same as the original technique developed by Slovic *et al.*^[2]. A set of 30 cards, each of which listed one specific item related to technology or to a human activity, was prepared. The listed risk items included technological risks, accidental risks and chronic and low exposure risks.

The subjects were interviewed in groups and asked to order the 30 cards according to their subjective judgments about the perceived magnitude of risks. In the Web survey, the subjects similarly ordered the virtual cards on the screen. The ordering of risk perception was based on the geometric mean risk rating within each group.



Results and Discussions

1) Dynamics of the risk perception during the last 25 years

The survey results showed that the ranking of the risk of motor vehicles fell during the 25-year period covered in the study, whereas those of power mowers and hunting rose during the last 15 years. The rankings of these two categories in the Web survey were quite similar to those of the same categories in the NIRS-2007 survey (Table 1).

The rankings of the possible sources of health risk related to chronic and low exposure (to food preservatives, X-rays and antibiotics) rose, and sources of accidental risk (surgery, fire fighting, police work and aviation) fell transiently in 1992. The public are often less concerned about risks over which they believe they have some degree of control, such as motor vehicle accidents and the accident risk may produce less anxiety because the outcome is resolved quickly, while health risk related to chronic and low exposure such as food-borne hazards may take years to manifest.

In the 1990s, risks of chemicals presumably in the environment were experienced as a result of new technologies, which might cause the transient rise of the rank of perceived risk related to chronic and low exposure. And the order of perceived risk of X-rays rose in the NIRS-1992 survey, which might have been influenced by the Chernobyl accident. When the Chernobyl accident occurred in 1986 in the former USSR, catastrophic on-site situations and radiation risk were repeatedly reported in Japan by various mass media. These rises of perceived risk ranking were transient and fell in 2007, which revealed that people tended to learn how to accommodate themselves to low risk in exchange for a high benefit related to technical risks during the last 15 years. However, the case of nuclear power was an exception.

Table 1 Ordering of perceived risk for 30 activities and technologies (overview)

	Total				Female (General public)				Researchers			
	WEB 2007	NIRS 2007	NIRS 1992	NIRS 1983	WEB 2007	NIRS 2007	NIRS 1992	NIRS 1983	NIRS 2007	NIRS 1992	NIRS 1983	
Number of subjects												
Male	319	52	20	36	0	0	0	0	46	20	36	
Female	319	63	38	30	319	37	33	25	15	5	5	
Age	*20s- 60s	20s- 60s	26- 55	20- 59	20s- 60s	20s- 60s	32- 55	20- 45	20s- 60s	26- 48	28- 59	
1. Handguns	1	1	1	3	1	1	2	1	1	1	4	
2. Nuclear power	2	2	2	19	2	2	1	4	12	5	28	
3. Smoking	3	4	9	4	3	13	8	8	3	12	5	
4. Private aviation	4	5	4	7	7	3	11	5	7	3	9	
5. Hunting	5	7	16	16	4	5	18	14	5	11	14	
6. Police work	6	10	6	8	6	8	12	7	8	4	11	
7. Surgery	7	8	10	6	8	4	14	11	9	6	6	
8. Fire fighting	8	6	14	9	5	6	17	10	6	8	10	
9. Motorcycles	9	3	3	2	9	10	10	3	2	2	2	
10. Large construction	10	11	11	5	11	7	13	16	11	7	3	
11. Motor vehicles	11	9	5	1	13	12	7	2	4	10	1	
12. X-rays	12	14	8	20	10	11	5	18	18	13	22	
13. Commercial aviation	13	12	17	15	12	9	15	13	15	15	15	
14. Pesticides	14	15	12	11	14	15	9	15	13	14	12	
15. Antibiotics	15	19	15	18	15	19	4	12	22	23	20	
16. Food preservatives	16	20	7	13	16	18	3	6	20	17	19	
17. Mountain climbing	17	13	19	12	18	16	23	21	10	9	8	
18. Food colouring	18	18	13	14	17	17	6	9	21	18	17	
19. Power mowers	19	16	25	28	19	14	26	28	17	20	27	
20. Contraceptives	20	25	20	24	20	21	19	19	27	21	23	
21. Alcoholic beverages	21	21	21	17	22	27	21	17	16	22	13	
22. Vaccinations	22	23	18	23	21	20	16	22	25	24	21	
23. Spray cans	23	29	22	25	23	24	20	23	29	29	24	
24. Railroads	24	27	23	22	24	26	22	25	28	27	18	
25. Skiing	25	22	27	27	25	22	29	27	23	19	25	
26. Bicycles	26	17	24	10	27	25	24	20	14	25	7	
27. Home appliances	27	30	30	30	26	30	27	30	30	30	30	
28. Electric power	28	24	28	26	28	23	25	24	26	28	26	
29. Football	29	26	26	29	29	29	28	29	19	16	29	
30. Swimming	30	28	29	21	30	28	30	26	24	26	16	
Spearman's coefficient of rank correlation	0.93				0.93				0.76			
									0.57			
									0.63			

*In order to ensure privacy, we did not ask respondents for their ages in the Web and NIRS-2007 surveys.

2) Factors influencing perceived risk observed in the Web survey

In the Web survey, the risk perceptions were uniform irrespective of gender, age and occupation except that both males and females aged over 60 judged X-rays as a higher risk (3rd-5th) than the other categories (Table 2). Furthermore, academic major (cultural, social, life sciences or other natural sciences) and educational background (high school, junior college, university or graduate school) of the subject persons had no influence on risk perception.

In a previous study, we examined the risk perception of the people who had received training in a radiation protection course at the NIRS^[3], and the respondents who had majored in life sciences (biology, pharmacy, medicine, dentistry and agriculture) judged

nuclear power as a higher risk (2nd) than did those who had majored in physics, chemistry or technology (14th). In the present study, however, academic majors had no influence on the risk perception of ordinary lay people, who were less interested in nuclear power and radiation.

Furthermore, whether respondents had children or not, the age of the respondents' children, and the respondents' lifestyle did not influence their ordering of the perceived risk.

Contrary to our expectations, there was no difference in the rank of 'motor vehicles' and 'motorcycles' between non-drivers and drivers, nor was there any difference in the rank of 'smoking' between smokers and non-smokers for either men or women.

Table 2 Ordering of perceived risk for 30 activities and technologies in the Web survey

	Male					Female					Occupation*			Life-style			
	20s	30s	40s	50s	>60s	20s	30s	40s	50s	>60s	Group A	Group B	Group C	Smoker	Non-smoker	Driver	Non-driver
Number of respondents	44	84	103	77	11	44	84	103	77	11	292	58	288	162	476	463	175
1.Handguns	1	1	1	1	2	1	1	1	1	1	1	1	1	1	1	1	1
2.Nuclear power	2	2	2	2	1	2	2	2	2	2	2	2	2	2	2	2	2
3.Smoking	3	4	3	3	4	3	3	4	3	4	3	4	3	5	3	3	3
4.Private aviation	5	6	5	4	5	8	6	7	5	7	4	3	7	4	4	4	4
5.Hunting	9	8	4	8	14	10	4	6	4	3	6	5	5	6	5	5	7
6.Police work	8	5	8	6	13	6	7	3	7	19	7	7	4	7	6	7	5
7.Surgery	4	3	7	5	10	4	5	9	9	6	5	6	8	3	8	6	6
8.Fire fighting	15	9	9	7	12	5	8	5	6	17	9	10	6	11	7	8	8
9.Motorcycles	7	7	6	10	6	9	15	8	8	9	8	9	9	8	9	9	10
10.Large construction	10	10	10	9	15	12	11	13	10	8	11	11	10	10	10	10	12
11.Motor vehicles	6	11	11	12	9	13	13	10	13	11	10	16	11	9	12	11	11
12.X-rays	11	13	12	11	3	7	12	11	11	5	12	8	12	12	11	12	9
13.Commercial aviation	14	12	17	13	22	11	10	12	12	23	13	17	13	14	13	13	14
14.Pesticides	19	14	13	14	7	16	9	14	17	12	14	13	15	15	14	14	13
15.Antibiotics	12	16	14	15	11	14	17	15	14	14	15	14	14	13	15	15	15
16.Food preservatives	13	18	16	17	8	15	14	19	15	13	17	12	16	17	16	16	16
17.Mountain climbing	18	15	15	16	20	20	18	16	18	10	16	18	18	18	17	17	18
18.Food colouring	17	20	18	18	16	19	16	17	16	15	18	15	17	16	18	18	17
19.Power mowers	21	17	20	20	17	17	19	18	20	21	19	19	19	20	19	19	20
20.Contraceptives	16	23	19	23	23	18	24	20	21	16	21	23	20	19	21	21	19
21.Alcoholic beverages	20	19	21	21	18	21	21	23	23	20	20	20	22	21	20	20	22
22.Vaccinations	26	21	23	19	21	23	23	21	19	18	22	22	21	22	22	22	21
23.Spray cans	22	22	22	22	19	26	20	22	22	26	23	21	23	23	23	23	23
24.Railroads	27	24	25	25	25	22	22	24	25	24	24	25	24	24	24	24	24
25.Skiing	23	26	24	24	27	25	27	25	24	22	25	24	25	26	25	25	25
26.Bicycles	28	25	27	26	26	29	26	26	26	27	26	28	26	25	26	26	27
27.Home appliances	24	28	30	28	28	24	25	27	28	29	27	29	27	27	28	28	26
28.Electric power	25	27	28	29	24	27	28	29	29	28	28	30	28	28	27	27	28
29.Football	30	30	26	27	29	28	29	28	27	25	29	26	29	29	29	29	29
30.Swimming	29	29	29	30	30	30	30	30	30	30	30	27	30	30	30	30	30

*Group A: Company employees and public employees/Group B: Self-employed persons and freelance professionals/Group C: Housewives, part-timers and unemployed.



Fig.1 In the NIRS surveys, the subjects ordered the 30 cards according to their subjective judgments about the perceived magnitude of risks.

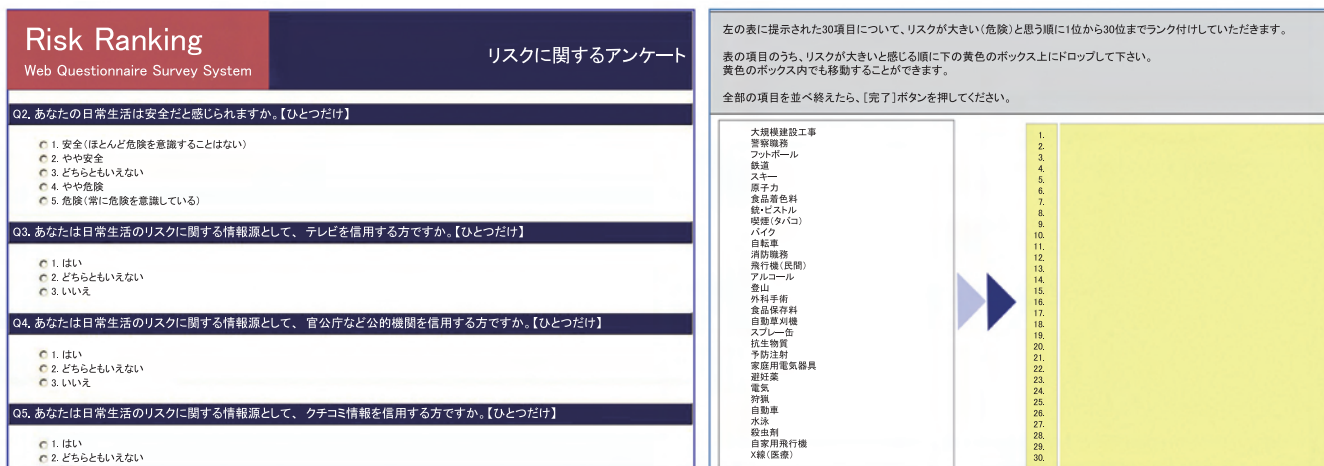


Fig. 2 In the Web survey, the subjects answered the questions about their occupations, academic careers, families, points of view and lifestyles and ordered the virtual cards on the screen (*Health Physics*, 102, 384-390, 2012).

3) Problems of risk communication regarding the Fukushima crisis

The TEPCO Fukushima Daiichi Nuclear Power Plant experienced a nuclear crisis after the seismic-triggered events of March 11. The present study revealed that nuclear power plants were regarded as high-risk facilities by Japanese citizens even before the crisis. Of course, such higher gaps in risk perception about nuclear power are also found with the general public in other nations. But there were observed differences in risk perception and attitude among different groups in contrast with the uniformity of Japanese perception in 2007.

During the initial period of the Fukushima crisis, when the public felt that the available information to them was so scarce, the internet and twitter information played a certain role. As a result of information from unknown sources, quite a few people actually swallowed gargling agents containing povidone iodine as a substitute for stable iodide tablets; such actions would not be recom-

mended by medical experts due to the expected adverse effects of the agent constituents. And, nowadays many Japanese people are very worried about small levels of radioactive contamination of foods. These behaviours and reactions are partly understood by their over-response to nuclear power and food additives before the accident.

References

- [1] Kanda R, Fujimoto K, Kobayashi S.: Comparison of risk perception on industrial and social events among three different groups of people who are engaged in education and research activities in Japan, *Jpn J Risk Anal*, 6, 88-95, 1994.
- [2] Slovic P, Fischhoff B, Lichtenstein S.: Perceived risk: psychological factors and social implications, *Proc R Soc A*, 376, 17-34, 1981.
- [3] Kanda R, Joshima H, Kobayashi S.: Knowledge and perception of risk among trainees on radiation protection course, *Jpn J Risk Anal*, 7, 67-73, 1995.

Protection against radon

**Tetsuo Ishikawa, Mirosław Janik,
Norbert Kavasi, Kazuki Iwaoka, Yasutaka Omori**

E-mail: tetsuo_i@nirs.go.jp

The five-year project of the Regulatory Science Research Group includes topics on estimation of public and occupational dose due to radon and its mitigation. Regarding these topics, the following progress was made in FY 2011 and 2012.

Radon mitigation

There are two possible ways to reduce exposure due to indoor radon and its decay products. One is to reduce radon concentrations, such as improving ventilation, aspirating air under floors, and sealing walls with plastic sheets. Ventilation, however, is not always practical in winter from the viewpoint of energy consumption. Another way is to directly reduce the concentration of radon decay products. Use of air cleaners is a typical method for this. In this study, effects of dose mitigation by a commonly-used air cleaner were investigated. Experiments were conducted using a radon chamber at NIRS with a radon concentration of about 10,000 Bq m⁻³. Aerosols with a median diameter of 100 nm were injected into the radon chamber.

Radon progeny concentration in the chamber was measured with conditions of the air cleaner ON and OFF. Although EERC (equilibrium equivalent radon concentration) was decreased during operation of the air cleaner, the unattached fraction (fraction of aerosol-unattached radon progeny) was increased. The air cleaner did not lower the radon concentration. The dose due to radon progeny was decreased with the EERC decrease, but the increase of the unattached fraction partially contributed to an increase of dose. Calculation results showed that the dose was decreased by about 40 % using the air cleaner. Air cleaners can be regarded as an effective tool for dose mitigation of the environment containing aerosols^[1].

International intercomparison for integrating radon and thoron detectors

According to the UNSCEAR 2000 report, the contribution of radon, thoron and their decay products represents the largest fraction of the world mean annual effective dose to the general population from natural radioactivity. Thus, many countries have conducted national or regional surveys of radon and thoron levels to determine average exposures and to recognize locations where



high radon or/and thoron levels occur. Many different measurement methods and instruments have been used in those surveys. In addition, new institutions and companies continually enter the field of radon and thoron measurements and new devices are still being developed. Thus, it is important to maintain the reliability of those devices by comparing them under the same conditions.

In this respect, we have already conducted three international intercomparison exercises at NIRS with a 24.4 m³ inner volume walk-in radon chamber that has systems to control radon concentration, temperature and humidity^[2]. Upon requests from the participants of previous intercomparison exercises, the 4th international intercomparison for integrating radon detectors was conducted in 2011. Since the inner volume is 24.4 m³, a large number of monitoring instruments can be accommodated at the same



Fig. 1 Photo showing the walk-in radon chamber at NIRS.

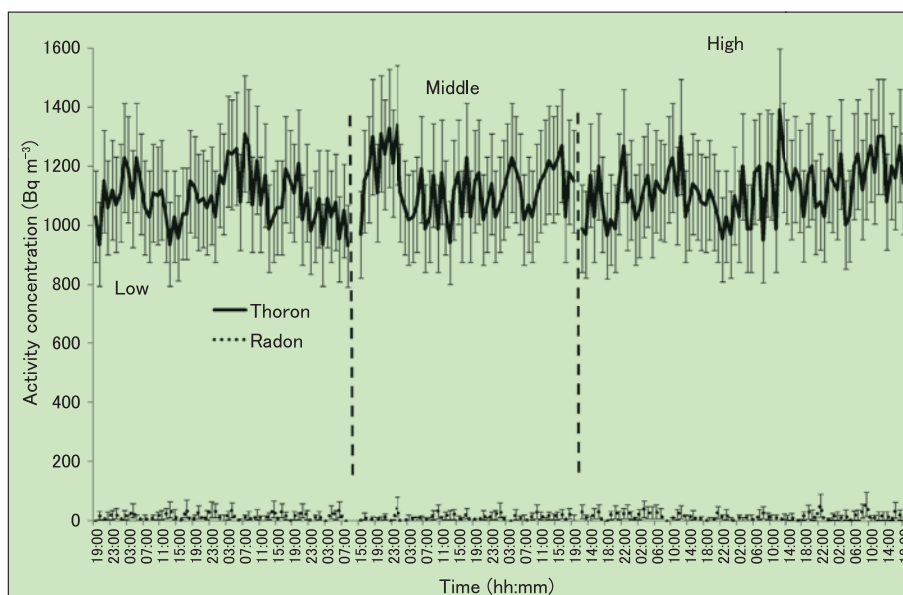


Fig.2 Plot of activity concentrations of radon and thoron obtained from experiments in the thoron experimental room^[3].

time (Fig. 1). Prior to these experiments the spatial uniformity of the radon concentration inside the radon chamber was established with appropriate tests. The NIRS radon chamber usually operates at one of three possible levels of exposure: low, medium and high with levels of 100 kBq h m⁻³, 500 kBq h m⁻³ and 1000 kBq h m⁻³, respectively. Furthermore, the 3rd thoron intercomparison was conducted with the NIRS thoron chamber of a 0.15 m³ inner volume.

Thirty-one laboratories from 15 countries participated in the radon intercomparison, using four types of detectors (CR-39, LR-115, polycarbonate film, charcoal, electret and photodiode) and 36 sets of detectors. Twelve laboratories from eight countries using two etch-track types (CR-39, polycarbonate) and 12 sets of dosimeters participated in the thoron intercomparison.

The tests were made on three different exposures of radon and three of thoron. It was found that 58% and 39% of the results did not differ more than 10% from the reference values of radon and thoron experiments, respectively. A large percentage of detectors, 57%, had a deviation of more than 20% for the thoron results which revealed problems and difficulties in the thoron calibration and measurement.

We are convinced that periodical intercomparison exercises for radon and thoron should be carried out, according to the needs from various institutions.

Thoron experimental room

According to the WHO handbook on indoor radon (²²²Rn), the health risk originating from inhaled ²²²Rn and its progeny is higher than was previously estimated. This fact highlights the importance of measurements of ²²²Rn and the hitherto neglected ²²⁰Rn as the latter can influence the results of ²²²Rn measuring units and in elevated amounts can increase the risk to human health. NIRS had already built a small-size ²²⁰Rn chamber (0.15 m³). Owing to its

small volume, however, the chamber could not meet the expanding demands of the comparison campaigns; therefore, a larger size chamber was required.

Thus, a new thoron (²²⁰Rn) experimental room was established at NIRS in 2011 to respond to the appearance of new passive devices for ²²⁰Rn and its progeny (²¹²Pb, ²¹²Bi) measurements. The room volume is 21.7 m³ with a low air exchange rate, 0.016 h⁻¹. Environmental parameters, such as temperature, relative and absolute humidity, wind speed, aerosol distribution and concentration, are monitored, but not controlled. Commercially available lantern mantles (500 pcs), which can generate maximum concentrations of 6000 Bq m⁻³ of ²²⁰Rn and 2000 Bq m⁻³ of its progeny, are used as a ²²⁰Rn source. Based on preliminary results from the thoron experimental room, stable and homogenized concentrations of ²²⁰Rn and its progeny can be ensured (Fig.2).

The ²²⁰Rn production from the lantern mantles is affected by absolute humidity; therefore, it is essential to check this parameter for adjustment of the level of ²²⁰Rn and its progeny. Getting a homogenous distribution of ²²⁰Rn in the room demands continuous air mixing. In the case of air mixing, the ²²⁰Rn progeny level was lower by one order of magnitude compared with the level of unmixed air. In the near future the room will be used for testing measuring instruments^[3].

References

- [1] Iwaoka K, Tokonami S, Ishikawa T, *et al.*: Mitigation effects of radon decay products by air cleaner, *J Radioanal Nucl Chem*, 295, 639-642, 2013.
- [2] Janik M, Tokonami S, Kranrod C, *et al.*: International intercomparisons of integrating radon/thoron detectors with the NIRS radon/thoron chambers, *Radiat Prot Dosim*, 141(4), 436-439, 2010.
- [3] Kavasi N, Janik M, Prasad G, *et al.*: Thoron experimental room at the National Institute of Radiological Sciences (NIRS), Japan, *Radiat Prot Dosim*, 152(1-3), 150-153, 2012.